TRIANGULAR SEGMENTS AND TWO-DIMENSIONAL ANALYSIS FOR MICROWAVE INTEGRATED CIRCUITS

A Thesis Submitted
in Partial Fulfilment of the Requirements
for the Degree of
DOCTOR OF PHILOSOPHY

By

RAKESH CHADHA

to the
DEPARTMENT OF ELECTRICAL ENGINEERING
INDIAN INSTITUTE OF TECHNOLOGY, KANPUR
MAY, 1981
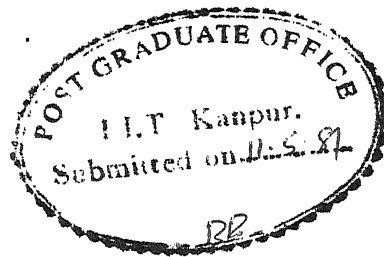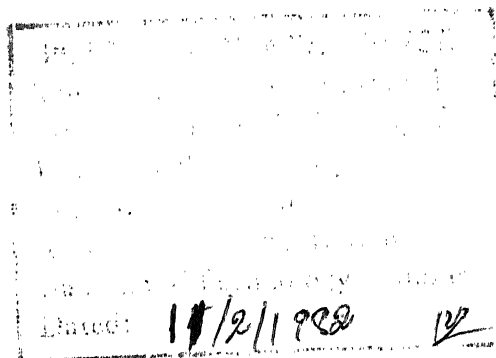
CERTIFICATE

This is to certify that the work reported in this thesis entitled 'TRIANGULAR SEGMENTS AND TWO-DIMENSIONAL ANALYSIS FOR MICROWAVE INTEGRATED CIRCUITS' by Mr. Rakesh Chadha has been carried out under my supervision and has not been submitted elsewhere for a degree.

(K.C. GUPTA)
Professor
Department of Electrical Engineering
Indian Institute of Technology
Kanpur 208016
INDIA

Dated: 11/2/1982

ACKNOWLEDGEMENTS

Thanks are also due to Shri C.M. Abraham for his excellent typing and Shri R.K. Bajpai for neat drawings.

Finally, I would like to mention that this work could not have been undertaken and carried out without the blessings of my teachers and elders. I shall always remain indebted to them.

May, 1981   — RAKESH CHADHA

TABLE OF CONTENTS

LIST OF TABLES

LIST OF FIGURES

Figure No.	Caption	Page

TRIANGULAR SEGMENTS AND TWO-DIMENSIONAL ANALYSIS
FOR MICROWAVE INTEGRATED CIRCUITS
A Thesis Submitted
In Partial Fulfilment of the Requirements
for the Degree of
DOCTOR OF PHILOSOPHY
by
Rakesh Chadha
Department of Electrical Engineering
Indian Institute of Technology, Kanpur
March, 1981

The concept of two-dimensional planar circuits is a generalization of one-dimensional stripline or microstrip circuits to the case when the transverse dimensions are comparable to wavelength. Thus, these circuits have dimensions comparable to (or greater than) the wavelength in two directions but have the third dimension much smaller than the wavelength. Analysis of two-dimensional circuits containing rectangular and circular segments by using impedance Green's functions is available in literature. Investigations reported in this thesis are aimed at (i) analysis of triangular planar segments and their applications in microwave integrated circuits, and (ii) use of two-dimensional analysis for the design and optimization of stripline and microstrip circuits.

The thesis begins with the development of impedance Green's functions for the analysis of triangular segments. Three types of triangles (30° - 60° right-angled, equilateral, and right-angled isosceles) are considered by placing additional image sources outside the triangular regions. The Green's functions satisfy

magnetic wall condition all along the periphery of the segments. Green's functions for some triangular shapes with electric wall on one of the sides and magnetic walls on the other two sides are also obtained.

Green's functions for circular sectors, annular rings, and annular sectors have been obtained by expanding these in series of eigenfunctions. As mutually orthogonal eigenfunctions are obtainable only for those sectoral angles which are submultiples of 180°, the Green's functions are obtainable for only these sectoral shapes.

Segmentation method for the analysis of planar circuits involves breaking up of a circuit pattern into segments for which Green's functions are known. S-matrix of the overall circuit is obtained from the S-matrices of the individual segments. This method is modified so that Z-matrices for individual planar segments are used to obtain the overall Z-matrix. The proposed method using Z-matrices is shown to be computationally more efficient than the earlier method.

The Green's functions, for the equilateral triangular segments, derived in this thesis have been used to analyze rhombic and hexagonal resonant shapes by segmenting these into triangular shapes. Equilateral triangular, 60°-rhombic, and regular hexagonal shapes are analyzed and their resonances have been investigated. It has been pointed out that equilateral triangular shapes have odd modes of resonances in addition to the even modes

reported earlier. For rhombic and hexagonal shapes, their resonance frequencies as well as the voltage variations around the periphery have been obtained for fundamental and some higher order modes. The resonance frequencies predicted have been verified experimentally for each of three shapes.

Stripline and microstrip T-junctions have been shown to exhibit lower parasitic reactances when triangular geometries are used as compared to the junctions with rectangular geometry normally used. Two types of T-junctions with impedance ratios $1:1:1$ and $(1/\sqrt{2}):1:1$ have been studied for this purpose. For T-junctions with impedance ratio $1:1:1$, an equilateral triangle is used at the junction. For T-junctions with impedance ratio $(1/\sqrt{2}):1:1$, a right-angled isosceles triangle (in magnetic wall model) is used at the junction. Improvements using triangular shaped junctions have been verified experimentally for both the cases.

The two-dimensional analysis technique can be used in optimization of the design of the circuits whose performance is limited by the junction reactances and the presence of higher order modes. This procedure has been used to obtain improved designs for 3 db in-phase power dividers and 3 db branch-line hybrids.

Three types of power divider circuits that have been considered are : i) a circuit with single matching section $(Z = Z_o/\sqrt{2})$ on the input side, ii) a circuit with single matching sections $(Z = Z_o\sqrt{2})$ on the output sides, and iii) a circuit with a matching

section ($Z=Z_0/2^{1/4}$) at the input side and matching sections ($Z=Z_0 \, 2^{1/4}$) on the output sides. Triangular geometries have been used at the T-junctions. The lengths of various matching sections and position and value of isolation resistance are optimized for each of the three types of power dividers to minimize input and output VSWR's at the center frequency. Experimental results for a microstrip circuit with single matching section at the input side are included.

For 3 db branch line hybrid also, right-angled isosceles triangles are used at each of the T-junctions. Lengths of the quarter wave sections are optimized to minimize the input VSWR and to equalize the power division at the center frequency.

These two circuit examples demonstrate the applicability of two-dimensional circuit analysis for the design and optimization of stripline and microstrip circuits.

INTRODUCTION

1.1 TWO-DIMENSIONAL COMPONENTS

Two-dimensional (2-d) microwave planar components have been proposed for use in microwave integrated circuits [1] - [4]. These components have dimensions comparable to (or greater than) the wavelength in two directions but have the third dimension much smaller than the wavelength. Three types of configurations for the 2-d components are thus possible. These are -(i) triplate or stripline type shown in Fig. 1.1(a) and (c); (ii) open or microstrip type shown in Fig. 1.1(b) and (c); and (iii) waveguide or cavity type shown in Fig. 1.1(d). The triplate and the open type configurations can be considered to be generalizations of one-dimensional stripline and microstrip circuits to the cases when the transverse dimensions are comparable to the wavelength. The waveguide type configuration (Fig. 1.1(d)) is a special case of three-dimensional waveguide in which the height is much smaller than the wavelength.

1.1.1 Methods of Analysis

Various methods for obtaining the characterization of a 2-d component depend upon its geometry (i.e. shape of the central conducting patch in a triplate structure or the upper

ϵ_r Stripline type

(a)

ϵ_r Microstrip type

(b)

2-D CIRCUIT ELEMENT   Plan view of (a) and (b)

(c)

2-D CIRCUIT ELEMENT   Waveguide type
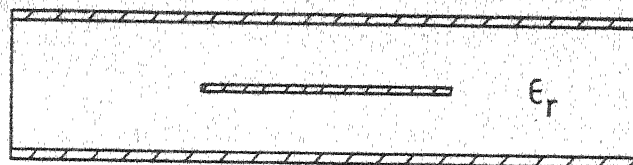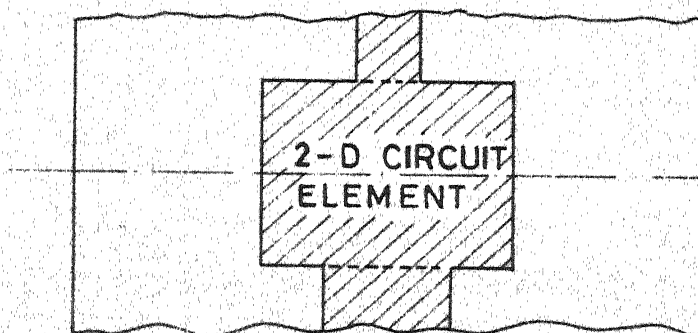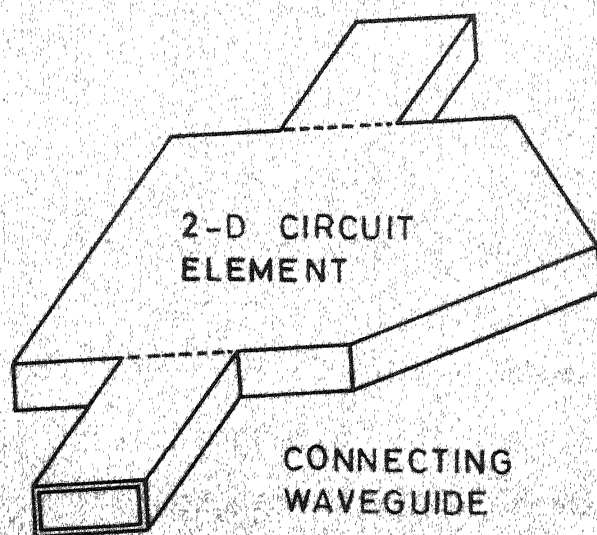
CONNECTING WAVEGUIDE

(d)

Fig.1.1 Three types of 2-d microwave circuits.

conductor patch in microstrip type circuit). When a 2-d component is of a simple geometrical shape, impedance Green's functions [1] are used for its analysis. These Green's functions have been known for only rectangular and circular shapes [3], [5]. Using Green's function, impedance matrix of a component can be obtained for specified port locations.

When the geometrical shape of a 2-d circuit can be considered to be made up of simpler shapes for which the Green's functions are available, the segmentation method [3],[4] can be used for finding the characteristics of the overall circuit from those of various components (with simple shapes). Details of the analysis using Green's functions and segmentation method are discussed in Chapter Two.

For the analysis of arbitrary shaped 2-d component, numerical methods are used. Finite element approach [2] and contour integral approach [1] have been discussed in the literature. The finite element approach is an extension of finite element methods [6] and involves the integration of certain basis functions over the entire conducting patch which is divided into numerous subsections. The contour integral method has been specifically proposed for 2-d components and is based on the Green's theorem in cylindrical coordinates. The voltage at a point on periphery is expressed in terms of line integral along the periphery. The periphery is divided into various sections and the impedance matrix is evaluated at these sections.

Another approach is the spectral domain analysis [7],[8] which has been used for many planar microwave integrated circuits. This method may be used for both the quasi-static and fullwave analysis. The quasi-static approach is used to compute the capacitance of the structure. The solution of the Poisson's equation is obtained in the Fourier transform domain. In the full-wave approach, Galerkin's procedure is used to deduce determinantal characteristic equation from the coupled algebraic equations in the Fourier transform domain.

1.1.2 Applications

There has been considerable interest in 2-d planar components in the last decade and these have found several applications in microwave integrated circuits, waveguide circuits, ferrite components and microstrip antennas. Some of the areas where the 2-d approach has found applications are listed below.

i) Resonators : Two-dimensional components can be used for the design of high-Q resonators used at microwave frequencies. Recently, triangular elements have been proposed for realizing resonators and prototype elements for band-pass and band-stop filters [9], [10]. Gap coupled triangular segments have been proposed for filter circuits [9] and the triangular resonators have been used in the design of three-port circulators [10].

ii) Discontinuity Analysis : Equivalent circuits have been
reported for most of the discontinuities in stripline and for
some discontinuities in microstrip line [11], [12]. For
several discontinuities, equivalent circuits are not available.
The 2-d approach can be employed to analyze accurately any
discontinuity. Even when an equivalent circuit is available,
a more accurate characterization can be obtained by the use of
2-d approach. It provides a general method for the analysis
of stripline and microstrip line discontinuities [13].

The concept of cavity type 2-d components, compatible for
use with waveguide circuits, can be used for the analysis of
waveguide discontinuities.

iii) Design of Novel Circuit Configurations: Several new
designs have emerged from the applications of 2-d circuit
approach. It has been shown [5] that a circular disc resonator
can be used as a 3 db hybrid circuit. Also a circular disc
resonator can behave as a coupled mode filter [14] when two
ports are located at right angles and the coupling between two
modes is obtained by having a very short strip length at an
open circuited third port.

iv) Design of Non-reciprocal Elements : 2-d circuits, fabri-
cated on ferrite substrates [15], may also be analyzed by the
2-d approach using the extension of analysis techniques for
circuits on dielectric substrates. This method has been used
for obtaining optimum shape of a wideband circulator [16].

v) <u>Microstrip Antennas</u> : Field distribution along the periphery of microstrip antennas can be evaluated by treating them as 2-d components with magnetic walls. The 2-d approach can be used to evaluate the voltages at various points along the periphery. The radiation field of these antennas can consequently be calculated from the voltage distribution [17], [18].

1.2   PRESENT INVESTIGATIONS

The investigations reported in this thesis are aimed at the extension of Green's function approach for analysis of segment shapes not analyzed so far and the use of the 2-d analysis in the design and optimization of microwave integrated circuits.

Green's functions have hitherto been known for only rectangular and circular segments [3], [5]. This thesis reports the development of Green's functions for some triangular segments, annular ring segments and some types of sectoral segments. Green's functions for the analysis of triangular segments are developed in Chapter Three. Three types of triangles (30° - 60° right-angled, equilateral, and right-angled isosceles) are considered by placing additional image sources outside the triangular regions. Green's functions for circular sectors, annular rings and annular sector shaped segments are developed in Chapter Four.

Segmentation method for the analysis of 2-d circuits involves breaking up of a circuit pattern into segments for which Green's functions are known. The scattering matrix for the overall circuit is computed from the S-matrices of individual components [3], [4]. In this method, a considerable effort is spent in computing S-matrices for each of the components. These matrices are then combined to obtain the overall S-matrix. Considerable reduction in computational effort can be achieved if the Z-matrices of individual components are combined to give the overall Z-matrix from which the overall network scattering matrix may be determined. Segmentation method that combines Z-matrices of individual components is described in Chapter Five.

Two-dimensional resonators are used in MIC's. Resonant structures of simple geometrical shapes such as rectangular, circular disk and annular ring are used extensively in MIC's [19] - [21]. Planar triangular resonators have been studied by Helszajn and James [9]. Spectral domain analysis of hexagonal and other microstrip resonant structures has been reported [8], [22]. The 2-d approach can be used for the analysis of these resonators. The voltages around the periphery and input impedances for various modes can be obtained. Triangular, rhombic and hexagonal resonators have been analyzed using this approach in Chapter Six.

Two-dimensional approach has been used to analyze stripline and microstrip discontinuities [13]. The approach can be used for the compensation of these discontinuities. T-junction discontinuity is studied in Chapter Seven. Normally, a rectangular geometry is used at the junction. It has been shown that triangular geometry can be used to reduce the junction parasitics.

Stripline and microstrip circuits can be analyzed more accurately using 2-d approach. A 3 db branch-line hybrid has been analyzed using 2-d approach in [3], [4]. This analysis can be used in the optimization procedure to obtain improved designs of circuits. Improved designs for 3 db in-phase power dividers and 3 db branch-line hybrid have been reported in Chapter Eight.

Chapter Nine summarizes the new findings reported in the thesis and suggests several further extensions of this work.

Chapter Two

ANALYSIS USING GREEN'S FUNCTIONS AND SEGMENTATION

This chapter presents a review of the Green's function approach [1] and the segmentation method [3],[4] for the analysis of two-dimensional planar circuits.

2.1 BASIC CONCEPTS

Consider a two-dimensional circuit shown in Fig. 2.1. An arbitrary shaped thin conductor is sandwiched midway between two ground conductors spaced 2d apart. There are several ports along the periphery. Widths of these ports are denoted as W_i, W_j, ... The rest of the periphery is open-circuited. The xy coordinates are selected parallel to and the z-axis is chosen perpendicular to the conducting plates. Thus, while the dimensions along x and y coordinates are comparable to (or greater than) the wavelength, the thickness along the z-direction is negligible. Therefore, the fields can be assumed to be constant along the z-direction.

The general Helmholtz equation, valid for a source free region, is given as[*]

$$(\nabla^2 + k^2)\underline{E} = 0, \qquad k^2 = \omega^2 \mu \varepsilon \qquad (2.1)$$

where μ and ε denote the permeability and permittivity of the dielectric material and ω is the angular frequency. The above

_____

[*]Underlined symbols throughout the thesis indicate vectors or matrices.
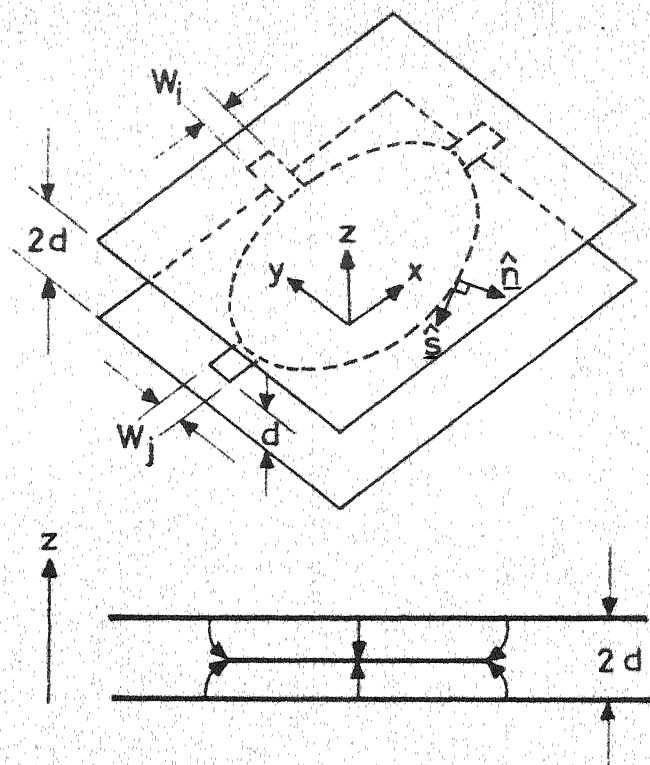
Fig. 2.1   Configuration of a stripline type 2-d circuit
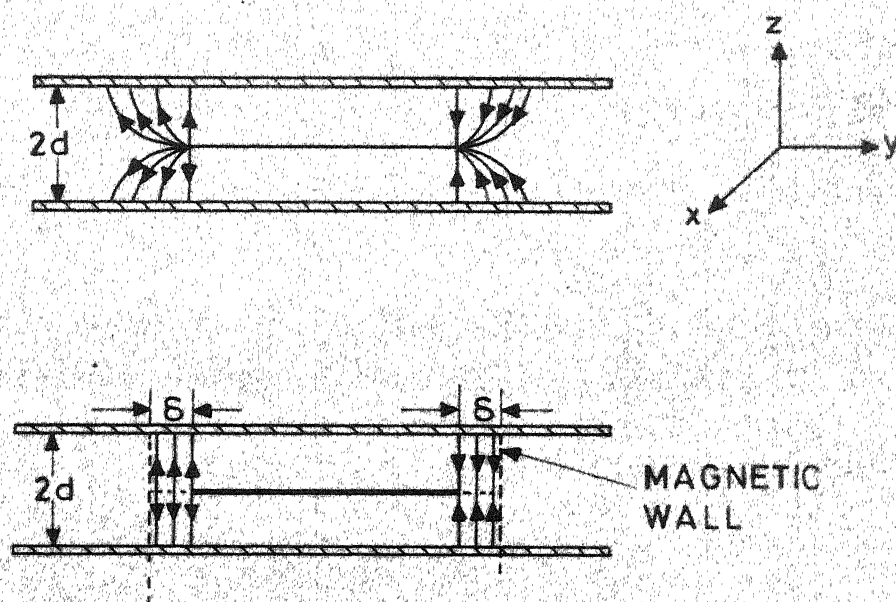
Fig. 2.2   Shift in the magnetic wall to account for the fringing field.

relation holds good for describing the field within the dielectric. At the center conductor and at the ground planes the tangential components of the electric field are zero. A magnetic wall is assumed to exist at the periphery of the 2-d component. Since the fields do not vary along the z-direction, both E_x and E_y are equal to zero within the dielectric region. The fringing field at the periphery is taken into account by shifting the magnetic wall by a certain distance from the physical periphery. This shift is shown in Fig. 2.2. For stripline type planar circuits, the shift δ in the magnetic wall is given by [11]

$$\delta = \frac{2d \, \ell n \, 2}{\pi} .$$

(2.2)

This value of δ is exact for a semi-infinite patch only, but it can be used in most practical cases. For microstrip type circuits, the value of δ is found from the expression for the fringing capacitance at an open-ended microstrip [12].

It may be noted that the fields above and below the central patch must be oppositely directed. In the discussions below, the $\underline{E}$ and $\underline{H}$ can be taken to be the fields on one side of the central patch, say the lower side.

Since E_x and E_y are zero, the E-field may be written as

$$\underline{E} = \hat{\underline{a}}_z \, E_z(x,y)$$

(2.3)

where $\hat{\underline{a}}_z$ is a unit vector along the z-direction, and E_z is a function of x and y coordinates only. Substituting (2.3) in

(2.1) and putting $\partial E_z / \partial z$ equal to zero, one obtains

$$(\nabla_T^2 + k^2)E_z = 0 \qquad (2.4)$$

where $\nabla_T^2 = \dfrac{\partial^2}{\partial x^2} + \dfrac{\partial^2}{\partial y^2}$. Using Maxwell's equation, the magnetic field can be written as

$$\underline{H} = - \frac{1}{j\omega\mu} \ \nabla \times \underline{E} \qquad (2.5)$$

which, using (2.3), reduces to

$$\underline{H} = \frac{1}{j\omega\mu} \left(- \frac{\partial E_z}{\partial y} \ \hat{\underline{a}}_x + \frac{\partial E_z}{\partial x} \ \hat{\underline{a}}_y \right) \qquad (2.6)$$

where $\hat{\underline{a}}_x$ and $\hat{\underline{a}}_y$ are unit vectors along the x and the y coordinates respectively.

Surface current on a conducting sheet can be obtained from the boundary condition

$$\underline{J}_s = \hat{n} \times (\underline{H}_1 - \underline{H}_2) \qquad (2.7)$$

where $\hat{n}$ is a unit vector normal to the boundary and $\underline{H}_1$ and $\underline{H}_2$ are magnetic fields on the two sides of a conducting sheet. For the central conductor of a stripline type 2-d circuit, $\underline{H}_1 = -\underline{H}_2$ and thus

$$\underline{J}_s = \frac{2}{j\omega\mu} \left(\frac{\partial E_z}{\partial x} \ \hat{\underline{a}}_x + \frac{\partial E_z}{\partial y} \ \hat{\underline{a}}_y \right) \ \text{amps/m} . \qquad (2.8)$$

For microstrip type planar circuits (after the periphery has been extended to take care of the fringing fields), there is no magnetic field above the upper conducting plane and so the factor of 2 in (2.8) will not appear for obtaining the surface current on the conducting patch.

The expression for $\underline{J}_s$ in (2.8) is valid at all points on the central patch including the periphery. For points on the periphery, $\underline{J}_s$ can be rewritten in terms of components which are normal and tangential to the periphery as

$$\underline{J}_s = \frac{2}{j\omega\mu} \left(\frac{\partial E_z}{\partial s} \hat{\underline{s}} + \frac{\partial E_z}{\partial n} \hat{\underline{n}} \right) \text{ amps/m} \qquad (2.9)$$

where $\hat{\underline{s}}$ and $\hat{\underline{n}}$ are unit vectors tangential and normal to the periphery as shown in Fig. 2.1. For points on the periphery where there are no coupling ports, the normal component of the surface current must be zero, i.e.

$$\frac{\partial E_z}{\partial n} = 0. \qquad (2.10)$$

At a coupling port on the periphery, the planar circuit can be excited by a stripline (or microstrip) and the current flow (at the coupling port) is normal to the periphery. The current flowing in at a coupling port is obtained using (2.9) as

$$i = - \int_W \left(\frac{2}{j\omega\mu} \frac{\partial E_z}{\partial n} \right) ds \qquad (2.11)$$

where W is the width of the coupling port and ds is the incremental distance along the periphery. The negative sign in (2.11) implies that the current i flows inwards whereas $\hat{\underline{n}}$ in (2.9) points outwards.

The characterization of the planar components can be carried out in terms of an RF voltage v on the central conductor. Since $\partial E_z / \partial z = 0$, v is obtained from (2.3) as

$$v = -E_z \, d \, . \tag{2.12}$$

Equations (2.4), (2.10) and (2.11) can now be written as follows :

$$(\nabla_T^2 + k^2)v = 0 \tag{2.13}$$

with

$$\frac{\partial v}{\partial n} = 0 \tag{2.14}$$

for points on the periphery where there are no coupling ports. The current flowing in at a coupling port is expressed as

$$i = \frac{2}{j\omega\mu d} \int_W \frac{\partial v}{\partial n} \, ds . \tag{2.15}$$

Solution to (2.13), with (2.14) and (2.15) as the boundary conditions, leads to the characterization of stripline type of planar components. For microstrip type planar circuits, the boundary condition (2.15) is modified so that the factor of 2 on the right-hand side does not appear. Governing equations for waveguide type of planar circuits can be obtained by using similar procedure.

2.2 GREEN'S FUNCTION APPROACH

This approach can be employed when the shape of the 2-d patch is relatively simple. The Green's function, which gives voltage at any point for a unit source current excitation elsewhere, is obtained analytically. When the locations of the ports are specified, the impedance matrix of the component can be easily derived using the Green's function.

2.2.1 Source Currents

If a planar component is excited by a current density J_z in z-direction at any arbitrary point (x_o, y_o) inside the periphery (as shown in Fig. 2.3), the wave equation can be written as

$$(\nabla_T^2 + k^2)v = -j\omega\mu \, d \, J_z \, . \tag{2.16}$$

When the circuit is excited by a stripline, J_z denotes a fictitious RF current density injected normally into the circuit. It may be noted that the line current density $(J_n = \dfrac{2}{j\omega\mu d} \dfrac{\partial v}{\partial n})$, being injected into the circuit at coupling ports located on the periphery, can equivalently be considered as fed normal to the circuit (along the z-direction) with the magnetic wall condition $\partial v/\partial n = 0$ imposed all along the periphery. This can be explained as follows. When the stripline is connected to a coupling port, there is some amount of current in the central strip which flows into the planar component. One half of this current flows in the opposite direction in each of the two ground planes. At the boundary where the strip is connected to the planar component, it may be considered that the current loops close by equivalent currents along the z-direction. Figure 2.4 shows the representation of tangential magnetic field (shown as ------) at the interface between planar circuit and the connecting line by an equivalent current density J_s (shown as _____) in z-direction. These equivalent currents may be evaluated as given below. At the periphery, the magnetic
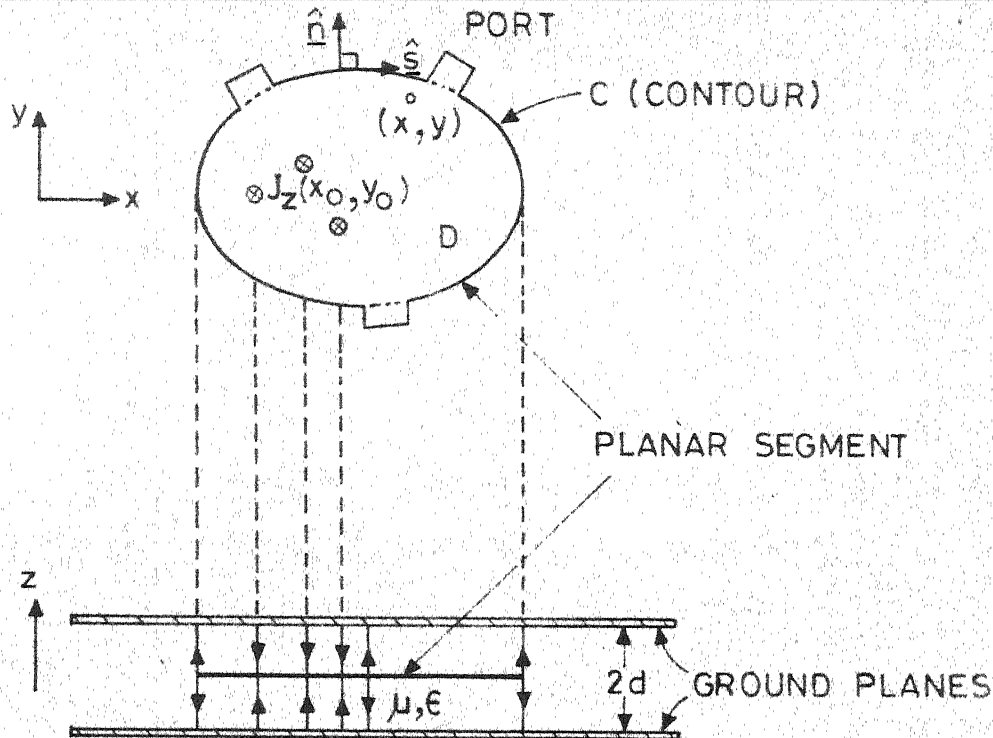
Fig. 2.3 Current sources $J_z(x_o, y_o)$ and field point (x, y)
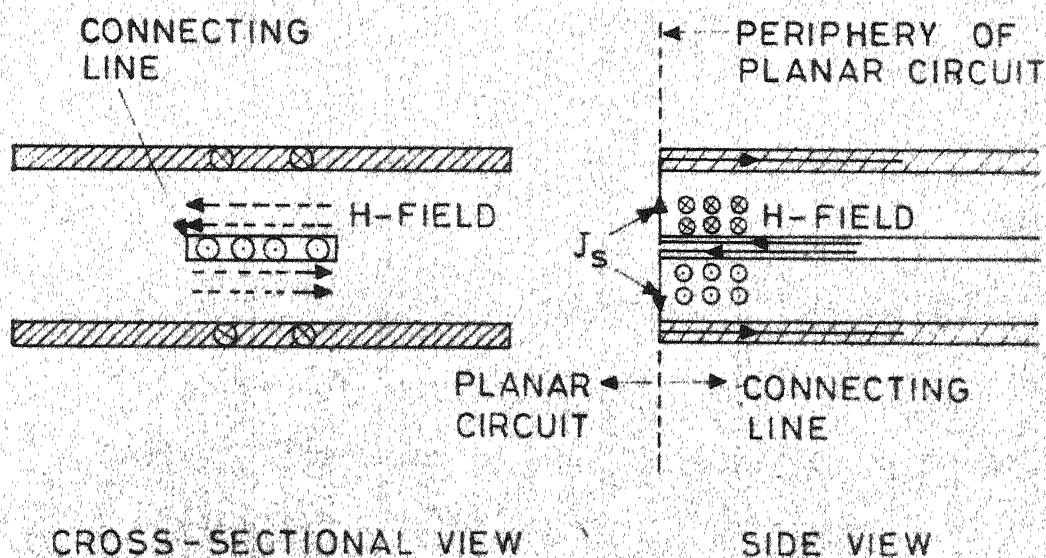
Fig. 2.4 Representation of H_{tan} by an equivalent current density J_s.

field can be written from (2.6) and (2.12) as

$$\underline{H} = \frac{1}{j\omega\mu d} \left(\frac{\partial v}{\partial n} \hat{\underline{s}} - \frac{\partial v}{\partial s} \hat{\underline{n}}\right).$$
(2.17)

This must equal the magnetic field on the other side of the interface between the planar segment and the feeding line. If the magnetic wall condition is imposed all along the periphery of the planar component, the tangential component of magnetic field at the periphery is modelled to be zero. In the present model, there is a change in magnetic field at the periphery (where coupling ports are located) and the equivalent fictitious surface current J_s in the z-direction, obtained from the boundary condition (2.7), may be written as

$$\underline{J}_s = -\frac{1}{j\omega\mu d} \frac{\partial v}{\partial n} \hat{\underline{a}}_z \quad \text{amps/m.}$$
(2.18)

$\underline{J}_s$ is in the negative z-direction in the region below the conducting patch as shown in Fig. 2.4. The planar component may now be considered to be excited by line currents along z-direction at the coupling ports and $\frac{\partial v}{\partial n} = 0$ can be imposed all along the periphery.

2.2.2 Green's Functions and Impedance Matrix

The Green's function $G(\underline{r}|\underline{r}_0)$ for (2.16) is obtained by applying a unit line current source $\delta(\underline{r} - \underline{r}_0)$ flowing along the z-direction in the region below the central patch and located at $\underline{r} = \underline{r}_0$. The Green's function $G(\underline{r}|\underline{r}_0)$ is a solution of

$$(\nabla_T^2 + k^2)G(\underline{r}|\underline{r}_0) = -j\omega\mu d \, \delta(\underline{r} - \underline{r}_0)$$
(2.19)

with the boundary condition at the periphery given by

$$\frac{\partial G}{\partial n} = 0 \ . \tag{2.20}$$

Equations (2.19) and (2.20) yield the Green's functions for both stripline type and microstrip type 2-d components. The voltage at any point on the planar component may now be written as

$$v(x,y) = \iint_D G(x,y \mid x_0,y_0) \ J_z(x_0,y_0) \ dx_0 \ dy_0 \tag{2.21}$$

where $J_z(x_0,y_0)$ denotes a source current density (real or fictitious) injected normally and D denotes the region of the planar component enclosed by magnetic walls.

When the source current is fed only at ports on the periphery, the voltage v at the periphery can be written in terms of line current J_s in z-direction (given by (2.18)) as

$$v(s) = - \int_C G(s \mid s_0) \ J_s(s_0) \ ds_0 \tag{2.22}$$

where s and s_0 are the distances measured along the periphery and the integral on the right-hand side is over the entire periphery. Since the line current $J_s(s_0)$ is present only at the coupling ports, equation (2.22) may be written as

$$v(s) = - \sum_j \int_{W_j} G(s \mid s_0) \ J_s(s_0) \ ds_0 \tag{2.23}$$

where the summation on the right-hand side is over all the coupling ports and W_j indicates the width of the jth coupling port. From (2.15) and (2.18), the current i_j fed in at the

jth port can be written in terms of the equivalent line current in the z-direction as

$$i_j = -2 \int_{W_j} J_s(s_o) \, ds_o. \tag{2.24}$$

If the widths of the coupling ports are assumed to be small so that the line current density J_s is distributed uniformly over the width of the port, using (2.24) one gets

$$J_s(s_o)\Big|_{\text{for jth port}} = -\frac{i_j}{2W_j}. \tag{2.25}$$

Substituting (2.25) in (2.23), $v(s)$ is obtained as

$$v(s) = \sum_j \frac{i_j}{2W_j} \int_{W_j} G(s|s_o) \, ds_o. \tag{2.26}$$

Equation (2.26) gives voltage at any point on the periphery. To obtain the voltage v_i at the ith coupling port, average voltage over the width of the port is taken, i.e.

$$v_i = \frac{1}{W_i} \int_{W_i} v(s) \, ds$$

$$= \sum_j \frac{i_j}{2W_i W_j} \int_{W_j} \int_{W_j} G(s|s_o) \, ds_o \, ds. \tag{2.27}$$

From (2.27) above, the elements of the impedance matrix of the planar component can be written as

$$z_{ij} = \frac{1}{2W_i W_j} \int_{W_i} \int_{W_j} G(s|s_o) \, ds_o \, ds. \tag{2.28}$$

The impedance matrix of a component is thus determined using the Green's function. The scattering matrix may be evaluated from the Z-matrix as [23]

$$\underline{S} = [\sqrt{Y_o}] \ (\underline{Z} - \underline{Z}_o)(\underline{Z} + \underline{Z}_o)^{-1} \ [\sqrt{Z_o}] \qquad (2.29)$$

where $\underline{Z}_o$, $[\sqrt{Z_o}]$ and $[\sqrt{Y_o}]$ are diagonal matrices with diagonal elements given by Z_{o1}, Z_{o2}, ..., Z_{oN}; $\sqrt{Z_{o1}}$, $\sqrt{Z_{o2}}$, ..., $\sqrt{Z_{oN}}$; and $1/\sqrt{Z_{o1}}$, $1/\sqrt{Z_{o2}}$, ..., $1/\sqrt{Z_{oN}}$ respectively. Z_{o1}, Z_{o2}, ..., Z_{oN} represent the normalizing impedances at various ports of the network.

2.2.3 Green's Functions for Rectangular and Circular Segments

Green's functions have hitherto been known for only rectangular and circular segments. The Green's function for the rectangle shown in Fig. 2.5(a) is given as [3]

$$G(x,y|x_o,y_o) = \frac{j\omega\mu d}{ab}$$

$$\sum_{-\infty}^{\infty} \sum_{-\infty}^{\infty} \frac{\cos(k_x \ x_o) \ \cos(k_y \ y_o) \ \cos(k_x \ x) \ \cos(k_y \ y)}{k_x^2 + k_y^2 - k^2} \qquad (2.30)$$

where $k_x = \frac{m\pi}{a}$ and $k_y = \frac{n\pi}{b}$. The Green's function for the circle shown in Fig. 2.5(b) is given as [5]

$$G(\rho, \phi | \rho_o, \phi_o) = \frac{d}{j\omega\varepsilon\pi a^2} +$$

$$j\omega\mu d \sum_{n=0}^{\infty} \sum_{m=1}^{\infty} \frac{\sigma J_n(k_{nm} \rho_o) J_n(k_{nm}\rho) \ \cos[n(\phi - \phi_o)]}{\pi(a^2 - n^2/k_{nm}^2)(k_{nm}^2 - k^2) \ J_n^2(k_{nm} \ a)} \qquad (2.31)$$
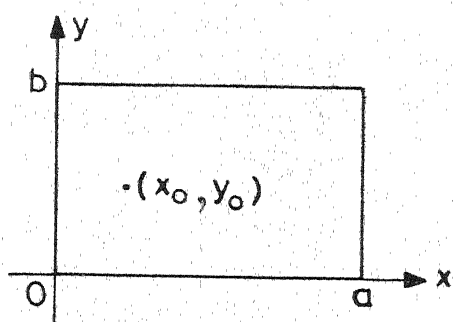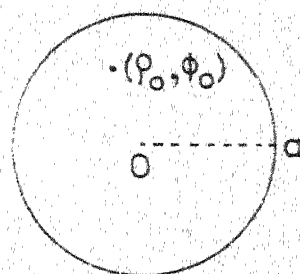
Fig . 2.5 Rectangular and a circular segment .
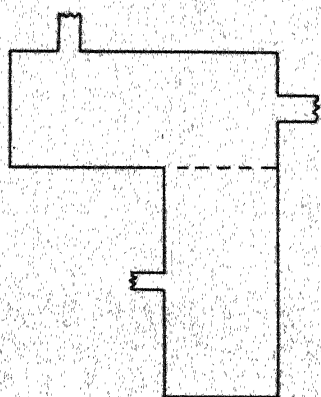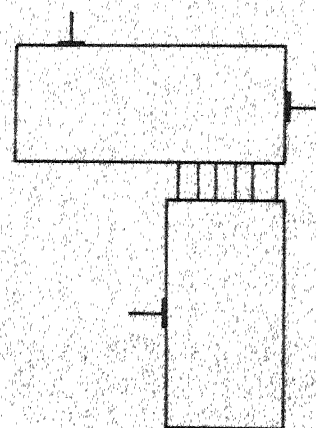
Fig . 2.6   Segmentation   method .

where $J_n(\cdot)$ represents Bessel's function of nth order, σ is
1 for n=0 and 2 otherwise, and k_{nm} satisfy

$$\frac{\partial}{\partial\rho} J_n(k_{nm}\rho)\Big|_{\rho=a} = 0. \qquad (2.32)$$

The subscript m in k_{nm} denotes the mth root of (2.32). For
zeroth order Bessel's function first root of (2.32) is taken
to be the nonzero root.

2.3 SEGMENTATION METHOD [3], [4]

The Green's function approach discussed above cannot be
applied to more general shapes whose Green's functions are
not known. In many cases, however, the circuit pattern can be
considered to be made up of simpler shapes whose Green's
functions are known. In such cases, the analysis may be
carried out by using the segmentation method [3],[4].Using
this method, the continuous connections at the boundaries of
simpler shapes (which constitute the circuit pattern) are
replaced by the multiple number of ports covering the entire
interconnections. The characteristics of circuit obtained
by this analysis converge to the actual circuit characteristics
when a large number of ports are considered at the inter-
connections.

To illustrate the segmentation method, an example of a
2-d circuit shown in Fig. 2.6(a) is taken. The circuit shape
can be considered to be made up of two rectangles. The circuit
characteristics can be obtained by considering two rectangular

components joined at discrete number of ports as shown in Fig. 2.6(b).

The circuit characteristics are obtained by combining S-matrices of the simpler shapes joined together. The overall S-matrix can be obtained from individual S-matrices by the methods used for analyzing multiport circuits. In the multiport connection method [24], the S-matrices of the individual components are put together as

$$
\begin{bmatrix} \underline{b}_p \\ \underline{b}_c \end{bmatrix} = \begin{bmatrix} \underline{S}_{pp} & \underline{S}_{pc} \\ \underline{S}_{cp} & \underline{S}_{cc} \end{bmatrix} \begin{bmatrix} \underline{a}_p \\ \underline{a}_c \end{bmatrix} \tag{2.33}
$$

where $\underline{a}_p$, $\underline{b}_p$ and $\underline{a}_c$, $\underline{b}_c$ are normalized wave variables at the p external and c internal connected ports. The interconnection constraints are put together as

$$
\underline{b}_c = \underline{\Gamma} \, \underline{a}_c \tag{2.34}
$$

where $\underline{\Gamma}$ is the connection matrix whose elements are all null except the 1's in the entries corresponding to pairs of adjacent ports. By eliminating $\underline{b}_c$ and $\underline{a}_c$ from (2.33) and (2.34), one obtains

$$
\underline{b}_p = \underline{S}_p \, \underline{a}_p \tag{2.35}
$$

where

$$
\underline{S}_p = \underline{S}_{pp} + \underline{S}_{pc} \, (\underline{\Gamma} - \underline{S}_{cc})^{-1} \, \underline{S}_{cp} \tag{2.36}
$$

is the scattering matrix of the circuit at its p ports.

The Green's function approach has been extended to some of the triangular and sectoral shapes in Chapters Three and Four. The segmentation method discussed herein is modified in Chapter Five resulting in a procedure where various operations performed are in terms of impedance matrices.

Chapter Three

GREEN'S FUNCTIONS FOR TRIANGULAR SEGMENTS

This chapter describes the development of Green's functions for some of the triangular segments used in two-dimensional planar circuits. For a given shape of 2-d component, derivation of the Green's function requires solution of (2.19) with the boundary condition (2.20). Product of delta functions $\delta(x-x_0)\,\delta(y-y_0)$, *contained* in the right-hand side of (2.19), represents a line current flowing along z-direction and located at (x_0,y_0). Such sources have been called line sources in this chapter.

In circuits, which are symmetrical about a plane, the concept of even and odd modes can be used to simplify the analysis of the circuit. For the odd mode half-section, the plane of symmetry is replaced by an electric wall at which the boundary condition

$$G = 0 \qquad\qquad (3.1)$$

is satisfied. Thus, there is need to obtain odd mode Green's functions which satisfy (3.1) on the electric wall and (2.20) on the remaining sides of the planar segment.

The method of images has been employed to obtain the Green's functions derived in this chapter.

3.1 METHOD OF IMAGES [25]

An analytical solution of the differential equation (2.19) is obtained by making the right-hand side a periodic function. For this purpose, additional line sources of the type $\delta(x-x_s)$ $\cdot \delta(y-y_s)$ are placed at points (x_s, y_s) outside the region of the planar component. The additional sources can be thought of as obtained by taking multiple images of the line source at (x_o, y_o) with respect to various walls of the planar component. The sign of an image source depends on the type of wall across which the image is being taken. The sign of the image source is same for an image across a magnetic wall and is reversed for an image across an electric wall. The source term in (2.19) gets modified and the boundary conditions are satisfied by the voltage v produced by the source and its images. The additional sources should be all outside the region of the planar component so that the solution for G still represents the Green's function for the geometrical shape of the 2-d component. The method cannot be applied to cases where any of the multiple images fall within the region of the planar component itself.

With these additional images, the source pattern used in (2.19) becomes periodic and can be expanded in Fourier series. The Green's function can then be expressed as an infinite series summation of the functions obtained in the Fourier series expansion. These are the eigenfunctions of equation (2.13) for the given boundary conditions. The coefficients in the series

summation for Green's function can then be obtained by substituting these series expansions in (2.19).

The Green's functions for some triangular shapes are now obtained using the method of images.

3.2 GREEN'S FUNCTION FOR $30^{\circ}-60^{\circ}$ RIGHT-ANGLED TRIANGLE

For the triangular geometry shown in Fig. 3.1(a), the Green's function can be obtained by solving (2.19) with the boundary conditions given by (2.20). The additional image sources are obtained by taking multiple images of the line source at (x_0, y_0) with respect to the three sides of the triangle which are magnetic walls. The locations of these multiple images are shown in Fig. 3.1 (b).

It can be seen that the periodicity of the pattern is 3a along the y-direction and $\sqrt{3}a$ along the x-direction. Hence, ABCDEFGH is chosen as a basic cell which contains 24 line sources (all positive*) in 24 triangular regions as shown in Fig. 3.1(b). It may be noted that a solution for G with this set of multiple sources will satisfy (2.19) in the original region of interest.

For the line source (x_0, y_0) at P in Fig. 3.1(b), the coordinates of the image line sources in ODEF can be expressed in terms of (x_0, y_0) as

---

*Since the source at P is positive.

Fig. 3.1 (a) A 30°–60° right–angled triangle and (b) location of image sources

$$x_I = \frac{x_o}{2} - \frac{\sqrt{3}}{2} y_o + \frac{a\sqrt{3}}{4}$$

$$y_I = -\frac{\sqrt{3}}{2} x_o - \frac{y_o}{2} + \frac{3a}{4}$$

for image I

$$x_{II} = \frac{x_o}{2} + \frac{\sqrt{3}}{2} y_o + \frac{a\sqrt{3}}{4}$$

$$y_{II} = -\frac{\sqrt{3}}{2} x_o + \frac{y_o}{2} + \frac{3a}{4}$$

for image II

$$x_{III} = -\frac{x_o}{2} - \frac{\sqrt{3}}{2} y_o + \frac{a\sqrt{3}}{4}$$

$$y_{III} = \frac{\sqrt{3}}{2} x_o - \frac{y_o}{2} + \frac{3a}{4}$$

for image III

$$x_{IV} = -\frac{x_o}{2} + \frac{\sqrt{3}}{2} y_o + \frac{a\sqrt{3}}{4}$$

$$y_{IV} = \frac{\sqrt{3}}{2} x_o + \frac{y_o}{2} + \frac{3a}{4}$$

for image IV

$$x_V = -x_o + \frac{a\sqrt{3}}{2}$$

$$y_V = -y_o + \frac{3a}{2}$$

for image V

Coordinates for the other image sources can be directly obtained from these by using symmetry about the axes.

The Fourier series expressions for each of the 24 line sources, which repeat periodically in the two-dimensional space, are obtained. The corresponding terms of these 24 expressions are added together and the resulting expression, identical to the right-hand side of (2.19) in the original triangular region, can be expressed as

$$- \frac{8j\omega\mu d}{3\sqrt{3}a^2} \sum_{m=-\infty}^{\infty} \sum_{n=-\infty}^{\infty} \cos(k_1 mx) \cos[k_2(m+2n)y]$$

$$\cdot \{(-1)^n \cos[k_1(m+n)x_0] \cos[k_2(m-n)y_0]$$

$$+ \cos(k_1 m x_0) \cos[k_2(m+2n)y_0] +$$

$$(-1)^{m+n} \cos(k_1 n x_0) \cos[k_2(2m+n)y_0] \} \tag{3.2}$$

where

$$k_1 = \frac{2\pi}{\sqrt{3}a} \tag{3.3a}$$

and

$$k_2 = \frac{2\pi}{3a} . \tag{3.3b}$$

Now substituting $\ell = -(m+n)$, expression (3.2) reduces to

$$- \frac{8j\omega\mu d}{3\sqrt{3}a^2} \sum_{-\infty}^{\infty} \sum_{-\infty}^{\infty} (-1)^m \cos(k_1 mx) \cos[k_2(n-\ell)y] \; T_1(x_0, y_0) \tag{3.4}$$

where $T_1(x,y)$ is defined as

$$T_1(x,y) = (-1)^\ell \cos(k_1 \ell x) \cos[k_2(m-n)y] +$$

$$(-1)^m \cos(k_1 mx) \cos[k_2(n-\ell)y] +$$

$$(-1)^n \cos(k_1 nx) \cos[k_2(\ell-m)y] \tag{3.5}$$

with the condition that the integers ℓ, m, and n satisfy

$$\ell + m + n = 0 \tag{3.6}$$

and k_1, k_2 are given by (3.3). It can be seen that

$$\sum \sum (-1)^{\ell} \cos(k_1 \ell x) \cos[k_2(m-n)y] \, T_1(x_0,y_0)$$

$$= \sum \sum (-1)^m \cos(k_1 m x) \cos[k_2(n-\ell)y] \, T_1(x_0,y_0)$$

$$= \sum \sum (-1)^n \cos(k_1 n x) \cos[k_2(\ell-m)y] \, T_1(x_0,y_0) . \qquad (3.7)$$

Using (3.7), expression (3.4) can be rewritten as

$$- \frac{8j\omega\mu d}{9\sqrt{3}a^2} \sum \sum T_1(x_0,y_0) \, T_1(x,y). \qquad (3.8)$$

It can be verified that the functions $T_1(x,y)$ satisfy the boundary condition, given by (2.20), for the triangle shown in Fig. 3.1(a). The functions $T_1(x,y)$ are the eigenfunctions for this triangle. These eigenfunctions agree with the potential functions for an equilateral triangle given by Schelkunoff [26]. The Green's function G can be written in terms of these eigenfunctions as

$$G(x,y|x_0,y_0) = \sum_{m=-\infty}^{\infty} \sum_{n=-\infty}^{\infty} A_{mn} \, T_1(x,y) . \qquad (3.9)$$

Substituting (3.9) in the left-hand side of (2.19) and using (3.6), one gets

$$(\nabla_T^2 + k^2)G = \sum_{-\infty}^{\infty} \sum_{-\infty}^{\infty} [k^2 - \frac{16\pi^2}{9a^2}(m^2+mn+n^2)] \, A_{mn} \, T_1(x,y). (3.10)$$

Since (3.10) and (3.8) are equal for all values of x and y, the values of A_{mn} are obtained by comparison as

$$A_{mn} = \frac{8j\omega\mu d \, T_1(x_0,y_0)}{16\sqrt{3}\pi^2(m^2+mn+n^2) - 9\sqrt{3}a^2k^2} . \qquad (3.11)$$

Substituting (3.11) in (3.9), one obtains

$$G(x,y \mid x_0,y_0) = 8j\omega\mu d \sum_{-\infty}^{\infty} \sum_{-\infty}^{\infty} \frac{T_1(x_0,y_0)\, T_1(x,y)}{16\sqrt{3}\pi^2(m^2+mn+n^2) - 9\sqrt{3}a^2k^2}$$

$$(3.12)$$

which is the required Green's function for (2.19) for the $30°$-$60°$ right-angled triangle shown in Fig. 3.1(a).

3.3 GREEN'S FUNCTION FOR AN EQUILATERAL TRIANGLE

As in the previous section, the right-hand side of (2.19) can be made periodic by placing additional line sources outside the equilateral triangle shown in Fig. 3.2(a). The positions of additional line sources are obtained by taking multiple images of the original line source at (x_0,y_0) with respect to magnetic walls at the three sides of the triangle. In this case also, the periodicity of the pattern is $3a$ along the y-direction and $\sqrt{3}a$ along the x-direction. The basic cell which repeats itself is ABCDEF which contains 12 line sources (all positive) in the 12 triangular regions as shown in Fig. 3.2(b).
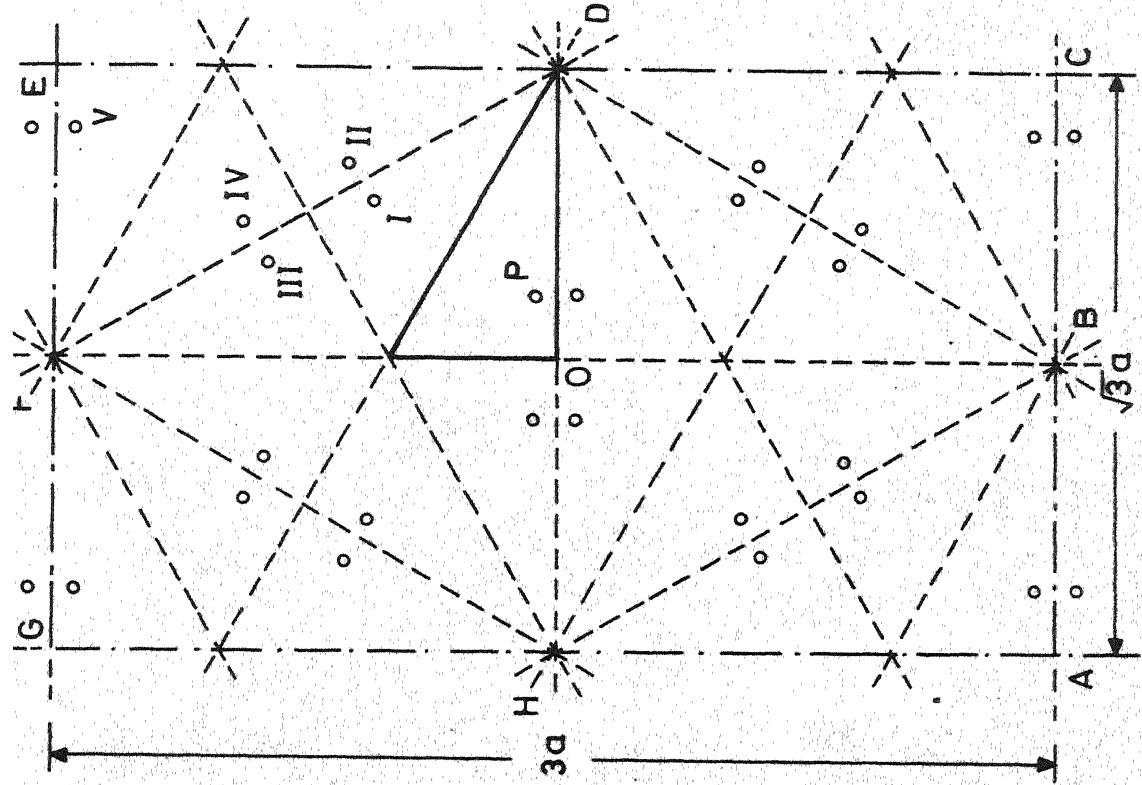
For the line source (x_0,y_0) at P in Fig. 3.2(b), the coordinates of the image line sources in BCDE can be expressed in terms of (x_0,y_0) as

$$x_I = \frac{x_0}{2} + \frac{\sqrt{3}}{2} y_0 + \frac{a\sqrt{3}}{4}$$

$$y_I = \frac{\sqrt{3}}{2} x_0 - \frac{y_0}{2} - \frac{3a}{4}$$

$\left.\right\}$ for image I

$$x_{II} = \frac{x_0}{2} - \frac{\sqrt{3}}{2} y_0 + \frac{a\sqrt{3}}{4}$$

$$y_{II} = -\frac{\sqrt{3}}{2} x_0 - \frac{y_0}{2} + \frac{3a}{4}$$
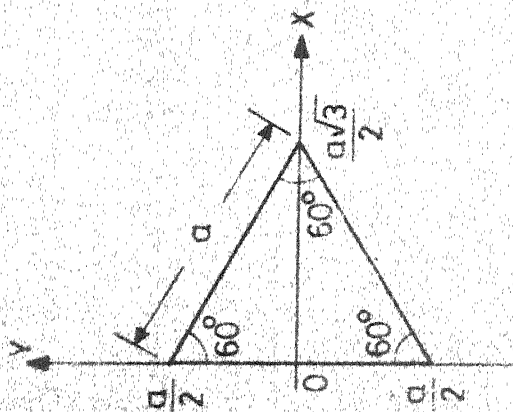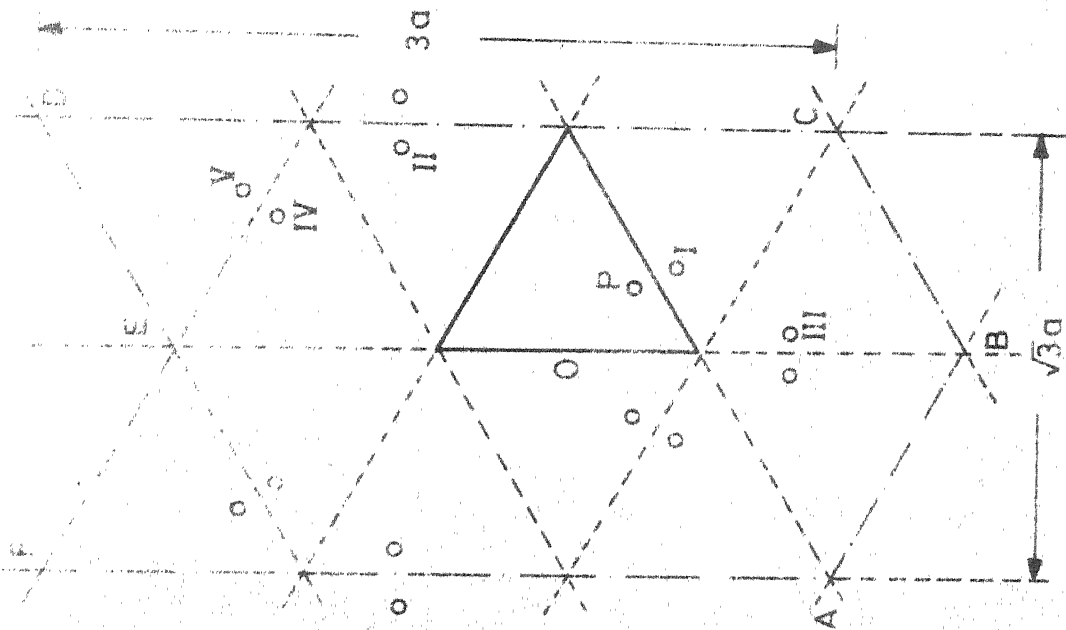
$\left.\right\}$ for image II

Fig. 3.2 (a) An equilateral triangle and (b) location of image sources

$$x_{III} = -\frac{x_o}{2} + \frac{\sqrt{3}}{2} y_o + \frac{a\sqrt{3}}{4}$$

$$y_{III} = -\frac{\sqrt{3}}{2} x_o - \frac{y_o}{2} - \frac{3a}{4}$$

for image III

$$x_{IV} = -\frac{x_o}{2} - \frac{\sqrt{3}}{2} y_o + \frac{a\sqrt{3}}{4}$$

$$y_{IV} = \frac{\sqrt{3}}{2} x_o - \frac{y_o}{2} + \frac{3a}{4}$$

for image IV

$$x_V = -x_o + \frac{a\sqrt{3}}{2}$$

$$y_V = y_o + \frac{3a}{2} .$$

for image V

Coordinates for the other image sources in the basic cell can be directly obtained from these by using symmetry about the y-axis.

Adding the corresponding terms in Fourier series expressions for each of the line sources in the basic cell, the resulting expression equivalent to the right-hand side of (2.19) can be expressed as

$$-\frac{4j\omega\mu d}{3\sqrt{3}a^2} \sum_{m=-\infty}^{\infty} \sum_{n=-\infty}^{\infty} \left[\cos(k_1 mx) \cos[k_2(m+2n)y] \right.$$

$$\cdot \{ (-1)^n \cos[k_1(m+n)x_o] \cos[k_2(m-n)y_o]$$

$$+ \cos(k_1 mx_o) \cos[k_2(m+2n)y_o]$$

$$+ (-1)^{m+n} \cos(k_1 nx_o) \cos[k_2(2m+n)y_o] \} +$$

$$\cos(k_1 mx) \sin[k_2(m+2n)y] \{ \cos(k_1 mx_o) \sin[k_2(m+2n)y_o]$$

$$- (-1)^{m+n} \cos(k_1 nx_o) \sin[k_2(2m+n)y_o] +$$

$$\left. (-1)^n \cos[k_1(m+n)x_o] \sin[k_2(m-n)y_o] \} \right]$$

(3.13)

where k_1 and k_2 are given by (3.3). Now substituting $\ell = -(m+n)$, the above expression can be rewritten as

$$-\frac{4j\omega\mu d}{3\sqrt{3}a^2} \sum \sum \Big[(-1)^m \cos(k_1 mx) \cos[k_2(n-\ell)y] \, T_1(x_0,y_0)$$

$$+ (-1)^m \cos(k_1 mx) \sin[k_2(n-\ell)y] \, T_2(x_0,y_0)\Big] \qquad (3.14)$$

where $T_2(x,y)$ is defined as

$$T_2(x,y) = (-1)^\ell \cos(k_1 \ell x) \sin[k_2(m-n)y]$$

$$+ (-1)^m \cos(k_1 mx) \sin[k_2(n-\ell)y]$$

$$+ (-1)^n \cos(k_1 nx) \sin[k_2(\ell-m)y] . \qquad (3.15)$$

Integers ℓ, m and n in (3.15) may be chosen as in the case of $T_1(x_0,y_0)$, to satisfy (3.6). It can be seen that

$$\sum \sum (-1)^\ell \cos(k_1 \ell x) \sin[k_2(m-n)y] \, T_2(x_0,y_0)$$

$$= \sum \sum (-1)^m \cos(k_1 mx) \sin[k_2(n-\ell)y] \, T_2(x_0,y_0)$$

$$= \sum \sum (-1)^n \cos(k_1 nx) \sin[k_2(\ell-m)y] \, T_2(x_0,y_0) . \qquad (3.16)$$

Using (3.7) and (3.16), the expression (3.14) reduces to

$$-\frac{4j\omega\mu d}{9\sqrt{3}a^2} \sum \sum [T_1(x_0,y_0) \, T_1(x,y) + T_2(x_0,y_0) \, T_2(x,y)]. \quad (3.17)$$

It can be verified that both the functions $T_1(x,y)$ and $T_2(x,y)$ satisfy the boundary condition (2.20) for the equilateral triangle geometry shown in Fig. 3.2(a). It is seen that $T_1(x,y)$ has even symmetry about the x-axis and $T_2(x,y)$ has odd symmetry about the x-axis. Since the line current excitation

in the right-hand side of (2.19) is asymmetric, the Green's function should contain terms of both $T_1(x,y)$ and $T_2(x,y)$. Let

$$G(x,y|x_0,y_0) = \sum_{m=-\infty}^{\infty} \sum_{n=-\infty}^{\infty} [A_{mn} T_1(x,y) + B_{mn} T_2(x,y)]. \quad (3.18)$$

Substituting (3.18) in the left-hand side of (2.19), one gets

$$(\nabla_T^2 + k^2)G = \sum \sum [k^2 - \frac{16\pi^2}{9a^2}(m^2+mn+n^2)]$$

$$\cdot [A_{mn} T_1(x,y) + B_{mn} T_2(x,y)] . \quad (3.19)$$

Since (3.17) and (3.19) are equal for all values of x and y, the values of A_{mn} and B_{mn} are obtained by comparison as

$$A_{mn} = \frac{4j\omega\mu d\ T_1(x_0,y_0)}{16\sqrt{3}\pi^2(m^2+mn+n^2) - 9\sqrt{3}a^2k^2} \quad (3.20a)$$

and

$$B_{mn} = \frac{4j\omega\mu d\ T_2(x_0,y_0)}{16\sqrt{3}\pi^2(m^2+mn+n^2) - 9\sqrt{3}a^2k^2} . \quad (3.20b)$$

Substituting (3.20) in (3.18), one obtains

$$G(x,y|x_0,y_0) = 4j\omega\mu d$$

$$\cdot \sum_{-\infty}^{\infty} \sum_{-\infty}^{\infty} \frac{T_1(x_0,y_0) T_1(x,y) + T_2(x_0,y_0) T_2(x,y)}{16\sqrt{3}\pi^2(m^2+mn+n^2) - 9\sqrt{3}a^2k^2} \quad (3.21)$$

which is the required Green's function for the equilateral triangle shown in Fig. 3.2(a).

Green's Functions for Even and Odd Mode Half-Sections

First term in the right-hand side of (3.21) corresponds to the Green's function for 30^0-60^0 right-angled triangle given by (3.12). The second term in (3.21) can be identified

as one half of the Green's function for the odd mode half-section of the equilateral triangle (i.e. a 30°-60° right-angled triangle shown in Fig. 3.1(a) with the side OB being an electric wall). This Green's function may be explicitly expressed as

$$G(x,y|x_o,y_o) = 8j\omega\mu d$$

$$\cdot \sum_{-\infty}^{\infty} \sum_{-\infty}^{\infty} \frac{T_2(x,y_o)\ T_2(x,y)}{16\sqrt{3}\pi^2(m^2+mn+n^2) - 9\sqrt{3}a^2k^2} \quad . \tag{3.22}$$

3.4 GREEN'S FUNCTIONS FOR AN ISOSCELES RIGHT-ANGLED TRIANGLE

As in earlier cases, additional line sources are placed outside the isosceles right-angled triangle shown in Fig. 3.3(a). The positions of additional images are shown in Fig. 3.3(b). The basic cell ABCD contains 8 line sources (all positive) in 8 triangular regions. For the line source (x_o,y_o) at P in Fig. 3.3(b), the coordinates of the image line source I can be expressed in terms of (x_o,y_o) as

$$x_I = a - y_o$$

$$y_I = a - x_o .$$

Coordinates of the other line sources in ABCD can be directly obtained from these by using symmetry about the axes.

Adding the corresponding terms in the Fourier series expressions for each of the line sources in the basic cell, the resulting expression can be expressed as
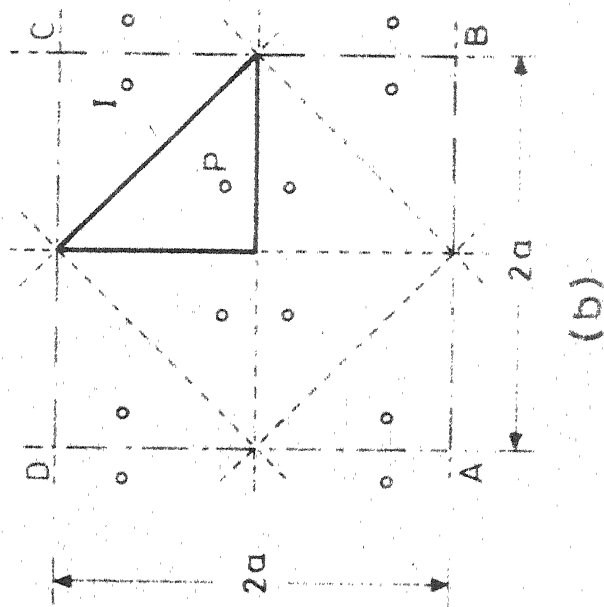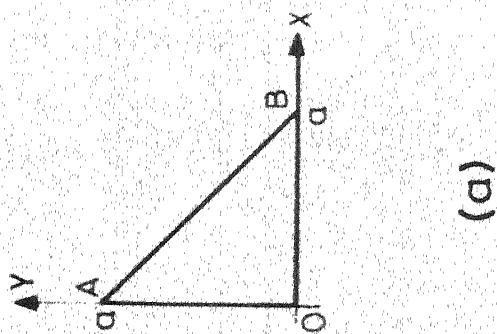
Fig. 3.3 (a) An isosceles right-angled triangle and
(b) location of image sources.

$$- \frac{j\omega\mu d}{a^2} \sum_{m=-\infty}^{\infty} \sum_{n=-\infty}^{\infty} \cos \frac{m\pi x}{a} \cos \frac{n\pi y}{a} \, T(x_0,y_0) \qquad (3.23)$$

where the eigenfunction $T(x,y)$ is given by

$$T(x,y) = \cos \frac{m\pi x}{a} \cos \frac{n\pi y}{a} + (-1)^{m+n} \cos \frac{n\pi x}{a} \cos \frac{m\pi y}{a}. \quad (3.24)$$

The function $T(x,y)$ satisfies the boundary condition (2.20) for the triangle of Fig. 3.3(a).

As in the previous section, expression (3.23) can be simplified to

$$- \frac{j\omega\mu d}{2a^2} \sum_{-\infty}^{\infty} \sum_{-\infty}^{\infty} T(x_0,y_0) \, T(x,y) \, . \qquad (3.25)$$

As before, G can be expressed as

$$G = \sum_{-\infty}^{\infty} \sum_{-\infty}^{\infty} A_{mn} \, T(x,y) \, . \qquad (3.26)$$

The left-hand side of (2.19), then reduces to

$$\sum_{-\infty}^{\infty} \sum_{-\infty}^{\infty} A_{mn} \left[k^2 - \left(\frac{m\pi}{a}\right)^2 - \left(\frac{n\pi}{a}\right)^2 \right] T(x,y) \, . \qquad (3.27)$$

The values of A_{mn} are obtained by equating (3.25) and (3.27). The Green's function is given by

$$G(x,y|x_0,y_0) = \sum_{-\infty}^{\infty} \sum_{-\infty}^{\infty} \frac{j\omega\mu d \, T(x_0,y_0) \, T(x,y)}{2[(m^2+n^2)\pi^2 - a^2 k^2]} \qquad (3.28)$$

which is the required Green's function for an isosceles right-angled triangle shown in Fig. 3.3(a).

A. Green's Function for Odd Mode Half-Section

The odd mode triangle for the present case has the same

shape as shown in Fig. 3.3(a), with the side OB as an electric wall where (3.1) should be satisfied and other sides are magnetic walls where (2.20) should be satisfied. Additional line sources are placed by taking multiple images of the original line source at (x_0, y_0) with respect to various walls of the triangle. In this case, the basic cell which repeats itself is ABCD which contains 32 line sources as shown in Fig. 3.4. The signs of the line sources are also shown. Following the steps similar to those in the earlier cases, the Green's function for this case is given by

$$G(x,y \mid x_0, y_0) = 2j\omega\mu d \sum_{\substack{-\infty \\ \text{odd}(m,n)}}^{\infty} \sum_{-\infty}^{\infty} \frac{U(x_0, y_0)\, U(x,y)}{[(m^2+n^2)\pi^2 - 4a^2 k^2]} \qquad (3.29)$$

where the summation is carried out for odd values of m and n, and

$$U(x,y) = \cos \frac{m\pi x}{2a} \sin \frac{n\pi y}{2a} - (-1)^{\frac{m+n}{2}} \cos \frac{n\pi x}{2a} \sin \frac{m\pi y}{2a}. \qquad (3.30)$$

Even mode half-section of an isosceles right-angled triangle has the same shape as the original segment. Green's function given in (3.28) may be used for this case also.

B. Green's Function when Hypotenuse is an Electric Wall

An isosceles right-angled triangle, with the hypotenuse as an electric wall and the other two sides being magnetic walls, would be needed for odd mode analysis of a square having symmetry about one of its diagonals. For example, for the square planar segments shown in Fig. 3.5, the odd mode triangle
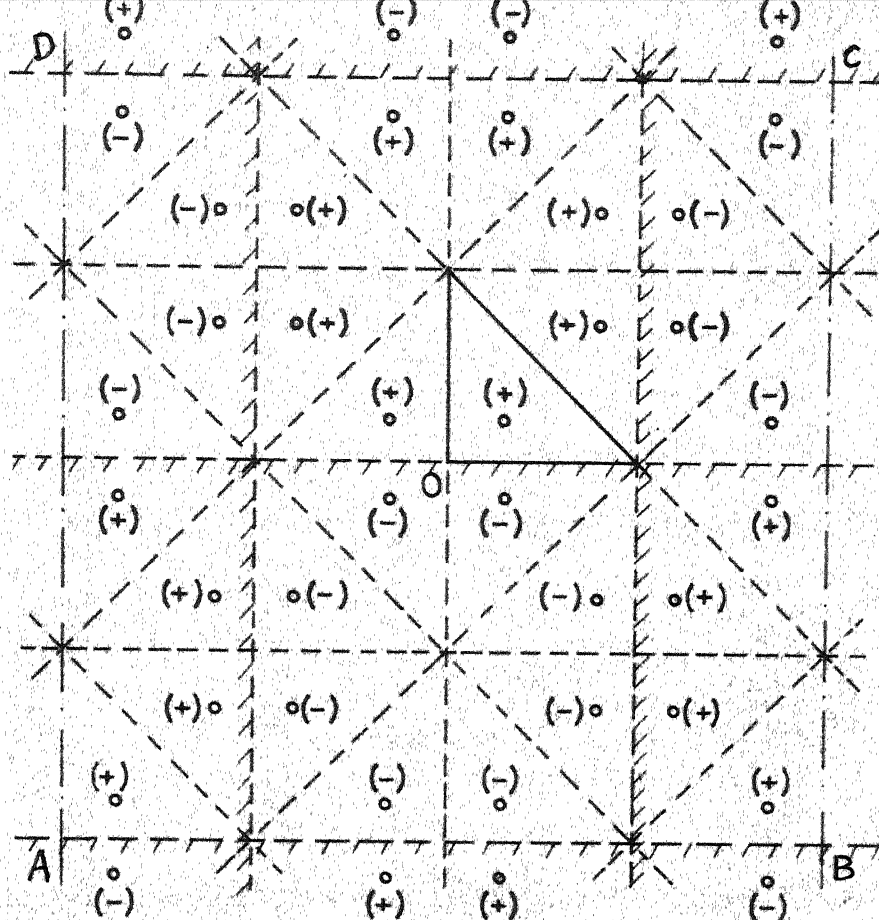
Fig. 3.4   Image sources for odd mode half-section
of isosceles right-angled triangle.
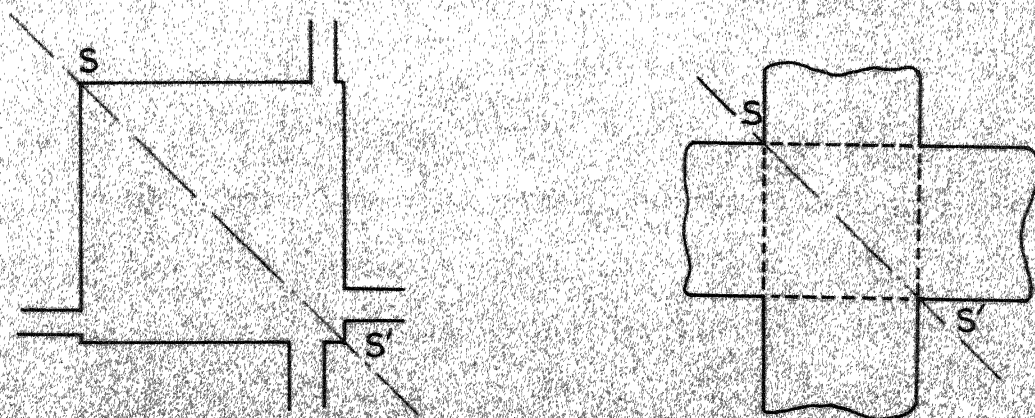
Fig. 3.5   Square segments with symmetry about
the diagonal.

would be a right-angled isosceles shown in Fig. 3.3(a). For this case, the boundary condition (3.1) is valid on the hypotenuse AB and on the other two sides (2.20) is satisfied. The positions of the additional sources (alongwith the sign) are shown in Fig. 3.6. The basic cell which repeats itself is ABCD. By carrying out steps similar to those in the earlier cases, the Green's function is found to be

$$G(x,y \mid x_0,y_0) = \sum_{m=-\infty}^{\infty} \sum_{n=-\infty}^{\infty} \frac{j\omega\mu d \; W(x_0,y_0) \; W(x,y)}{2[(m^2+n^2)\pi^2 - a^2 k^2]} \qquad (3.31)$$

where

$$W(x,y) = \cos\frac{m\pi x}{a} \cos\frac{n\pi y}{a} - (-1)^{m+n} \cos\frac{n\pi x}{a} \cos\frac{m\pi y}{a}. \quad (3.32)$$

3.5 GREEN'S FUNCTION FOR RECTANGLE (ODD MODE)

A rectangle, with one side as an electric wall and the other three sides being magnetic walls, would be needed for odd mode analysis of a rectangle having symmetry about an axis parallel to and midway between two of its sides. For example, for the rectangular planar segment shown in Fig. 3.7(a), the odd mode half-section would be a rectangle as shown in Fig. 3.7(b). For this case, the boundary condition (3.1) is valid on the side OA and on the other three sides (2.20) is satisfied. By carrying out steps similar to those in the earlier cases, the Green's function is found to be
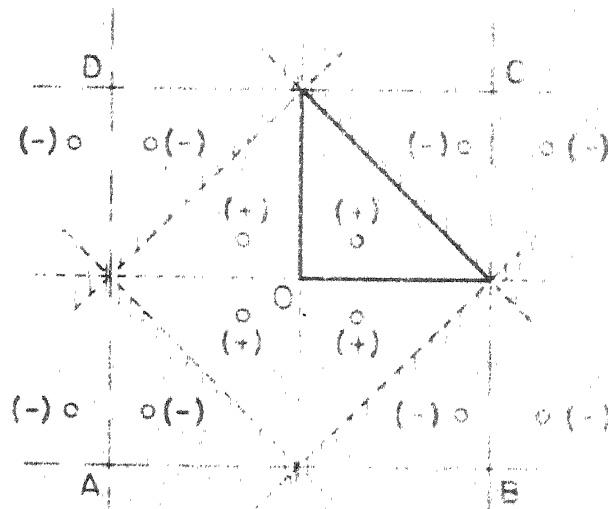
Fig. 3.6 Image sources for isosceles right-angled triangle with hypotenuse as electric wall.
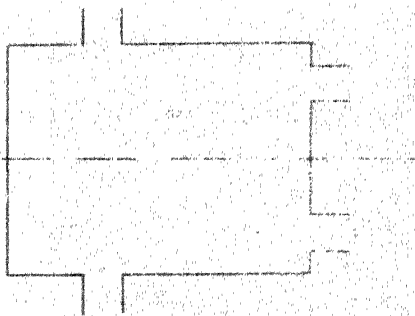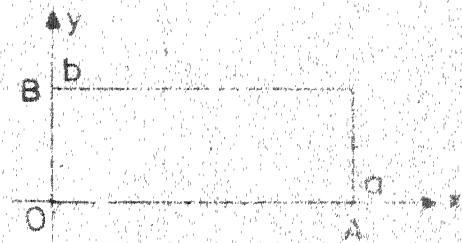
(a) (b)

Fig. 3.7 (a) Rectangular segment with symmetry and (b) rectangle with electric wall on one side.

$$G(x,y|x_0,y_0) = \frac{j\omega\mu d}{ab}$$

$$\cdot \sum_{\substack{m=-\infty}}^{\infty} \sum_{\substack{n=-\infty \\ odd\ n}}^{\infty} \frac{\cos(k_x x_0)\ \sin(k_y y_0)\ \cos(k_x x)\ \sin(k_y y)}{(k_x^2 + k_y^2 - k^2)}$$

$$(3.33)$$

where the summation is carried out for only odd values of n and all values of m, and

$$k_x = \frac{m\pi}{a} \quad ; \quad k_y = \frac{n\pi}{2b} \quad .$$

3.6 DISCUSSION

The method of images used in this chapter is restricted to the shapes enclosed by boundaries which are straight lines. This is because the only mirror surface which gives a point image for a point source is a plane mirror. Only for a few polygonal shapes, the images can be uniquely specified without any ·of the image sources falling within the region of the planar segment. If all sides of the polygon are magnetic walls or all sides are electric walls, the internal angle at each vertex should be a submultiple of 180°. For polygons with mixed boundary conditions (i.e. some sides as electric walls and rest magnetic walls) the angles at all vertices where one side is electric wall and the other magnetic wall should be 90° or a submultiple of 90°. Other vertices should have angles which are submultiples of 180°. Thus, the method of images is restricted to rectangular and the triangular shapes discussed.

In reducing the right-hand side of (2.19) to a periodic function, one of the factors obtained, viz. $T_1(x,y)$ in (3.8), $T_2(x,y)$ in (3.17), $T(x,y)$ in (3.25), $U(x,y)$ in (3.29), $W(x,y)$ in (3.31) and $\cos(k_x x) \sin(k_y y)$ in (3.33), is the eigenfunction which satisfies the boundary conditions. Thus, this part of the procedure may be used in evaluation of eigenfunctions in similar cases.

The procedure employing the method of images can also be used for finding Green's functions for planar segments with all short circuit boundaries reported in [27]. A similar procedure can be used for finding Green's function for Poisson's equation also.

The Green's functions for some of the triangular planar segments developed in this chapter may be used to analyze multiport circuits using triangular segments. Other two-dimensional shapes which can be segmented into these types of triangles (and circular and rectangular geometries) can also be analyzed using the segmentation method [3], [4].

These Green's functions have been used for the analysis of triangular, rhombic and hexagonal resonators in Chapter Six, and for the analysis of triangular T-junctions in Chapters Seven and Eight.

Chapter Four

GREEN'S FUNCTIONS FOR CIRCULAR SECTORS,
ANNULAR RINGS AND ANNULAR SECTORS

In this chapter, Green's functions are obtained for circular sector, annular ring and annular sector shaped segments. Annular ring structures have been proposed for use in microstrip antennas [17] and are used in circuits like ratrace hybrids. The circular and annular sectors are used in microstrip bends as shown in Fig. 4.1, and their characterizations are needed to analyze these bends accurately. Also, the characterization of an annular sector can be used to analyze accurately a tapered line segment as shown in Fig. 4.2. The Green's functions of these geometries have not been available so far.

The Green's functions developed in this chapter have been obtained by expansion in series of eigenfunctions. These Green's functions are valid both for triplate stripline type and for open microstrip type circuits.

4.1 EXPANSION OF GREEN'S FUNCTION IN EIGENFUNCTIONS [25]

The Green's function $G(\underline{r}|\underline{r}_0)$ is given by the solution of (2.19) with the boundary condition (2.20). In this method, the Green's function is expanded in terms of known eigenfunctions of the corresponding Helmholtz's equation given by (2.13) and (2.14).
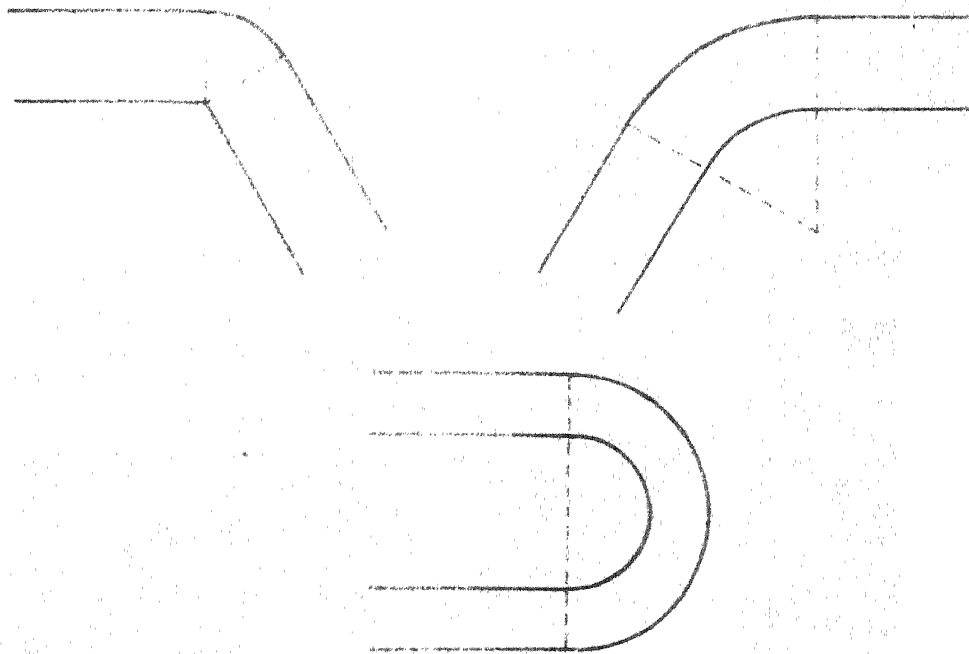
Fig. 4.1   Circular and annular sectors in
stripline/microstrip bends.
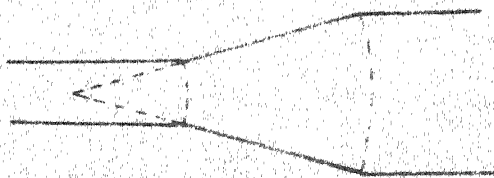
Fig. 4.2   Tapered line section modeled by
an annular sector.

Let ψ_n represent the normalized eigenfunctions of (2.13), which satisfy (2.14), and let k_n^2 be the corresponding eigenvalues so that

$$\nabla_T^2 \, \psi_n + k_n^2 \, \psi_n = 0 \qquad\qquad (4.1)$$

where n represents the two indices defining a particular ψ_n. The normalised eigenfunctions ψ_n form an orthonormal set, such that

$$\iint_D \psi_n^* \, \psi_m \, dx \, dy = \begin{cases} 1 \, , & \text{if } n = m \\ 0 \, , & \text{otherwise} \end{cases} \qquad\qquad (4.2)$$

where the superscript $*$ denotes complex conjugate, and the region of integration D is bounded by the periphery of the planar component, at which ψ_n's satisfy the boundary condition $\partial\psi_n/\partial n = 0$. The Green's function G satisfies similar boundary conditions given by (2.20). Assuming that the functions ψ_n form a complete set of orthonormal functions, it is possible to expand $G(\underline{r}|\underline{r}_0)$ in a series of ψ_n. Let

$$G(\underline{r}|\underline{r}_0) = \sum_m A_m \, \psi_m(\underline{r}) \, . \qquad\qquad (4.3)$$

Substituting (4.3) into (2.19), and using (4.1), one gets

$$\sum_m A_m(k^2 - k_m^2) \, \psi_m(\underline{r}) = -j\omega\mu d \, \delta(\underline{r} - \underline{r}_0) \, . \qquad\qquad (4.4)$$

Multiplying both sides of the above equation by $\psi_n^*(\underline{r})$ and integrating over the region D, one obtains

$$\sum_m A_m(k^2 - k_m^2) \iint_D \psi_m(\underline{r}) \, \psi_n^*(\underline{r}) \, dx \, dy = -j\omega\mu d \, \psi_n^*(\underline{r}_0) \qquad (4.5)$$

which, by virtue of the orthonormal property (4.2), reduces to

$$A_n(k^2 - k_n^2) = -j\omega\mu d\ \psi_n^*(\underline{r}_o) \quad . \tag{4.6}$$

Thus

$$A_n = \frac{j\omega\mu d\ \psi_n^*(\underline{r}_o)}{k_n^2 - k^2} \tag{4.7}$$

so that

$$G(\underline{r}|\underline{r}_o) = j\omega\mu d\ \sum_n \frac{\psi_n(\underline{r})\ \psi_n^*(\underline{r}_o)}{k_n^2 - k^2} \tag{4.8}$$

is the required Green's function expansion. For a lossless circuit, ψ_n are real and the complex conjugate is not needed in (4.8).

This method is restricted to cases where the eigenfunctions are known. As discussed in the previous chapter, for shapes enclosed by straight edges, eigenfunctions can be obtained, only if, the internal angle at each vertex is a submultiple of π. Eigenfunctions can also be obtained for shapes like circles, rings, ellipses, etc. [17].

4.2 CIRCULAR SECTORS

For the circular sector shown in Fig. 4.3, the set of functions which satisfy the boundary conditions is given as

$$f_{\nu m}(\rho,\phi) = J_\nu(k_{\nu m}\rho)\cos\nu\phi \tag{4.9a}$$

$$\nu = n\pi/\alpha \tag{4.9b}$$

where $J_\nu(\cdot)$ represents Bessel's function of νth order, and $k_{\nu m}$ are chosen to satisfy
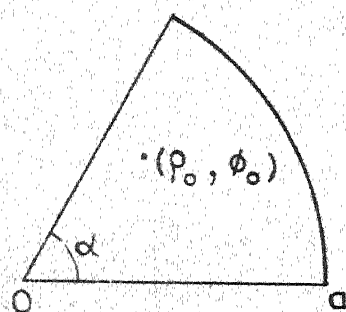
Fig.4.3 A circular sector .

$$J_\nu' (k_{\nu m} a) = 0 . \qquad (4.10)$$

In above, the subscript m denotes the mth root of (4.10), $J_\nu'(\cdot)$ denotes derivative with respect to the argument, and n could be any nonnegative integer. In addition, m can take the value zero for $n = 0$. This corresponds to $k_{\nu m} = 0$ and implies that the function has a value of unity throughout the sector. The set of functions given by (4.9) are, in general, not orthogonal to each other. The functions are orthogonal if, and only if, ν is an integer which implies that π is an integral multiple of α.

Let us consider the case for which $\alpha = \pi/\ell$, where ℓ is a positive integer. The set of functions discussed above are mutually orthogonal since ν takes only integral values. To obtain the Green's function using (4.8), these eigenfunctions must be normalized over the region of the sector. The following integral is used for normalizing the eigenfunction :

$$\int_0^a \rho\, J_{n_i}^2(k_{n_i m} \rho)\, d\rho = \begin{cases} a^2/2 \,, & \text{if } m = n_i = 0 \\[2mm] \text{else } \tfrac{1}{2}[a^2 - n_i^2/k_{n_i m}^2] J_{n_i}^2(k_{n_i m} a) \end{cases} \qquad (4.11)$$

where $n_i = n\ell$, and denotes that ν takes only integral values. Also

$$\int_0^\alpha \cos^2 n_i \phi\, d\phi = \begin{cases} \alpha \,, & \text{if } n_i = 0 \\[2mm] \text{else } \alpha/2 \,. \end{cases} \qquad (4.12)$$

Using (4.11) and (4.12), the Green's function can be written as

$$G(\underline{r}|\underline{r}_0) = \frac{2 \, \ell \, d}{j \omega \epsilon \pi a^2} \; +$$

$$2 j \ell \omega \, \mu d \sum_{n=0}^{\infty} \sum_{m=1}^{\infty} \frac{\sigma_{n_i} \, J_{n_i}(k_{n_i m} \rho_0) J_{n_i}(k_{n_i m} \rho) \, \cos n_i \phi_0 \, \cos n_i \phi}{\pi(a^2 - n_i^2/k_{n_i m}^2)(k_{n_i m}^2 - k^2) \, J_{n_i}^2(k_{n_i m} a)} .$$

$$(4.13)$$

The angle of the sector α equals π/ℓ , and $n_i = n\ell$. The eigenvalues $k_{n_i m}^2$ are given by

$$J_{n_i}'(k_{n_i m} a) = 0 \tag{4.14}$$

and

$$\sigma_{n_i} = \begin{cases} 1, & \text{if } n_i = 0 \\ 2, & \text{if } n_i > 0 . \end{cases} \tag{4.15}$$

For $\ell = 1$, when the sector becomes a semicircle, the Green's function is same as that for the even mode half-section of a circle. Thus the Green's function given by (4.13) is consistent with the Green's function for a circle given in (2.31).

4.3 ANNULAR RINGS

For the annular ring structure shown in Fig. 4.4, the set of mutually orthogonal eigenfunctions, which satisfy the boundary condition (2.14) on the periphery, is given by

$$f_{nm}(\rho, \phi) =$$
$$[N_n'(k_{nm} a) \, J_n(k_{nm} \rho) - J_n'(k_{nm} a) \, N_n(k_{nm} \rho)] \begin{cases} \cos n\phi \\ \sin n\phi \end{cases} \tag{4.16}$$
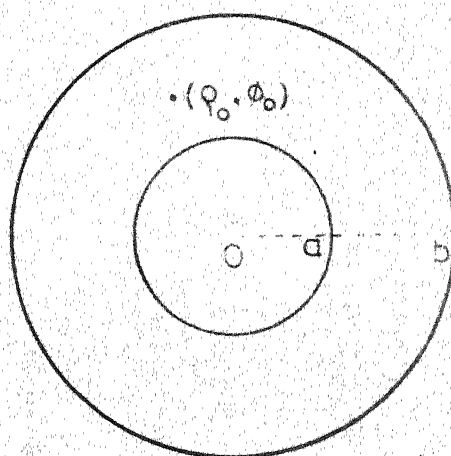
Fig. 4.4 An annular ring.

where $N_n(\cdot)$ denotes Neumann's function of order n, and $N_n'(\cdot)$ denotes derivative with respect to the argument. The eigenvalues k_{nm}^2 are obtained from

$$\frac{J_n'(k_{nm}a)}{N_n'(k_{nm}a)} = \frac{J_n'(k_{nm}b)}{N_n'(k_{nm}b)} \ . \tag{4.17}$$

As in (4.10), n takes nonnegative integral values and m takes positive integral values in the above equation also. In addition, m can take the value zero for $n = 0$, and this corresponds to a unity value of f_{nm} throughout the region and $k_{nm} = 0$.

To obtain the Green's function using (4.8), the eigenfunctions described by (4.16) are normalized using

$$\int_a^b \rho \, [N_n'(k_{nm}a) \, J_n(k_{nm}\rho) - J_n'(k_{nm}a) \, N_n(k_{nm}\rho)]^2 \, d\rho \ =$$

$$\tfrac{1}{2} \{(b^2 - \frac{n^2}{k_{nm}^2}) \, [N_n'(k_{nm}a) \, J_n(k_{nm}b) - J_n'(k_{nm}a) \, N_n(k_{nm}b)]^2$$

$$- (a^2 - \frac{n^2}{k_{nm}^2})[N_n'(k_{nm}a) \, J_n(k_{nm}a) - J_n'(k_{nm}a) \, N_n(k_{nm}a)]^2 \} \tag{4.18}$$

and usual normalizing relations for $\cos n\phi$ and $\sin n\phi$. The Green's function for the annular ring can now be written as

$$G(\underline{r}|\underline{r}_0) = \frac{d}{j\omega\varepsilon\pi(b^2-a^2)} +$$

$$j\omega\mu d \sum_{n=0}^{\infty} \sum_{m=1}^{\infty} \frac{\sigma_n \, F_{nm}(\rho_0) \, F_{nm}(\rho) \, \cos[n(\phi-\phi_0)]}{\pi[\,(b^2-n^2/k_{nm}^2)F_{nm}^2(b) - (a^2-n^2/k_{nm}^2)F_{nm}^2(a)\,](k_{nm}^2-k^2)} \tag{4.19}$$

where $F_{nm}(\rho)$ is defined as

$$F_{nm}(\rho) = N'_n(k_{nm}a) \, J_n(k_{nm}\rho) - J'_n(k_{nm}a) \, N_n(k_{nm}\rho) \qquad (4.20)$$

and k_{nm} are chosen to satisfy (4.17).

To use this Green's function for analyzing an annular ring, (4.17) has to be solved repeatedly to obtain k_{nm}'s.

4.4 ANNULAR SECTORS

The Green's functions for annular sectors (shown in Fig. 4.5) can be obtained in the same way as for circular sectors. The set of functions which satisfy the boundary conditions is given by

$$f_{\nu m}(\rho,\phi) = [N'_\nu(k_{\nu m}a) \, J_\nu(k_{\nu m}\rho) - J'_\nu(k_{\nu m}a) \, N_\nu(k_{\nu m}\rho)] \cos \nu\phi \qquad (4.21)$$

where $\nu = n\pi/\alpha$, and $k_{\nu m}$ satisfy

$$\frac{J'_\nu(k_{\nu m}a)}{N'_\nu(k_{\nu m}a)} = \frac{J'_\nu(k_{\nu m}b)}{N'_\nu(k_{\nu m}b)} \, . \qquad (4.22)$$

These functions are mutually orthogonal if, and only if, $\alpha = \pi/\ell$, where ℓ is a positive integer. The Green's function can now be written as :

$$G(\underline{r}|\underline{r}_0) = \frac{2 \ell d}{j\omega\epsilon\pi(b^2-a^2)} + 2j\ell\omega\mu d$$

$$\cdot \sum_{n=0}^{\infty} \sum_{m=1}^{\infty} \frac{\sigma_{n_i} F_{n_i m}(\rho_0) \, F_{n_i m}(\rho) \cos n_i \phi_0 \cos n_i \phi}{\pi[(b^2-n_i^2/k^2_{n_i m})F^2_{n_i m}(b)-(a^2-n_i^2/k^2_{n_i m})F^2_{n_i m}(a)] \, (k^2_{n_i m}-k^2)} \, .$$

$$(4.23)$$

The angle of the sector α equals π/ℓ , and $n_i = n\ell$. The function $F_{n_i m}(\rho)$ is given by (4.20) and $k_{n_i m}$ are obtained by
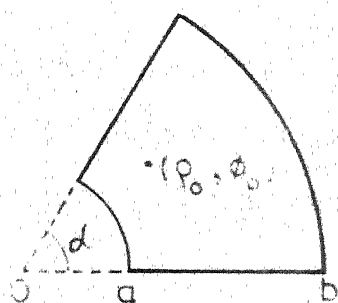
Fig. 4.5 An annular sector

solving (4.22). For $\ell = 1$, when the annular sector becomes
an annular half-ring, the Green's function is same as that for
even mode half-section of an annular ring. Thus, the Green's
function for annular sector is consistent with the Green's
function for annular ring in the same way as the Green's
function for a circular sector is with that of a circle.

4.5 DISCUSSION

Green's functions for circular sectors, annular rings and
annular sectors have been obtained by expansion in series of
known eigenfunctions. Using the Green's functions given by
(4.13), (4.19) and (4.23), the Green's function technique
of analyzing planar circuits and microstrip antennas can be
extended to shapes incorporating circular sectors, annular
rings and annular sectors.

Analysis of circular sector shaped segments using Green's
functions is only as expensive (computationally) as the ana-
lysis of circular segments since the eigenvalues in both cases
are obtained as zeros of the derivatives of Bessel's functions.
For annular ring and annular sector shaped segments, the eigen-
values are obtained by solving the transcedental equations
(4.17) and (4.22) respectively. Corresponding equation has to
be solved for obtaining each eigenvalue k_{nm}^2 or $k_{n_i m}^2$ and thus,
the procedure is computationally expensive.

Chapter Five

SEGMENTATION METHOD USING IMPEDANCE MATRICES

As discussed in Chapter Two, two-dimensional planar
components can be analyzed by the use of Green's functions.
The Green's functions are available for only a few regular
shapes. The technique of segmentation can be employed to
analyze planar circuits of shapes which can be considered
to be made up of those regular shapes. A formulation for
combining segments to form two-port and four-port circuits
is given in [3] and [4] and could be extended to any general
n-port network. In this method a considerable effort is
spent in computing S-matrices for each of the components.
These matrices are then combined to obtain the overall S-
matrix. Considerable reduction in the computational effort
involved can be achieved if Z-matrices of individual compo-
nents are combined to obtain the overall Z-matrix from which
the scattering matrix of the overall network may be deter-
mined. Segmentation procedures that combine Z-matrices of
the components are described in this chapter.

5.1 COMPUTATIONAL EFFORT IN SEGMENTATION USING S-MATRICES

In the segmentation method using S-matrices, the
S-matrices of the individual components are obtained and the
overall S-matrix is computed using the method discussed in
Sec. 2.3. The c-ports in equation (2.33) would refer to the

ports at the boundaries between the regular shaped components.

In this method, the solution of (2.36) requires inversion
of a matrix of order equal to the number of interconnected
ports. Let us consider an example shown in Fig. 5.1 for illu-
strating the total computational effort needed in the segmen-
tation method. This network is a planar circuit version of a
compensated in-line power divider [28]. Segment B and parts
C_1 and C_2 of the segment C are quarter wave transformers with
characteristic impedances equal to $Z_0/(2^{1/4})$ and $(2^{1/4})Z_0$,
respectively. Segments A,D and E are portions of outgoing
transmission lines (with characteristic impedance Z_0). These
three segments are considered as planar components in order
to take into account any higher order modes that may be
excited by the discontinuities in the line width existing at
the ends of three transformers. For better accuracy, each
external port is divided into six subports for obtaining the
Z-matrix. The six subports are combined together using ideal
six-way power dividers (not shown in the figure) at each
external port [3]. To obtain S-matrices of individual seg-
ments, five complex matrices, three of order 12 and one each
of order 14 and 20,are to be inverted. The number of inter-
connections in the network is now 44 and so a complex matrix
of order 88 has to be inverted to obtain the overall scatter-
ing matrix.

It has been pointed out by Monaco and Tiberio [29], that
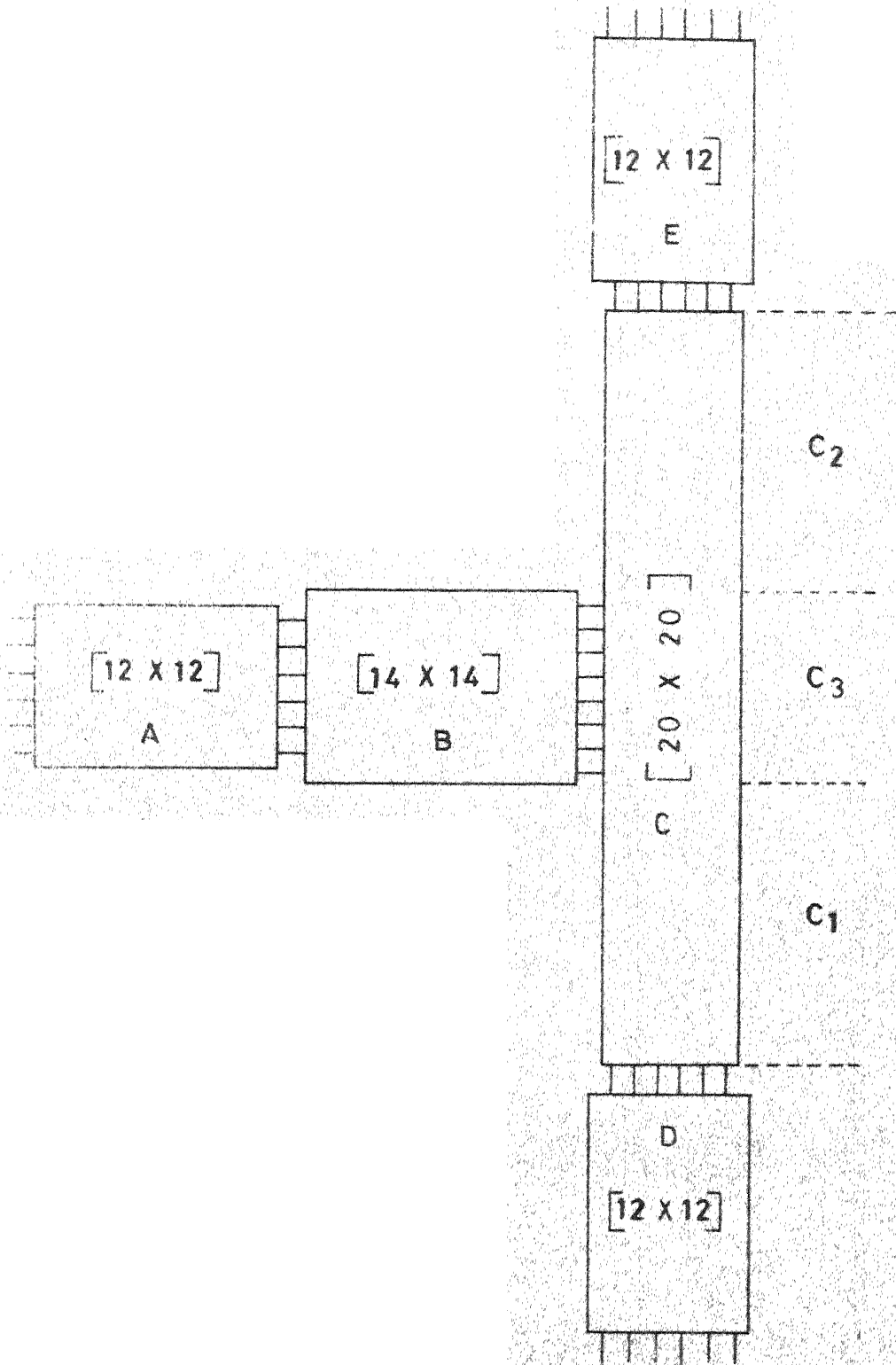
Fig. 5.1 A planar circuit analyzed by segmentation method.

with suitable ordering of rows and columns it is possible to
write the connection matrix in the form

$$\underline{\Gamma} = \begin{bmatrix} \underline{O} & \underline{I} \\ \underline{I} & \underline{O} \end{bmatrix} \qquad (5.1)$$

where $\underline{I}$ is an identity matrix and $\underline{O}$ a null matrix, each of
order $c/2$. They have also pointed out that when two segments
are being interconnected, submatrix $\underline{S}_{cc}$ in (2.33) can be
written in the block diagonal form as

$$\underline{S}_{cc} = \begin{bmatrix} \underline{M} & \underline{O} \\ \underline{O} & \underline{N} \end{bmatrix} \qquad (5.2)$$

where $\underline{M}$ and $\underline{N}$ are $\frac{c}{2} \times \frac{c}{2}$ matrices. In such cases the matrix
$(\underline{\Gamma} - \underline{S}_{cc})$ may be written in the form

$$(\underline{\Gamma} - \underline{S}_{cc}) = \begin{bmatrix} -\underline{M} & \underline{I} \\ \underline{I} & -\underline{N} \end{bmatrix} . \qquad (5.3)$$

The inverse of $(\underline{\Gamma} - \underline{S}_{cc})$ can now be expressed as

$$(\underline{\Gamma} - \underline{S}_{cc})^{-1} = \begin{bmatrix} \underline{N}(\underline{I} - \underline{M}\,\underline{N})^{-1} & (\underline{I} - \underline{N}\,\underline{M})^{-1} \\ (\underline{I} - \underline{M}\,\underline{N})^{-1} & \underline{M}(\underline{I} - \underline{N}\,\underline{M})^{-1} \end{bmatrix} \qquad (5.4)$$

which requires inverse of two matrices of order $\frac{c}{2}$ and thus
results in saving of computational effort [29].

This technique can be extended for interconnection of more than two segments also, if $\underline{S}_{cc}$ can be expressed in the block diagonal form of (5.2). This is possible if the net-work does not contain any loop with odd number of segments in it. The nomenclature 'loop' as used here is a topological term meaning any closed path constituted by segments and connected subports. Two segments joined together by two (or more) subports would constitute a loop with two segments in it. More examples of loops are shown in Fig. 5.2.

In a network, if there is no loop with odd number of segments in it then the above technique can be employed to reduce computational effort. The circuit shown in Fig. 5.1 does not contain any loop at all and combination of S-matrices using (5.4) would require inversion of two complex matrices each of order 44 only.

5.2 SEGMENTATION USING Z-MATRICES

The computational efficiency of segmentation using S-matrices can be improved if the Z-matrices of individual components are combined to yield the overall Z-matrix.

5.2.1 Interconnection Using Z-matrices

In a general network of segments, the Z-matrices of various components can be written together as

$$
\begin{bmatrix} \underline{v}_p \\ \underline{v}_c \end{bmatrix} = \begin{bmatrix} \underline{Z}_{pp} & \underline{Z}_{pc} \\ \underline{Z}_{cp} & \underline{Z}_{cc} \end{bmatrix} \begin{bmatrix} \underline{i}_p \\ \underline{i}_c \end{bmatrix} \tag{5.5}
$$
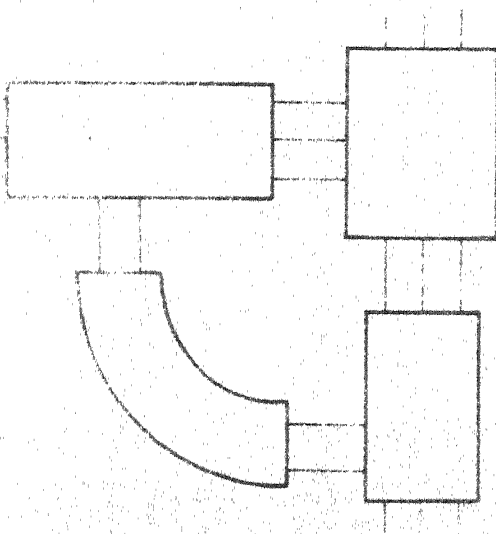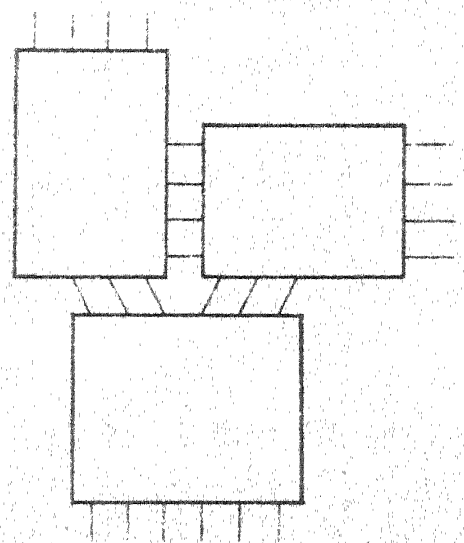
FOUR SEGMENT LOOP   THREE-SEGMENT LOOP

Fig. 5.2 Examples of loops.

where $\underline{v}_p$ and $\underline{i}_p$ are the voltage and the current variables at the p external ports, and $\underline{v}_c$ and $\underline{i}_c$ are the corresponding variables at the internal connected ports. Equation (5.5) does not take into account the constraints imposed by the interconnections. The constraints are : (i) the voltages at the two connected ports are equal and, (ii) the currents are equal and oppositely directed. For all the internal ports, these constraints can be expressed as

$$\underline{\Gamma}_1 \, \underline{v}_c = \underline{0} \qquad\qquad (5.6a)$$

and

$$\underline{\Gamma}_2 \, \underline{i}_c = \underline{0} \qquad\qquad (5.6b)$$

where $\underline{\Gamma}_1$ and $\underline{\Gamma}_2$ matrices with $c/2$ rows and c columns are given by the circuit topology. In these matrices, each row describes a connection such that all elements in a row are zero except the two corresponding to the two connected ports. The two nonzero entries in a row are 1 and -1 for matrix $\underline{\Gamma}_1$. For matrix $\underline{\Gamma}_2$, both of the nonzero entries are 1.

Substituting for $\underline{v}_c$ from (5.5) into (5.6), one obtains

$$\underline{\Gamma}_1 \, \underline{Z}_{cc} \, \underline{i}_c = - \, \underline{\Gamma}_1 \, \underline{Z}_{cp} \, \underline{i}_p. \qquad\qquad (5.7)$$

Multiplying (5.6b) by $j \, (= \sqrt{-1})$ and then combining with (5.7), the relation between $\underline{i}_c$ and $\underline{i}_p$ can be expressed as

$$\begin{bmatrix} \underline{\Gamma}_1 \, \underline{Z}_{cc} \\ \\ j \, \underline{\Gamma}_2 \end{bmatrix} \underline{i}_c = \begin{bmatrix} - \, \underline{\Gamma}_1 \, \underline{Z}_{cp} \\ \\ \underline{0} \end{bmatrix} \underline{i}_p \qquad\qquad (5.8)$$

where $\underline{0}$ is a null matrix with c/2 rows and p columns. In (5.8), the matrix on the left-hand side is a square matrix of order c × c. The current variables $\underline{i}_c$ can thus be written as

$$\underline{i}_c = \begin{bmatrix} \underline{r}_1 \underline{Z}_{cc} \\ j \underline{r}_2 \end{bmatrix}^{-1} \begin{bmatrix} -\underline{r}_1 \underline{Z}_{cp} \\ \underline{C} \end{bmatrix} \underline{i}_p . \qquad (5.9)$$

It should be noted that the Z-matrices for lossless circuits are purely imaginary. Equation (5.6b) was multiplied by j so as to make the matrix to be inverted in (5.9) purely imaginary. Multiplication and inversion of purely imaginary matrices can be carried out with the same computational effort as required for real matrices.

Substituting the expression for $\underline{i}_c$ from (5.9) into (5.5), the overall network impedance matrix is obtained as

$$\underline{Z}_p = \underline{Z}_{pp} - \underline{Z}_{pc} \begin{bmatrix} \underline{r}_1 \underline{Z}_{cc} \\ j\underline{r}_2 \end{bmatrix}^{-1} \begin{bmatrix} \underline{r}_1 \underline{Z}_{cp} \\ \underline{0} \end{bmatrix} . \qquad (5.10)$$

This requires the inversion of a matrix of order equal to the number of interconnected ports. For lossless circuits, this combination requires inversion of a real matrix of order c × c.

5.2.2 Combination Using Subgrouped Interconnections

The computation effort required for combination of Z-matrices can be reduced further if the connected ports are subgrouped as described below.

The 'c' connected ports are divided into groups 'q' and 'r', each containing $c/2$ ports. This is done in such a way that q_1 and r_1 ports are connected together, q_2 and r_2 ports are connected together and so on. This involves reordering of rows and/or columns for $\underline{Z}_{cp}$, $\underline{Z}_{pc}$ and $\underline{Z}_{cc}$ as given in (5.5). The Z-matrices of individual components can now be written together as

$$
\begin{bmatrix} \underline{v}_p \\ \underline{v}_q \\ \underline{v}_r \end{bmatrix} = \begin{bmatrix} \underline{Z}_{pp} & \underline{Z}_{pq} & \underline{Z}_{pr} \\ \underline{Z}_{qp} & \underline{Z}_{qq} & \underline{Z}_{qr} \\ \underline{Z}_{rp} & \underline{Z}_{rq} & \underline{Z}_{rr} \end{bmatrix} \begin{bmatrix} \underline{i}_p \\ \underline{i}_q \\ \underline{i}_r \end{bmatrix} . \tag{5.11}
$$

In this formulation, the interconnection constraints can be expressed in a much simpler form as

$$
\underline{v}_q = \underline{v}_r , \tag{5.12a}
$$

and

$$
\underline{i}_q + \underline{i}_r = \underline{0} . \tag{5.12b}
$$

Substituting (5.12) into (5.11) and eliminating $\underline{v}_p$, $\underline{v}_q$ and $\underline{i}_r$, one obtains

$$
(\underline{Z}_{qq} - \underline{Z}_{qr} - \underline{Z}_{rq} + \underline{Z}_{rr})\underline{i}_q = (\underline{Z}_{rp} - \underline{Z}_{qp})\underline{i}_p
$$

or

$$
\underline{i}_q = (\underline{Z}_{qq} - \underline{Z}_{qr} - \underline{Z}_{rq} + \underline{Z}_{rr})^{-1} (\underline{Z}_{rp} - \underline{Z}_{qp})\underline{i}_p . \tag{5.13}
$$

Substituting (5.13) into the first equation of (5.11) and using $\underline{i}_r = - \underline{i}_q$, the Z-matrix of the overall network is obtained as

$$\underline{Z}_p = \underline{Z}_{pp} + (\underline{Z}_{pq} - \underline{Z}_{pr})(\underline{Z}_{qq} - \underline{Z}_{qr} - \underline{Z}_{rq} + \underline{Z}_{rr})^{-1} (\underline{Z}_{rp} - \underline{Z}_{qp}) \, . \tag{5.14}$$

The relation between $\underline{v}_q$ and $\underline{i}_p$, obtained by substituting (5.13) into the second equation of (5.11), is given as

$$\underline{v}_q = [\underline{Z}_{qp} + (\underline{Z}_{qq} - \underline{Z}_{qr})(\underline{Z}_{qq} - \underline{Z}_{qr} - \underline{Z}_{rq} + \underline{Z}_{rr})^{-1} (\underline{Z}_{rp} - \underline{Z}_{qp})]\underline{i}_p \, . \tag{5.15}$$

In the above formulation, the order of the matrix to be inverted is $c/2$ as compared to the case of (5.10) where a matrix of order c needs to be inverted.

5.2.3 An Example

The two methods of combining Z-matrices are illustrated by combining two three-port resistive subnetworks shown in Fig. 5.3. The Z-matrices of the two components are

$$\underline{Z}_A = \begin{bmatrix} 4 & 3 & 3 \\ 3 & 7 & 3 \\ 3 & 3 & 5 \end{bmatrix} \tag{5.16a}$$

and

$$\underline{Z}_B = \begin{bmatrix} 7 & 3 & 3 \\ 3 & 5 & 3 \\ 3 & 3 & 5 \end{bmatrix} \, . \tag{5.16b}$$

Using the first method for interconnection using Z-matrices, the component characterizations are put in the form
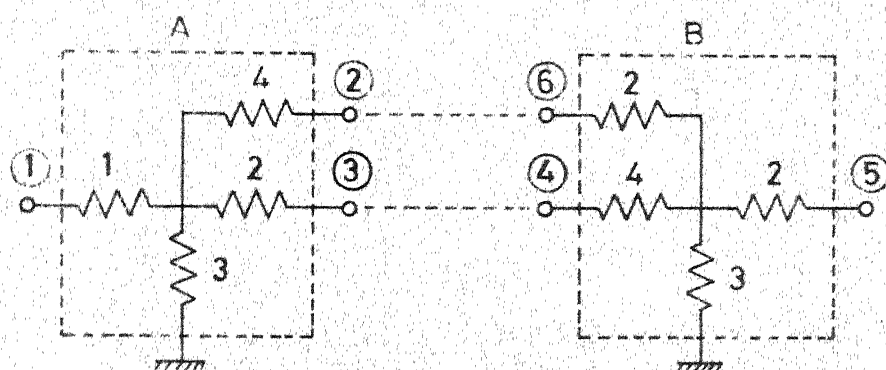
Fig. 5.3 Lumped network example
used for illustration.

$$\begin{bmatrix} v_1 \\ v_5 \\ \hline v_2 \\ v_3 \\ v_4 \\ v_6 \end{bmatrix} = \begin{bmatrix} 4 & 0 & 3 & 3 & 0 & 0 \\ 0 & 5 & 0 & 0 & 3 & 3 \\ \hline 3 & 0 & 7 & 3 & 0 & 0 \\ 3 & 0 & 3 & 5 & 0 & 0 \\ 0 & 3 & 0 & 0 & 7 & 3 \\ 0 & 3 & 0 & 0 & 3 & 5 \end{bmatrix} \begin{bmatrix} i_1 \\ i_5 \\ \hline i_2 \\ i_3 \\ i_4 \\ i_6 \end{bmatrix} . \qquad (5.17)$$

Matrices $\underline{\Gamma}_1$ and $\underline{\Gamma}_2$ are obtained as

$$\begin{bmatrix} 1 & 0 & 0 & -1 \\ 0 & 1 & -1 & 0 \end{bmatrix} \begin{bmatrix} v_2 \\ v_3 \\ v_4 \\ v_6 \end{bmatrix} = \underline{0} \qquad (5.18)$$

and

$$\begin{bmatrix} 1 & 0 & 0 & 1 \\ 0 & 1 & 1 & 0 \end{bmatrix} \begin{bmatrix} i_2 \\ i_3 \\ i_4 \\ i_6 \end{bmatrix} = \underline{0} . \qquad (5.19)$$

The overall Z-matrix is obtained by substituting (5.17) – (5.19) in (5.10). It may be pointed out that the matrix $\underline{\Gamma}_2$ need not be multiplied by j since $\underline{Z}_{cc}$ is real. Thus,

$$\underline{Z}_p = \begin{bmatrix} 4 & 0 \\ 0 & 5 \end{bmatrix} - \begin{bmatrix} 3 & 3 & 0 & 0 \\ 0 & 0 & 3 & 3 \end{bmatrix} \begin{bmatrix} 7 & 3 & -3 & -5 \\ 3 & 5 & -7 & -3 \\ 1 & 0 & 0 & 1 \\ 0 & 1 & 1 & 0 \end{bmatrix}^{-1} \begin{bmatrix} 3 & -3 \\ 3 & -3 \\ 0 & 0 \\ 0 & 0 \end{bmatrix}$$

or

$$\underline{Z}_p = \begin{bmatrix} 4 & 0 \\ 0 & 5 \end{bmatrix} + \frac{1}{108} \begin{bmatrix} -108 & 108 \\ 108 & -108 \end{bmatrix} = \begin{bmatrix} 3 & 1 \\ 1 & 4 \end{bmatrix}. \qquad (5.20)$$

This can be verified to be the Z-matrix of the combination.
For obtaining the Z-matrix of the combination using sub-
grouped interconnections, the connected ports are divided
into two groups as discussed earlier. The Z-matrices for
this purpose can be written together as

$$\begin{bmatrix} v_1 \\ v_5 \\ \hline v_2 \\ v_4 \\ \hline v_6 \\ v_3 \end{bmatrix} = \begin{bmatrix} 4 & 0 & 3 & 0 & 0 & 3 \\ 0 & 5 & 0 & 3 & 3 & 0 \\ \hline 3 & 0 & 7 & 0 & 0 & 3 \\ 0 & 3 & 0 & 7 & 3 & 0 \\ \hline 0 & 3 & 0 & 3 & 5 & 0 \\ 3 & 0 & 3 & 0 & 0 & 5 \end{bmatrix} \begin{bmatrix} i_1 \\ i_5 \\ \hline i_2 \\ i_4 \\ \hline i_6 \\ i_3 \end{bmatrix} \qquad (5.21)$$

and the overall Z-matrix is given by substituting various
submatrices in (5.21) into (5.14),i.e.

$$\underline{Z}_p = \begin{bmatrix} 4 & 0 \\ 0 & 5 \end{bmatrix} + \begin{bmatrix} 3 & -3 \\ -3 & 3 \end{bmatrix} \begin{bmatrix} 12 & -6 \\ -6 & 12 \end{bmatrix}^{-1} \begin{bmatrix} -3 & 3 \\ 3 & -3 \end{bmatrix}$$

$$= \begin{bmatrix} 4 & 0 \\ 0 & 5 \end{bmatrix} + \begin{bmatrix} -1 & 1 \\ 1 & -1 \end{bmatrix} = \begin{bmatrix} 3 & 1 \\ 1 & 4 \end{bmatrix} \qquad (5.22)$$

which is the Z-matrix of the combination.

5.2.4 Combination of External Subports

In many circuits (e.g. in Fig. 5.1), the external ports are divided into multiple subports for higher accuracy. The combination of Z-matrices as discussed in Sections 5.2.1 and 5.2.2 yields the overall Z-matrix at the external subports. The multiple subports at each external port are combined as follows. It is assumed that only the TEM mode is present in the uniform transmission line at the location of the external port. This is a valid assumption if the external ports are taken at a certain distance away from the planar circuit since any higher order modes present at the discontinuity at the junction of the transmission line and the planar circuit would decay along the uniform transmission line. For considering the external ports at a certain distance from the discontinuities, the intermediate transmission lines are modelled as rectangular planar segments (as shown in Fig. 5.1 for the power divider circuit).

Since only TEM mode is assumed to be present at an external port, the voltages at the subports of an external port are same. Thus, one can makes use of the parallel connection of subports which implies that the total current injected in a port gets divided into its various subports. This combination requires inversion of the overall Z-matrix to obtain admittance matrix. In general, if ports I and J are divided into subports,

$I = \{i_1, i_2, \ldots\}$ and $J = \{j_1, j_2, \ldots\}$ then the term Y_{IJ} of the overall admittance matrix is given as

$$Y_{IJ} = \sum_{k \in I} \sum_{\ell \in J} y_{k\ell} \qquad (5.23)$$

where $y_{k\ell}$ are the terms of the admittance matrix with multiple subports. The overall scattering matrix may be obtained from the admittance matrix $\underline{Y}$ using [23]

$$\underline{S} = [\sqrt{Z_o}] \, (\underline{Y}_o - \underline{Y})(\underline{Y}_o + \underline{Y})^{-1} \, [\sqrt{Y_o}] \qquad (5.24)$$

where $[\sqrt{Z_o}]$ and $[\sqrt{Y_o}]$ have been defined in (2.29) and $\underline{Y}_o$ is a diagonal matrix given by $Y_{o1}, Y_{o2}, \ldots, Y_{oN}$. $Y_{o1}, Y_{o2}, \ldots Y_{oN}$ represent the normalizing admittances at various external ports.

If the external ports are located such that the TEM mode approximation is not valid, the voltage and current density over the width of an external port can be expanded in terms of higher order stripline modes. The higher order stripline modes decay away from the junction along the transmission line and their characteristic impedances are reactive. Therefore, these higher order modes are considered as terminated by these reactive impedances at the port location itself [16]. However, for purposes of characterization of the planar circuit, it is convenient that the external ports be chosen at the locations where only the dominant mode exists, so that the procedure described earlier is applicable.

5.3 DISCUSSION

For analyzing the circuit shown in Fig. 5.1 by the inter-
connection of Z-matrices discussed in Sec. 5.2.1, two real
matrices of orders 52 and 18 and a complex matrix of order 3
need be inverted. It is seen that there is considerable
saving in computational effort as compared to segmentation
using S-matrices. In the method using subgrouped inter-
connections discussed in Sec. 5.2.2, inversions of two real
matrices of orders 26 and 18 and of a complex matrix of order 3
are required for analyzing the circuit shown in Fig. 5.1.

Orders of matrices that need to be inverted in different
methods are compared in Table 5.1. It may be noted that seg-
mentation using Z-matrices with suitably subgrouped inter-
connections involves significantly smaller amount of computa-
tions as compared to the other methods available earlier.
Moreover, this method can be used for any arbitrary topology
whereas, as pointed out in Sec. 5.1, the method using S-
matrices with subgrouping of connected ports can be used
only when the network does not contain any loop with odd
number of segments in it.

The proposed method using Z-matrices with suitably
subgrouped interconnections has been used for segmentation in
Chapters Six to Eight.

Table 5.1 Orders of matrices to be inverted in various
methods of segmentation for the circuit of
Fig. 5.1

Method	Segmentation using S-matrices	Segmentation using Z-matrices
Without subgrouping the connected ports	20×20 complex	52×52 real
	$3 \times (12 \times 12)$ complex	18×18 real
	14×14 complex	3×3 complex
	88×88 complex	
With suitable subgrouping of the connected ports	20×20 complex	26×26 real
	$3 \times (12 \times 12)$ complex	18×18 real
	14×14 complex	3×3 complex
	$2 \times (44 \times 44)$ complex	

Chapter Six

TRIANGULAR, RHOMBIC AND HEXAGONAL
RESONATORS

Two-dimensional planar resonators are used in
microwave integrated circuits. These resonators are
generally of a regular shape. In these resonators, the
electromagnetic energy is confined in the dielectric
medium between the ground plane(s) and the planar patch.
Resonant structures of simple geometrical shapes such as
rectangular, circular disk and annular ring have been
extensively used in oscillators, filters and circulators
[19] - [21]. Besides these, resonant structures of other
geometrical shapes also find applications in microwave
networks. Availability of different shapes provides
added flexibility in the design of circuits. Planar tri-
angular resonators have been studied by Helszajn and
James [9] and proposed for use in band-pass and band-stop
filters. It has been found that a stripline circulator
using an apex coupled equilateral triangular resonator
has a bandwidth three times more than that of a circular
disk circulator [10]. For many applications, the circular
resonator is not suitable due to anharmonius relationship
between its mode frequencies [30]. Hence, there is con-
siderable interest in the study of resonant structures of
different shapes [8]. Spectral domain analysis of

hexagonal resonators has been reported recently [22].

In this chapter, planar resonators of shapes such as an equilateral triangle, a 60° - rhombus and a regular hexagon are analyzed. Various modes of resonance for these resonators have been found from the theoretical analysis. Experimental verification of the resonance frequencies has been carried out and these have been found to be in close agreement with the theoretically predicted values.

6.1 METHOD OF ANALYSIS

The resonators discussed in this chapter are analyzed using the Green's function method. The periphery of the circuit is divided into various sections (each side of an equilateral triangle divided into twelve sections). The impedance matrix of a resonator (with various sections on the periphery treated as ports) is obtained. For rhombic and hexagonal resonators, segmentation method is employed to obtain the impedance matrix. The expressions for the Green's functions involve series summation from $-\infty$ to ∞ . For numerical evaluation of the impedance matrix, summation of terms from -50 to +50 is taken and is found to be adequate for convergence. Integrals of eigenfunctions (appearing in the Green's function expansion) over widths of various ports are needed for evaluation of impedance matrix. These integrals are listed in Appendix A.

Resonance in 2-d Circuits

The concept of resonance, applicable to 2-d circuits, can be evolved from lumped and transmission line resonators. In lumped resonators the reactance or the susceptance, between two terminals, is zero at the resonance frequency. If the resonator is considered lossless, the impedance is zero for series resonance and the admittance is zero for shunt resonance.

A section of uniform transmission line with both ends open, resonates when the length of the line is a multiple of half wavelength. The input admittance at any arbitrary point along the length of the line (Fig. 6.1) can be obtained. For the lowest order mode ($\lambda = 2\ell$), the input admittance is zero for all locations of the feed point except when feed point is located in the centre ($x = \frac{\ell}{2}$). At this point, the input impedance is zero. This centre point corresponds to the zero of the voltage variation along the length for the dominant mode. For higher order modes also, the input admittance for all locations of the feed point is zero except those corresponding to the zeros of the corresponding voltage variation. It is seen that as the frequency is increased the input admittances at all the points (except those corresponding to zeros of the voltage variation) cross zero (from negative to positive) at resonance. Correspondingly, the input impedances at all
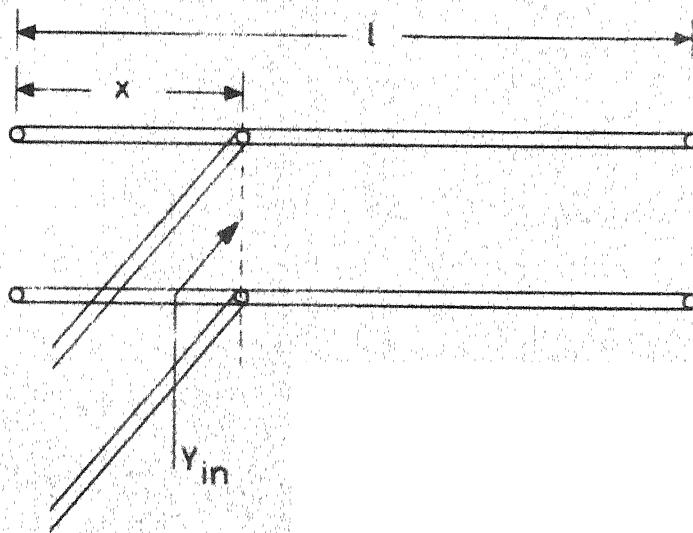
Fig. 6.1 A transmission line resonator

these points change sign from positive infinity to
negative infinity at resonance.

The concept of resonance described above for trans-
mission line resonators, can be applied to 2-d resonators
also. The input impedances, at various sections on the
periphery, go to infinity at resonance. Just below a
resonance frequency, the input reactances at various
sections have very high positive values and these change
sign to very high negative values at the resonance
frequency. This is valid for all sections except when
mid-point of a section corresponds to zero of the voltage
distribution.

The voltage distribution around the periphery at a
desired frequency of interest can be found from the
impedance matrix. This requires the location of the feed
point. If there are more than one feed points, relative
magnitudes and phases of the current fed have to be known.

Use of Geometrical Symmetry

For analyzing resonators of shapes such as a 60°-
rhombus and a regular hexagon, geometrical symmetry has
been utilized and the even and odd mode half-sections have
been analyzed separately. The even mode half-section has
a magnetic wall at the plane of symmetry and the odd mode
half-section has an electric wall at the plane of symmetry.
The impedance matrix is evaluated for the even mode case.

For the odd mode case, the impedance matrix is obtained by considering the ports along the electric wall to be grounded. A general method for finding Z-matrix for a circuit with part of the periphery grounded is described below.

Let the ports along the magnetic and electric walls be grouped as 1 and 2 respectively. The impedance matrix for ports all along the periphery can be partitioned as

$$
\begin{bmatrix} \underline{v}_1 \\ \underline{v}_2 \end{bmatrix} = \begin{bmatrix} \underline{Z}_{11} & \underline{Z}_{12} \\ \underline{Z}_{21} & \underline{Z}_{22} \end{bmatrix} \begin{bmatrix} \underline{i}_1 \\ \underline{i}_2 \end{bmatrix} . \tag{6.1}
$$

The subscript 2 denotes ports along the electric wall and hence

$$
\underline{v}_2 = \underline{0} . \tag{6.2}
$$

Substituting (6.2) into (6.1), the relation giving the impedance matrix for ports along the magnetic walls in the odd mode case is obtained as

$$
\underline{v}_1 = (\underline{Z}_{11} - \underline{Z}_{12} \, \underline{Z}_{22}^{-1} \, \underline{Z}_{21}) \, \underline{i}_1 . \tag{6.3}
$$

The modes of resonance for the three resonator shapes are described in subsequent sections.

6.2   TRIANGULAR RESONATORS

Planar resonators of equilateral triangle shape have been investigated by Helszajn and James [9]. They have studied the field patterns in triangular resonators with magnetic wall at the axis of symmetry, i.e. even mode field

patterns of an equilateral triangle. For the even mode, the voltage along the periphery of the triangle varies according to the eigenfunction $T_1(x,y)$ given by (3.5). The corresponding resonance frequencies are given by [9]

$$k_{m,n,\ell} = \frac{4\pi}{3a} \sqrt{m^2 + mn + n^2}$$

or

$$f = \frac{2c}{3a\sqrt{\varepsilon_r}} \sqrt{m^2 + mn + n^2} \qquad (6.4)$$

where c is the velocity of electromagnetic waves in free space and 'a' is the side of the triangle. In above, the indices ℓ, m and n satisfy (3.6). It follows from Chapter Three that $T_2(x,y)$ given by (3.15) is also an eigenfunction of the triangle. The voltage variations for these modes of resonance are given by (3.15). However, these modes are resonant at the same frequencies as the corresponding even modes i.e. given by (6.4). It may be noted that when m = n, $T_2(x,y)$ reduces to zero at all points. Thus, these odd modes exist only when m ≠ n.

Even modes of resonance are excited when the triangle is fed with currents that are symmetrical about the axis of symmetry as shown in Fig. 6.2(a). Odd modes of resonance can be excited by feeding currents which are anti-symmetrical about the axis of symmetry as shown in Fig. 6.2(b). These odd mode resonances have not been pointed out by earlier investigators. At the lowest frequency of resonance, the

(a)

(b)
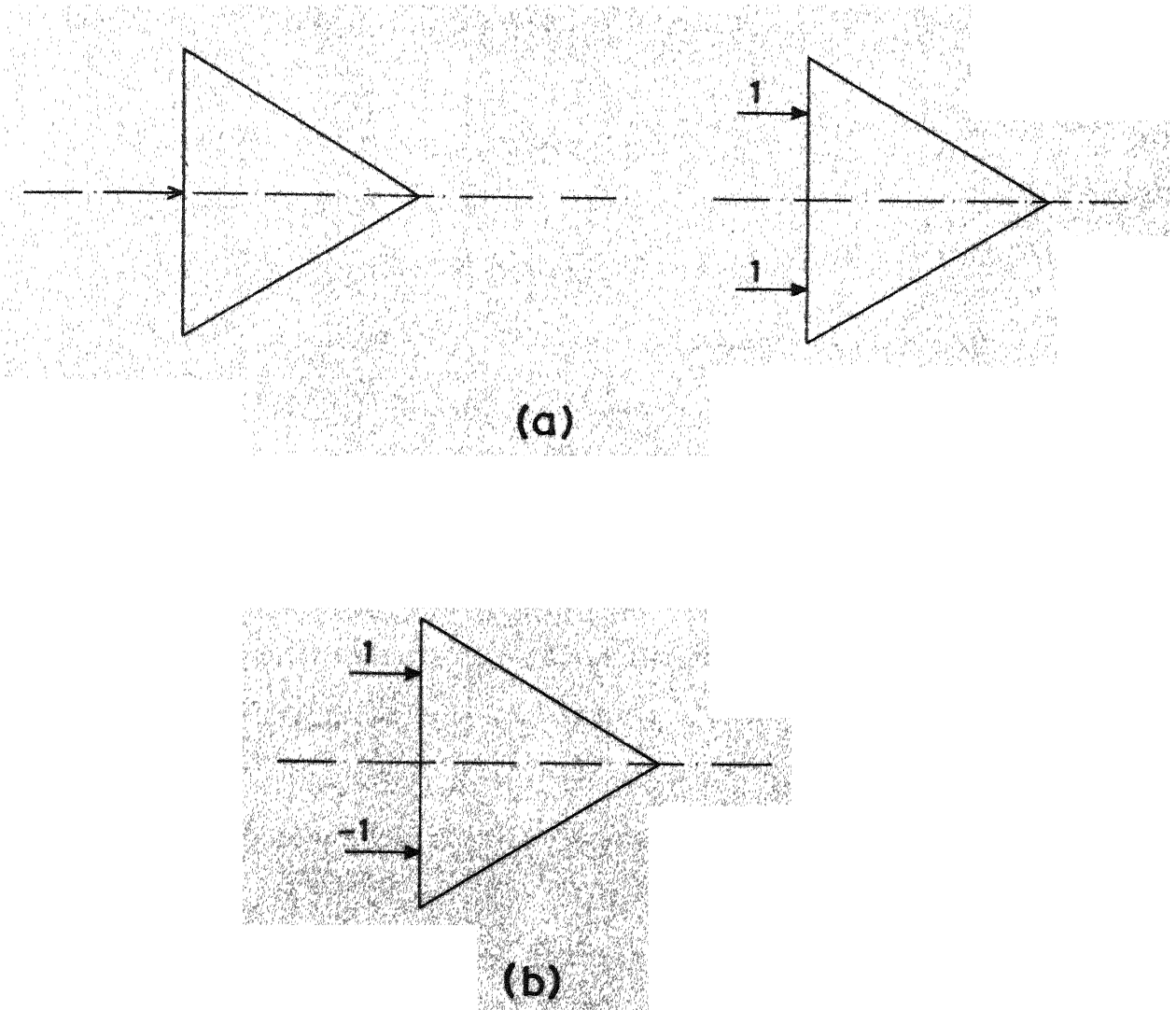
Fig. 6.2 (a)   Even mode and (b) odd mode
excitations for an equilateral triangle

voltage distributions around the periphery for the even
and the odd modes of resonance are shown in Fig. 6.3
(curves 'a' and 'b' respectively). An arbitrary linear
scale has been chosen for representing voltages in this
and in similar figures later.

For an arbitrary excitation both even and odd modes
of resonance are excited. The voltage distribution for a
mixed excitation ($\frac{1}{2}$ of the even mode excitation minus
$\frac{1}{2}$ of the odd mode excitation) is also shown in Fig. 6.3
(curve 'c'). It is seen that, for this case, the voltage
variation can be obtained as $\frac{1}{2}$ of even mode variation
minus $\frac{1}{2}$ of odd mode variation.

An equilateral triangular resonator has been fabri-
cated in stripline configuration on polystyrene substrate
(ε_r = 2.47, height d = 1/16", side of triangle, A=6.055 cm).
Photograph shown in Fig. 6.4 includes the lower plate of
substrate for this resonator. The frequencies of reso-
nance have been measured experimentally. The resonance
frequencies are detected using a network analyzer set-up
as shown in Fig. 6.5. At the resonance frequency high
fields are excited and because of losses in the resonator,
a dip is observed in the reflected signal. To obtain
theoretical values of resonance frequencies, the magnetic
wall is considered to be shifted outwards from the physical
periphery by an amount δ given by (2.2). The effective
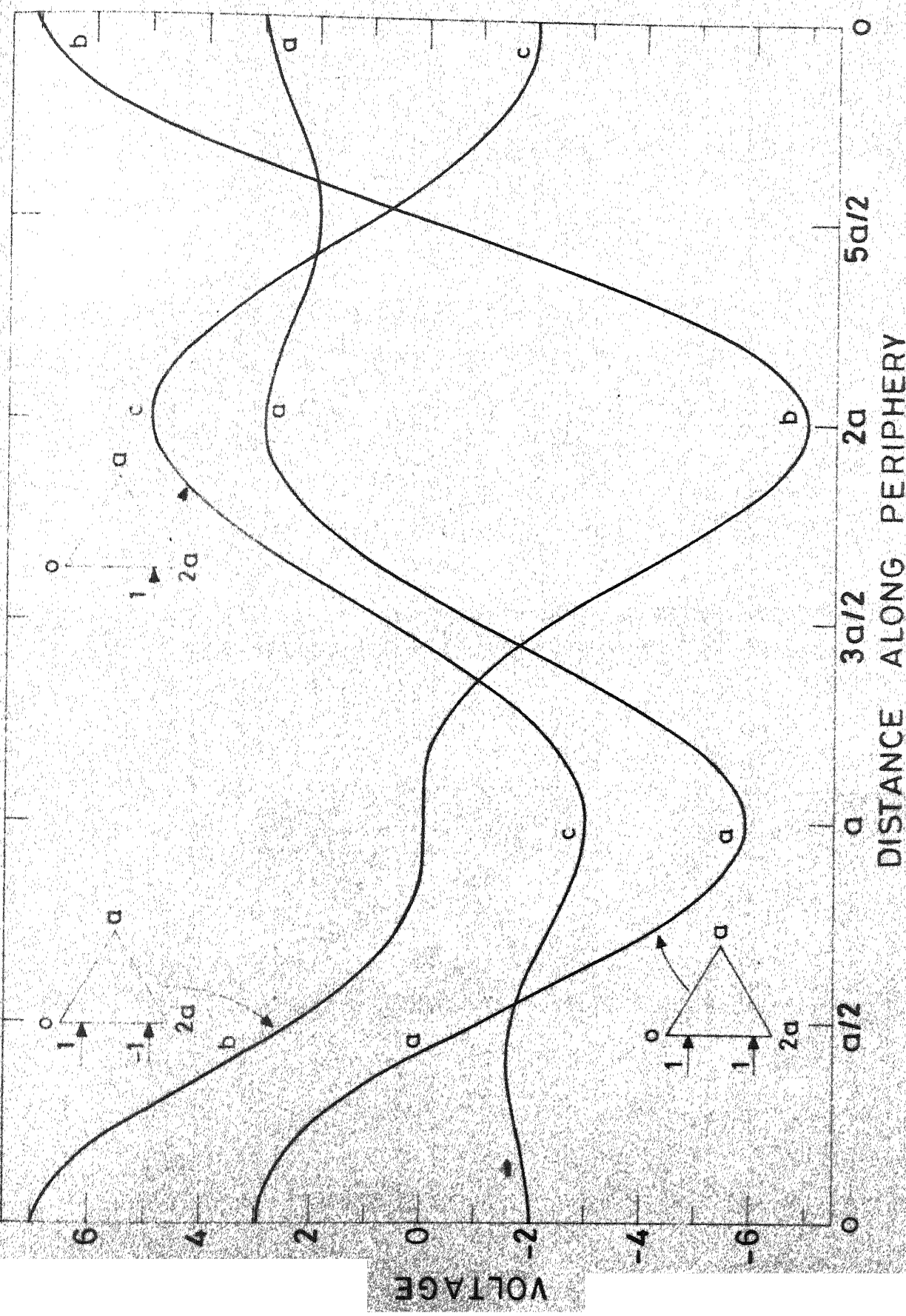side of the triangle 'a' is given by

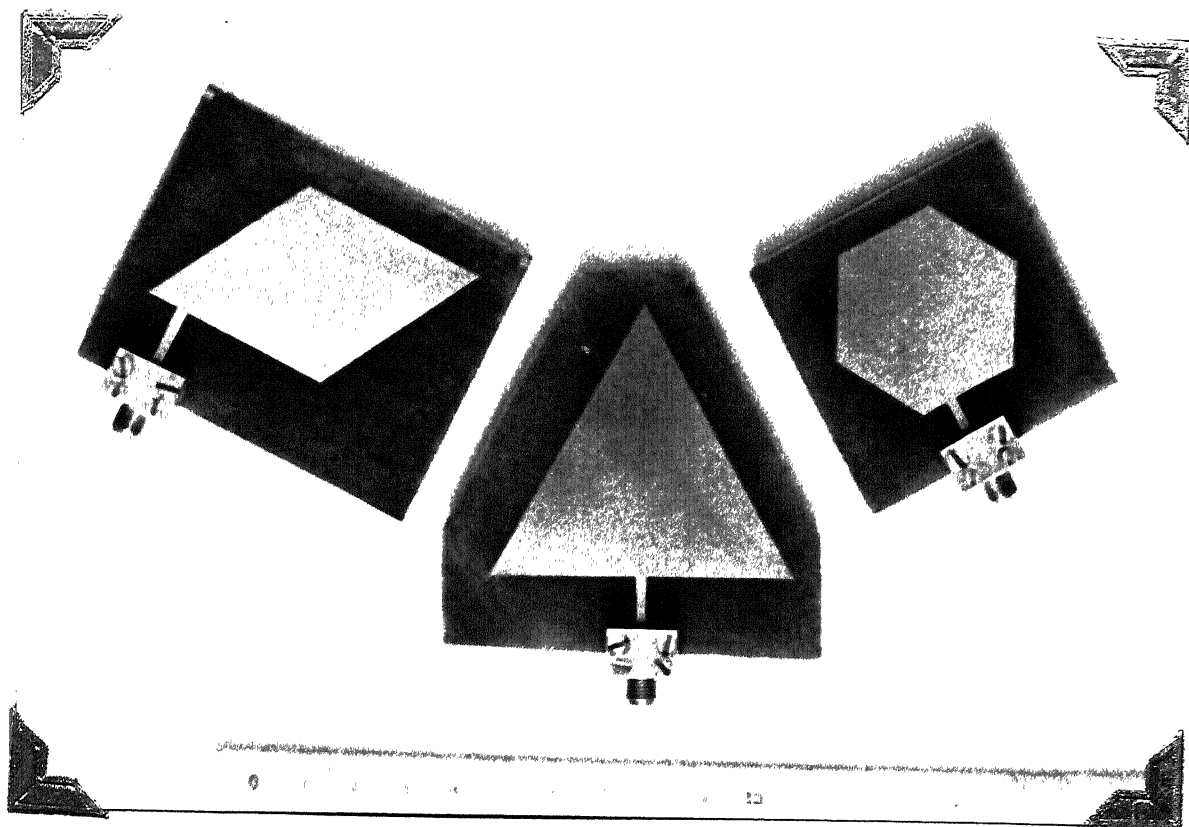Fig. 6·3 Voltage variations for equilateral triangular resonator.

Fig. 6.4   Triangular, rhombic and hexagonal resonators
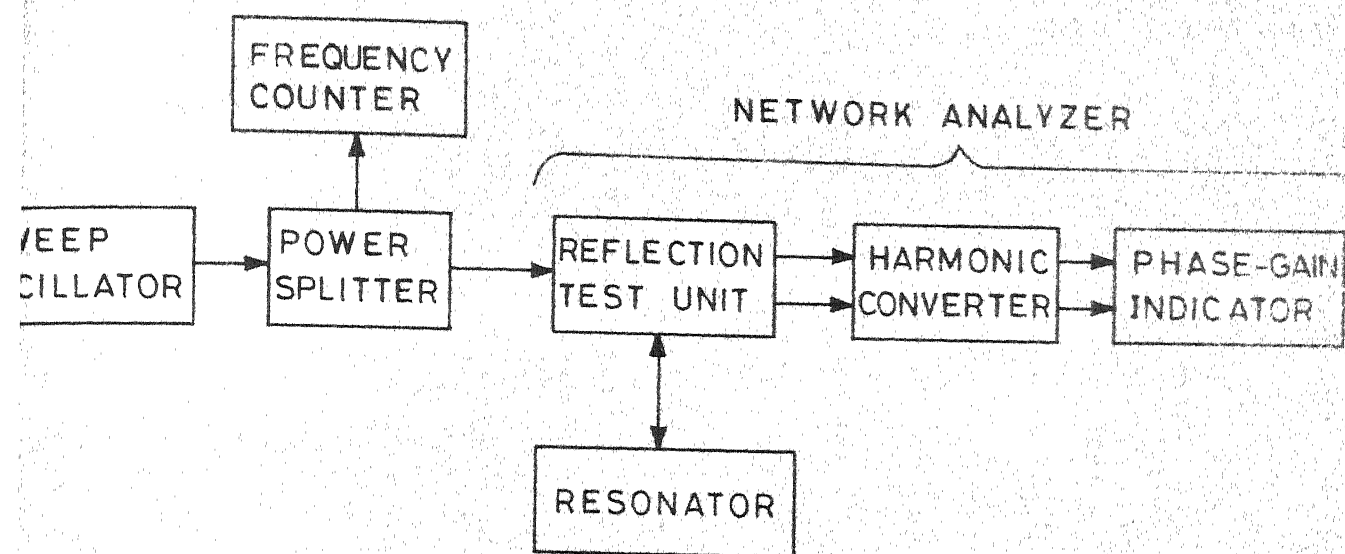with the top dielectrics and ground planes
removed .

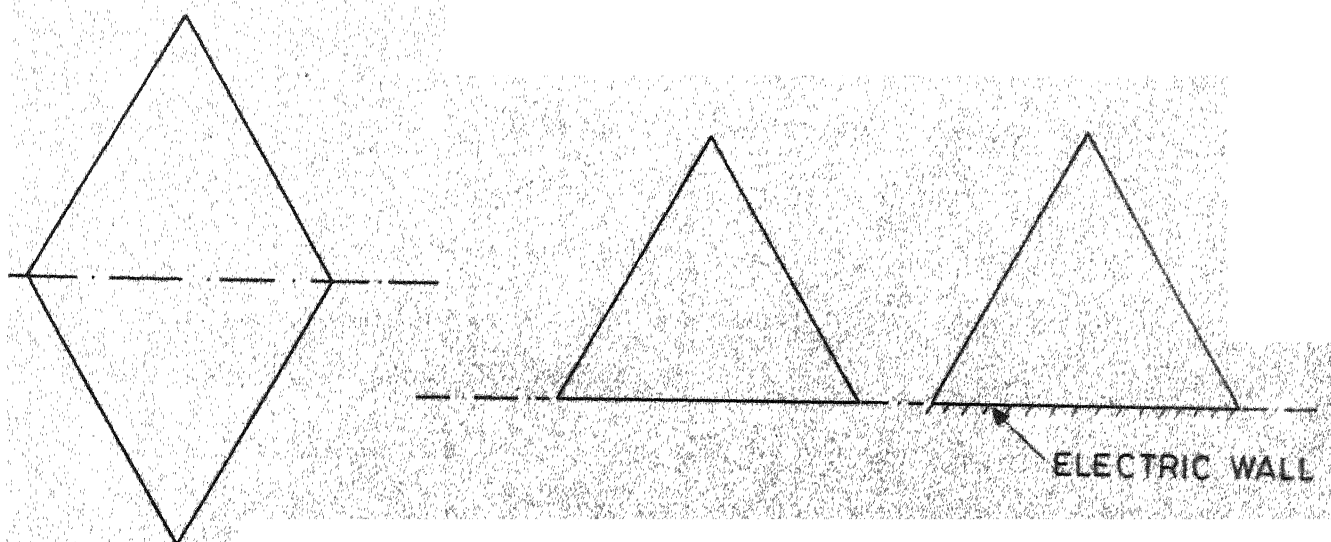Fig.6.5   Network analyzer set-up for measuring resonance frequency.

Fig. 6.6   A 60°-rhombus and its even and odd mode half-sections.

$$a = A + 2\sqrt{3}\,\delta \qquad\qquad (6.5)$$

where A is the actual side of the triangle. Theoretical and experimental values of resonance frequencies have been compared in Table 6.1.

6.3 RHOMBIC RESONATORS

A 60° - rhombus can be analyzed by segmenting it into two equilateral triangles. However, it has been analyzed by considering its even and odd mode half-sections. The even and odd mode analysis is preferred since the even mode half-section corresponds to an equilateral triangle whose analysis is already available. Further, this approach provides a better insight into the nature of modes.

The even mode half-section of a 60° rhombus is an equilateral triangle with all sides as magnetic walls whereas the odd mode half-section is an equilateral triangle with one side as electric wall and other two sides as magnetic walls. These even and odd mode half-sections are shown in Fig. 6.6. The rhombus will have all the possible modes of resonances of an equilateral triangle and also those of its odd mode half-section. The impedance matrix of the odd mode half-section is obtained by using the procedure outlined in Sec. 6.1.

Table 6.1 Comparison of theoretically calculated and
experimentally measured values of resonance
frequencies for an equilateral triangular
resonator.

Effective side a = 6.298 cm, ε_r = 2.47, d = 1/16"

Mode m,n	λ *	Resonance Frequency	
		Theoretical	Experimental
1,0	1.5a	2.021 GHz	2.039 GHz
1,1	$a\sqrt{3}/2$	3.500 GHz	3.524 GHz
2,0	0.75a	4.041 GHz	4.038 GHz
2,1	$3a/2\sqrt{5}$	5.346 GHz	5.356 GHz
3,0	0.5a	6.062 GHz	6.041 GHz
2,2	$a\sqrt{3}/4$	7.000 GHz	7.084 GHz
3,1	$3a/2\sqrt{3}$	7.285 GHz	7.280 GHz
4,0	3a/8	8.082 GHz	8.047 GHz

* $\lambda = \lambda_o/\sqrt{\varepsilon_r} = c/(f\sqrt{\varepsilon_r})$

The modes of resonance corresponding to the even mode are same as those of the equilateral triangle. The resonance frequencies corresponding to the odd mode are obtained separately. The lowest resonance frequency corresponds to the odd mode. The voltage distribution along the periphery for the lowest order mode is shown in Fig. 6.7. The next higher resonance frequency corresponds to lowest resonance frequency of the equilateral triangle (i.e. even mode half-section). Since the equilateral triangle has two modes (even and odd) at many resonance frequencies, the rhombus also has two modes at these frequencies. These modes are designated as even-even and even-odd, where the first word 'even' refers to the even mode of the rhombus and the second word 'even' or 'odd' refers to the corresponding mode of the triangle. The even-odd mode is excited by feeding currents which are anti-symmetric about the longer diagonal (xx) and symmetric about the smaller diagonal of the rhombus as shown in Fig. 6.8(a). The even-even mode can be excited as shown in Fig. 6.8(b). The voltage variations around the periphery for the even-even and even-odd modes are shown in Fig. 6.9 (curves 'a' and 'b' respectively).

The lowest order mode (i.e. odd mode) of the rhombus (shown in Fig. 6.7) has quarter cycle variation along each side. Hence, this may be called $(\frac{1}{2}, \frac{1}{2})$ odd mode. The next
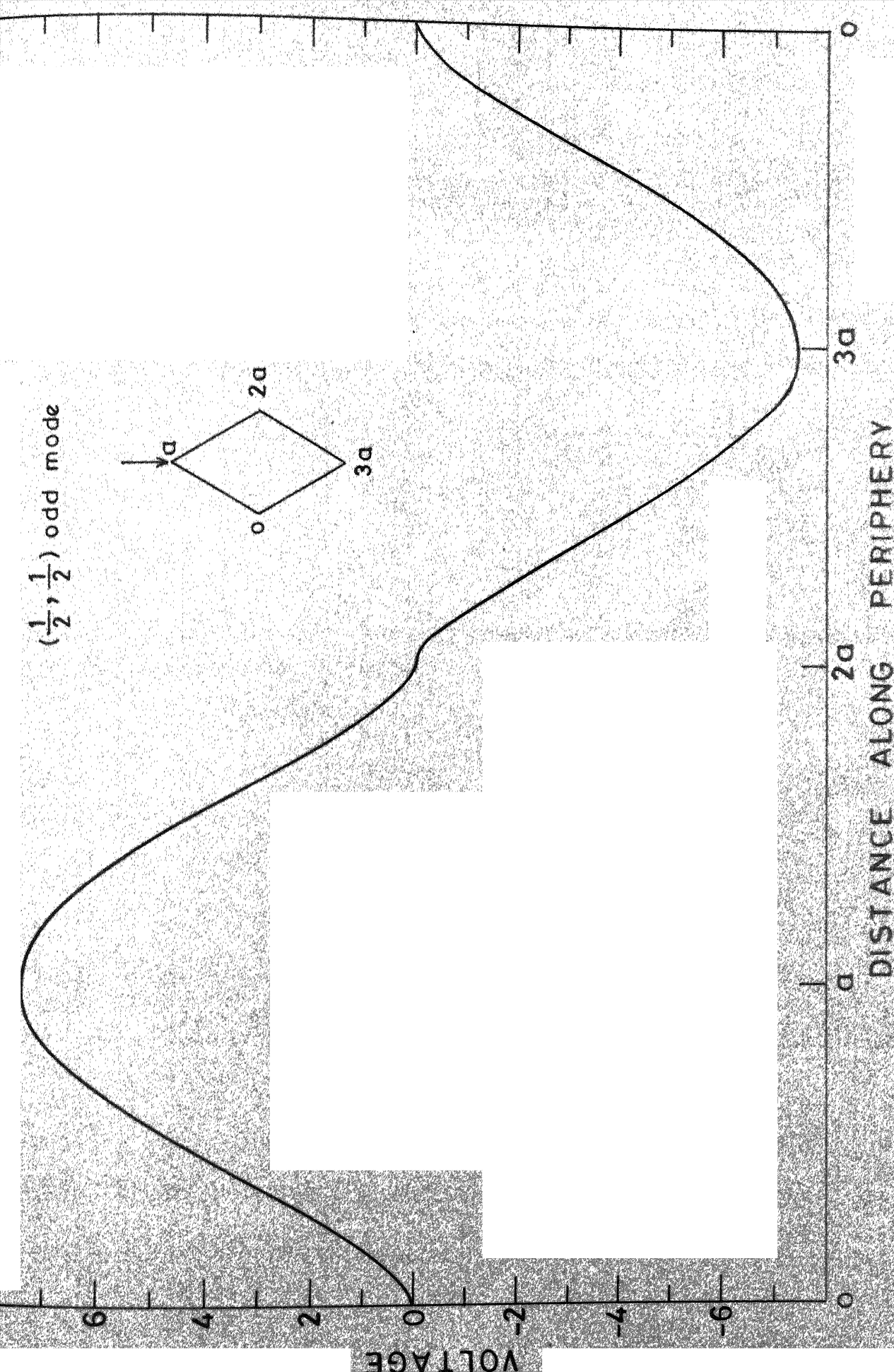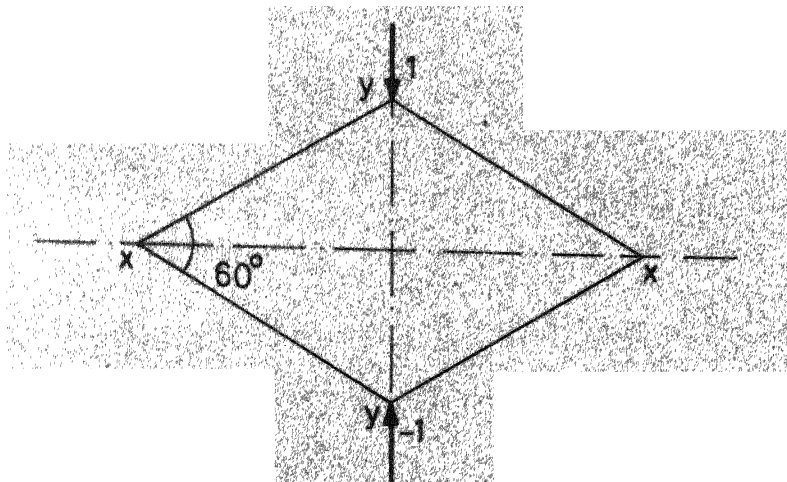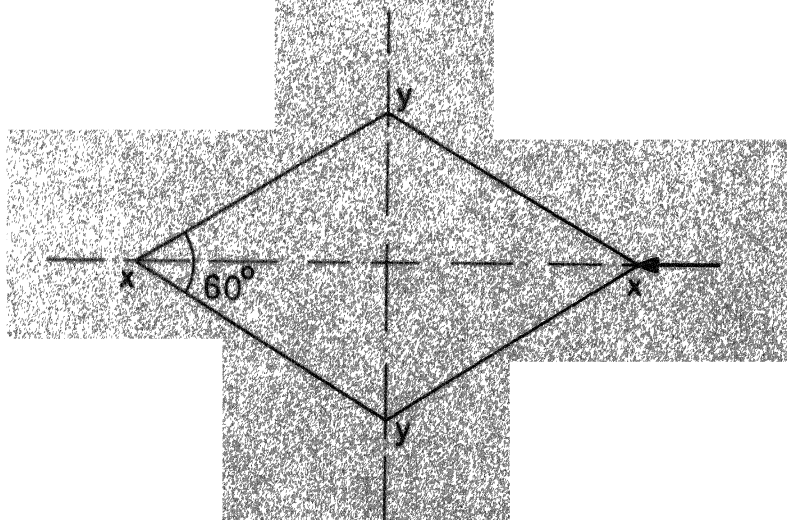
Fig. 6·7 Voltage variation for dominant mode of rhombus

$(\frac{1}{2}, \frac{1}{2})$ odd mode

VOLTAGE

DISTANCE ALONG PERIPHERY

Fig. 6.8 Excitation of (a) an even-odd
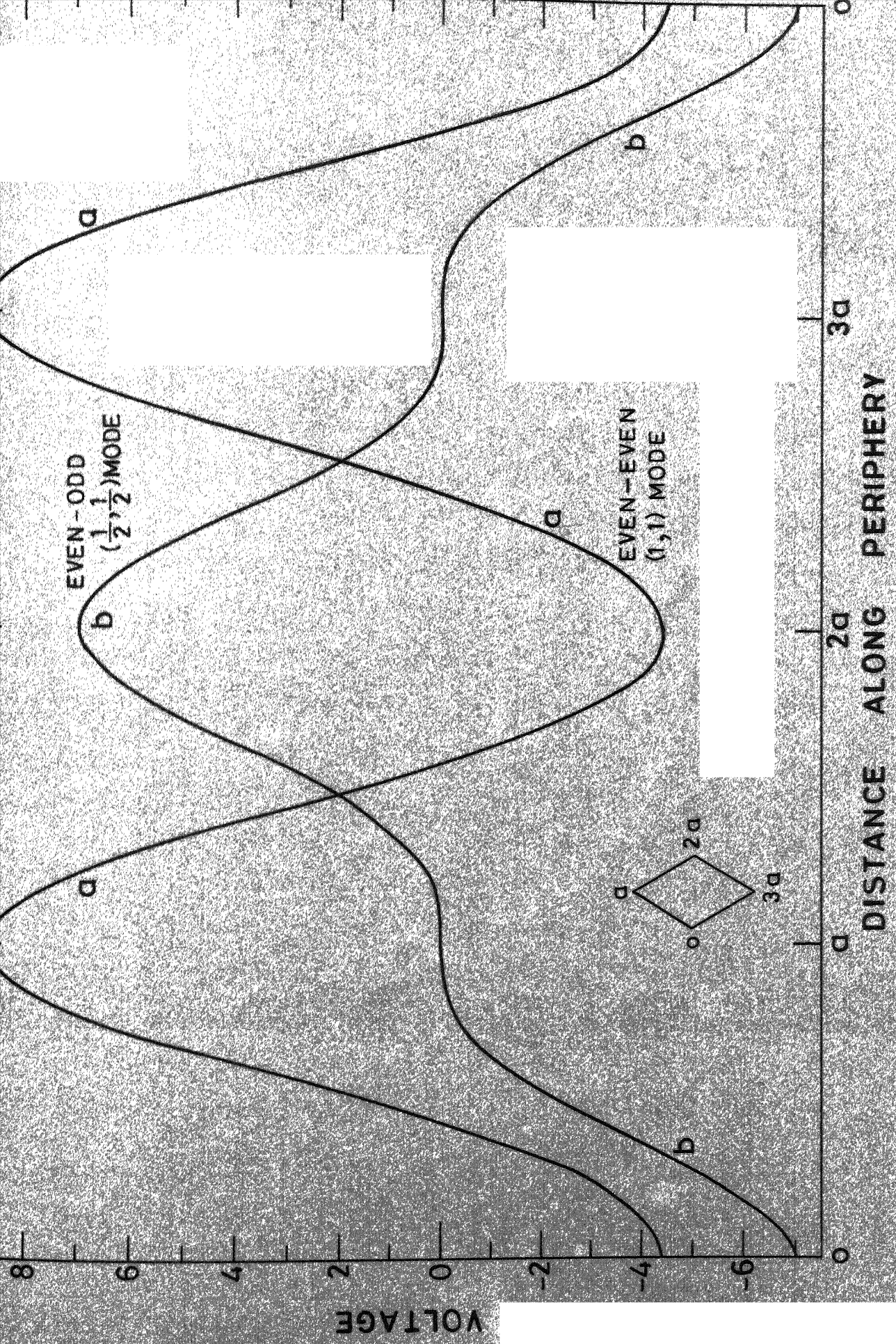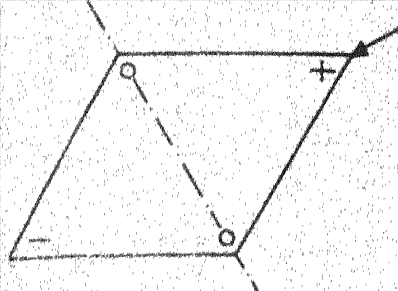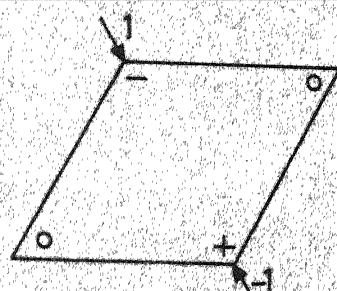and (b) an even-even mode
of a rhombus

Fig. 6.9 Voltage variation for lowest order even modes of rhombus.

higher even-even mode shown in Fig. 6.9 (curve 'a') has
half cycle variation along each side and can be termed as
(1,1) even-even mode. The even-odd mode resonant at the
same frequency has quarter cycle variation along each side
(Fig. 6.9, curve 'b') and is termed as $(\frac{1}{2}, \frac{1}{2})$ even-odd
mode. Other higher order modes are also named in the
same fashion. The positions of zeros around the periphery
are shown in Fig. 6.10 for various modes. The feed point
locations have been indicated by arrows. Some higher order
modes have same number of cycles along each side as another
lower frequency mode of the same type. For instance, the
even-even modes at $\lambda = 1.5a$ and $\lambda = 0.75a$ have half
cycle variation along each side. Though both of these may
termed as (1,1) even-even modes, it is seen that the mode
at the higher frequency has a non-monotonic voltage varia-
tion between the positive and the negative peaks along the
periphery. The variation of voltage along the periphery for
the even-even mode at $\lambda = 0.75a$ is shown in Fig. 6.11.
To distinguish it from the lower order (1,1) even-even mode,
this mode is termed as $(1,1)^*$ even-even mode. Similar beha-
viour has been observed for other higher order modes also,
where the number of cycles along a side of the rhombus for
a higher frequency mode is same as that for a similar mode
at lower frequency because of non-monotonic variation of
voltage between positive and negative peaks. In such cases,
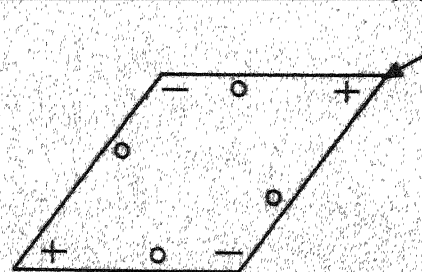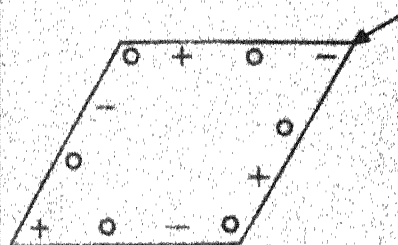the high frequency mode is termed with a superscript *.

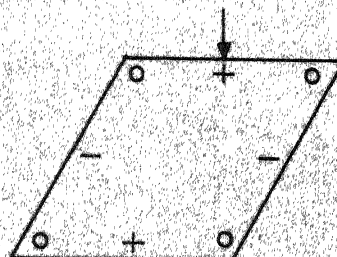$\left(\frac{1}{2},\frac{1}{2}\right)$ odd mode
$\lambda = 2.34a$

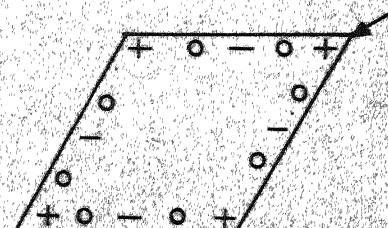$\left(\frac{1}{2},\frac{1}{2}\right)$ even-odd mode
$\lambda = 1.5a$

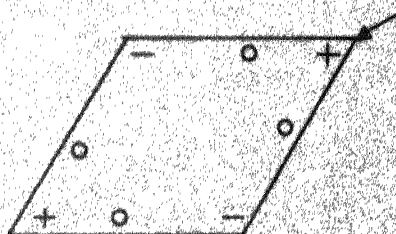$(1,1)$ even-even mode
$\lambda = 1.5a$

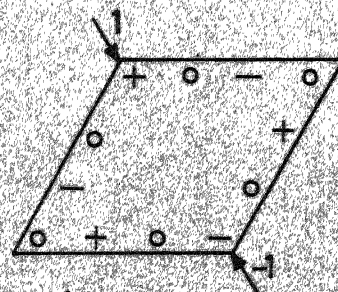$\left(1\frac{1}{2},1\frac{1}{2}\right)$ odd mode
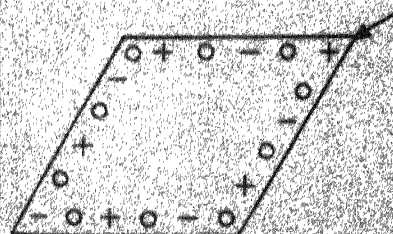$\lambda = 1.023a$

$(1,1)$ odd mode
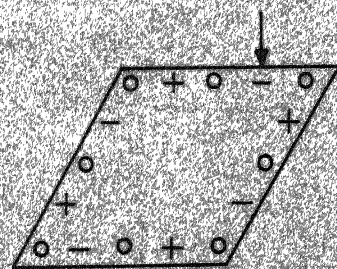$\lambda = 0.908a$

$(2,2)$ even-even mode
$\lambda = 0.866a$

$(1,1)^*$ even-even mode
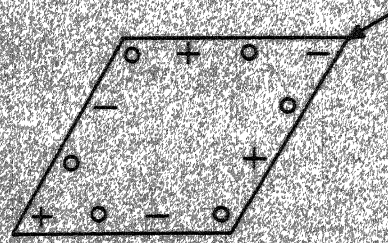$\lambda = 0.75a$

$\left(1\frac{1}{2},1\frac{1}{2}\right)$ even-odd mode
$\lambda = 0.75a$

$\left(2\frac{1}{2},2\frac{1}{2}\right)$ odd mode
$\lambda = 0.66a$

$(2,2)$ odd mode
$\lambda = 0.596a$

$\left(1\frac{1}{2},1\frac{1}{2}\right)^*$ odd mode
$\lambda = 0.57a$

Contd.
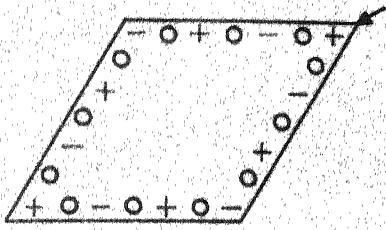
(3,3) even–even mode
$\lambda = 0.567a$

$(2\frac{1}{2}, 2\frac{1}{2})$ even–odd mode
$\lambda = 0.567a$

(2,2)* even–even mode
$\lambda = 0.5a$

(2,2) even–odd mode
$\lambda = 0.5a$
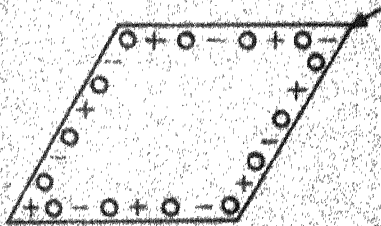
$(3\frac{1}{2}, 3\frac{1}{2})$ odd mode
$\lambda = 0.482a$

(3,3) odd mode
$\lambda = 0.455a$
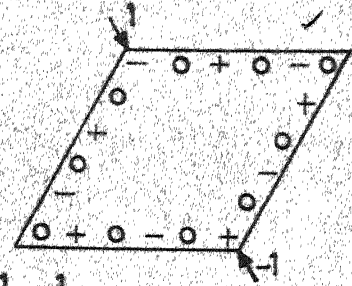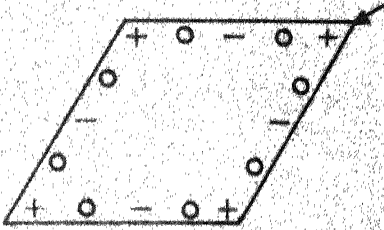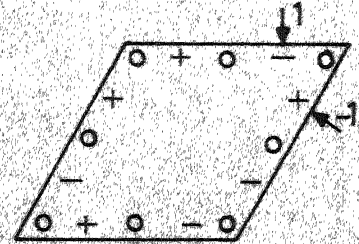
(4,4) even–even mode
$\lambda = 0.433a$

$(2\frac{1}{2}, 2\frac{1}{2})$* odd mode
$\lambda = 0.423a$
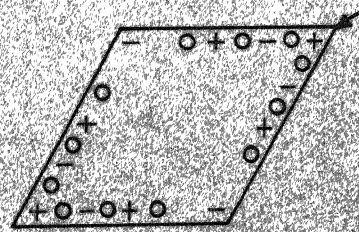
(3,3)* even–even mode
$\lambda = 0.416a$

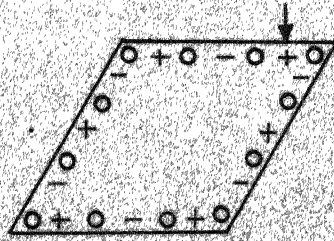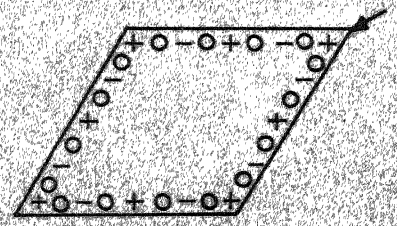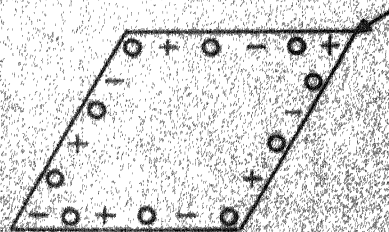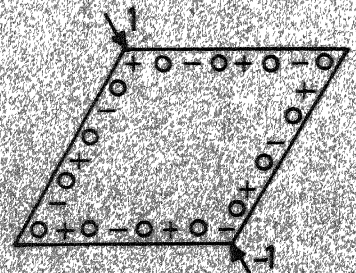$(3\frac{1}{2}, 3\frac{1}{2})$ even–odd mode
$\lambda = 0.416a$

Fig. 6.10 Various modes of a rhombus.
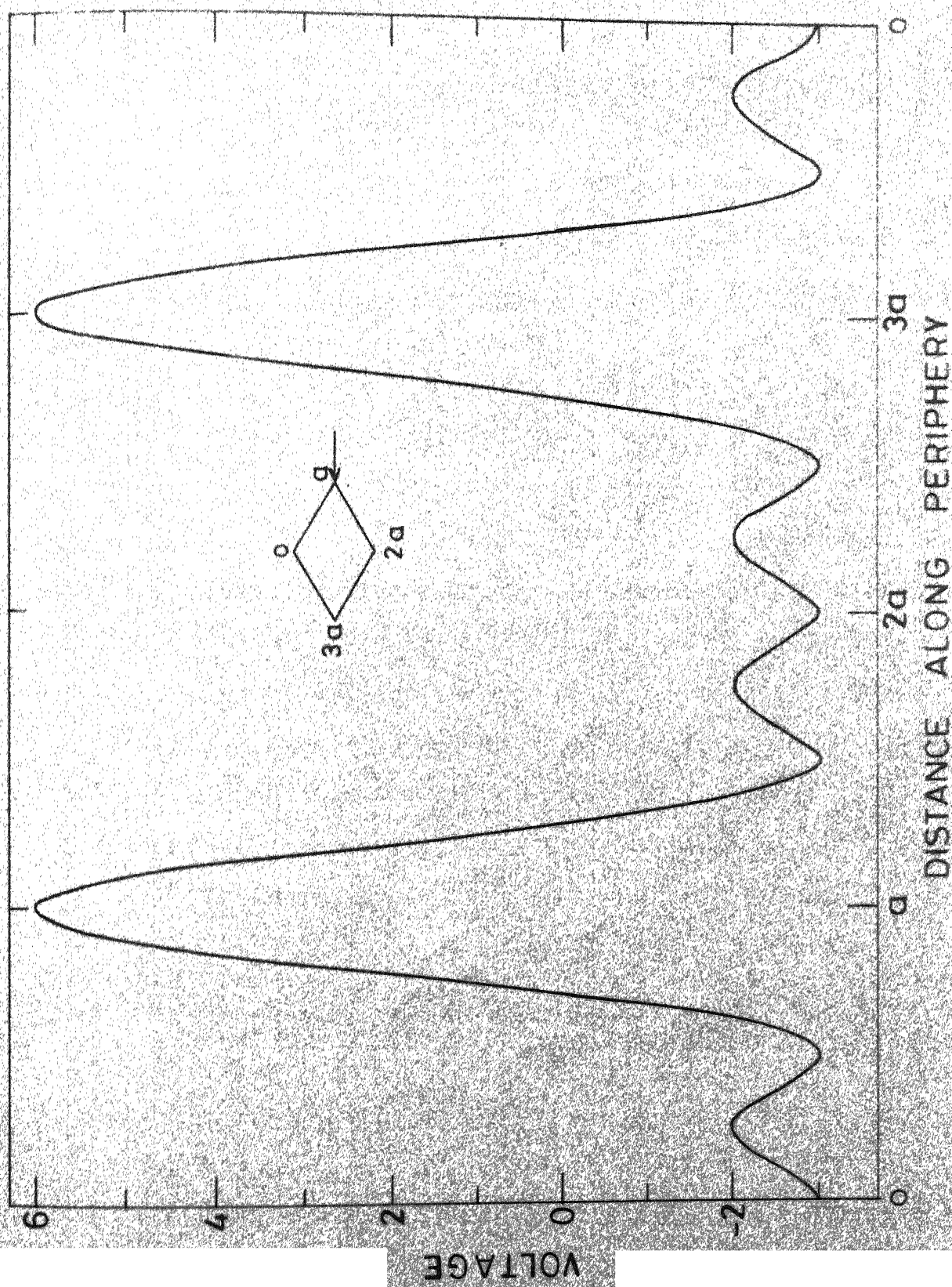
Fig. 6.11 Voltage variation for (1,1)* even-even mode

It is worthwhile here to compare the modes of
resonances of a rhombus with those of a square resonator
with side a. At the lowest resonant frequency ($\lambda = 2a$),
both (1,0) and (0,1) modes are resonant in a square
resonator. In these modes, the voltage has half cycle
variation along two parallel sides and is constant along
the other set of two parallel sides as shown in Fig. 6.12(a).
The (1,0) and (0,1) modes can be combined to give the
($\frac{1}{2}$,$\frac{1}{2}$) modes shown in Fig. 6.12(b). Conversely, each of the
modes shown in Fig. 6.12(a) can be thought of as obtained
from the two ($\frac{1}{2}$,$\frac{1}{2}$) modes in Fig. 6.12(b). In a rhombus,
the two ($\frac{1}{2}$,$\frac{1}{2}$) modes, i.e. ($\frac{1}{2}$,$\frac{1}{2}$) odd mode and ($\frac{1}{2}$,$\frac{1}{2}$) even-
odd mode do not resonate at the same frequency and hence
these cannot be combined to give a (0,1) or a (1,0) mode.
In a square, the (1,0) and (0,1) modes exist because the
two ($\frac{1}{2}$,$\frac{1}{2}$) modes are resonant at the same frequency (λ=2a). In a
rhombus, (1,0) and (0,1) modes do not exist because the two ($\frac{1}{2}$,$\frac{1}{2}$)
modes resonate at frequencies given by $\lambda = 2.34a$ and
$\lambda = 1.5a$.

A 60°-rhombic resonator has been fabricated in strip-
line configuration on polystyrene substrate ($\varepsilon_r = 2.47$,
height d = 1/16", side of rhombus, A = 3.755 cm.). The
photograph shown in Fig. 6.4 includes the lower plate of
substrate for the rhombic resonator also. The frequencies
of resonance have been measured experimentally. The effective

(0,1) mode
λ = 2a

(1,0) mode
λ = 2a

(a)
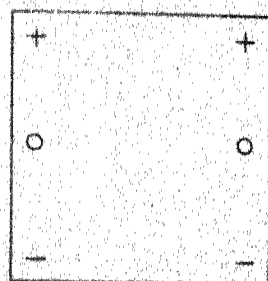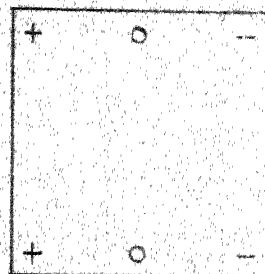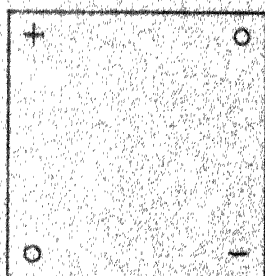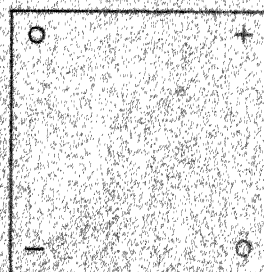
$(\frac{1}{2}, \frac{1}{2})$ mode
λ = 2a

$(\frac{1}{2}, \frac{1}{2})$ mode
λ = 2a

(b)

Fig. 6.12   Modes of a square resonator

side of the rhombus is obtained by considering the
magnetic wall to be shifted outwards from the physical
periphery by an amount δ. Effective side 'a' is thus given
by

$$a = A + \frac{4}{\sqrt{3}} \delta \qquad (6.6)$$

where A is the actual side of the rhombus. Theoretical
and experimental values of the resonance frequencies for
the rhombic resonator have been compared in Table 6.2.

6.4 HEXAGONAL RESONATORS

A regular hexagonal shape has been used as a microstrip
resonator and as a circulator element [31]. Hsu et al.[32]
have obtained the lowest order resonant frequency of a
microstrip resonator in terms of effective hexagon side 'a'
as

$$f = 2.011 \frac{c}{2\pi a \sqrt{\epsilon_r}} . \qquad (6.7)$$

Sharma and Hoefer [22] have recently reported analysis of
regular hexagonal microstrip resonators. They have used
the quasi-static formulation in the spectral domain to
determine the capacitance and effective hexagon side. The
lowest order resonant frequency has then been determined
using (6.7).

In this section, the even and odd mode analysis for a
regular hexagon is presented. The even mode half-section is

Table 6.2 Comparison of theoretically calculated and experimentally measured resonance frequencies for a 60°-rhombic resonator

Effective side, $a = 3.917$ cm, $\varepsilon_r = 2.47$, $d = 1/16''$

Mode	λ	Resonance frequency	
		Theoretical	Experimental
$(\frac{1}{2},\frac{1}{2})$ odd	2.34a	2.081 GHz	2.129 GHz
$(\frac{1}{2},\frac{1}{2})$ even-odd $\}$ $(1,1)$ even-even	1.5a	3.249 GHz	3.235 GHz
$(1\frac{1}{2},1\frac{1}{2})$ odd	1.023a	4.764 GHz	4.765 GHz
$(1,1)$ odd	0.908a	5.369 GHz	5.327 GHz
$(2,2)$ even-even	0.866a	5.627 GHz	5.639 GHz
$(1,1)^*$ even-even $\}$ $(1\frac{1}{2},1\frac{1}{2})$ even-odd	0.75a	6.498 GHz	6.465 GHz
$(2\frac{1}{2},2\frac{1}{2})$ odd	0.66a	7.383 GHz	7.413 GHz
$(2,2)$ odd	0.596a	8.172 GHz	8.159 GHz
$(1\frac{1}{2},1\frac{1}{2})^*$ odd	0.57a	8.551 GHz $\}$	8.549 GHz
$(3,3)$ even-even $\}$ $(2\frac{1}{2},2\frac{1}{2})$ even-odd	0.567a	8.596 GHz	
$(2,2)^*$ even-even $\}$ $(2,2)$ even-odd	0.5a	9.747 GHz	9.737 GHz
$(3\frac{1}{2},3\frac{1}{2})$ odd	0.482a	10.109 GHz	10.129 GHz
$(3,3)$ odd	0.455a	10.703 GHz	10.704 GHz
$(4,4)$ even-even	0.433a	11.254 GHz	11.194 GHz
$(2\frac{1}{2},2\frac{1}{2})^*$ odd	0.423a	11.533 GHz	11.526 GHz
$(3,3)^*$ even-even $\}$ $(3\frac{1}{2},3\frac{1}{2})$ even-odd	0.416a	11.714 GHz	11.699 GHz

a trapezoid which is analyzed by segmenting it in three
equilateral triangles. The odd mode half-section is also
a trapezoid with the largest side being an electric wall
as shown in Fig. 6.13. The odd mode half-section is
analyzed by finding the impedance matrix for all ports of
the trapezoid and imposing the electric wall boundary
condition for the ports along the largest side using the
procedure outlined in Sec. 6.1. Alternatively, it may be
analyzed by segmentation method with segment 'a'(Fig. 6.13)
being an equilateral triangle and 'b' and 'c' equilateral
triangles with one side as an electric wall.

At the lowest resonance frequency, both the even and
the odd modes are resonant. The variations of voltage
around the periphery for the lowest order modes are shown
in Fig. 6.14. For many higher order modes also, the odd
mode resonates at the same frequency as the even mode. The
positions of zeros around the periphery for various modes
of resonance studied are shown in Fig. 6.15. For even
mode resonances, variations along the axis of symmetry are
also known. These correspond to radial variations (at the
axis) and are shown in Fig. 6.15 for even modes. The lowest
order modes of a hexagon are resonant at $\lambda = 3.11a$. The
results of Hsu et al. [32] given by (6.7) yield a corres-
ponding value of $3.124a$ which is quite close to the value
obtained by the present method.
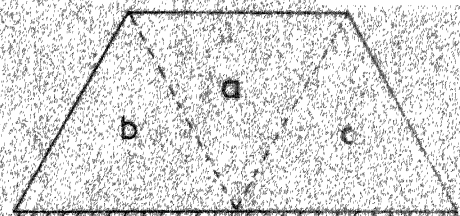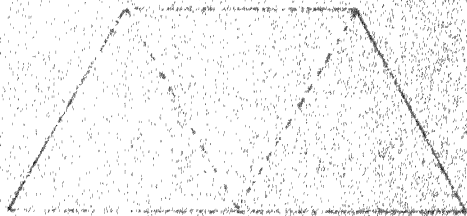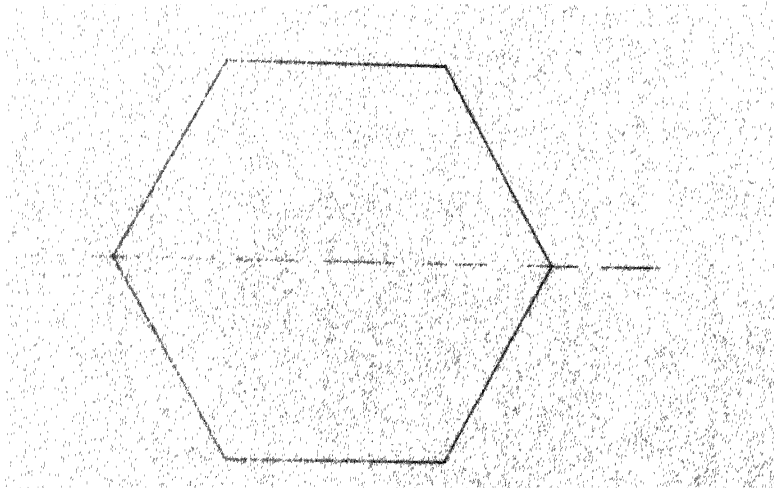
Fig. 6.13   A hexagon and its even and odd mode
             half-sections.
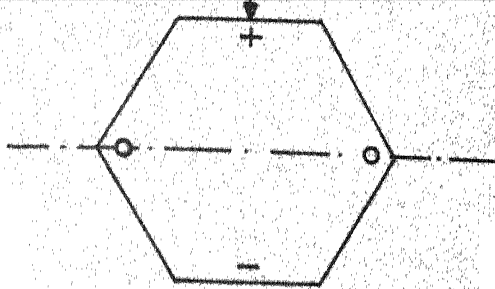
(1,1) odd mode
λ = 3.11a
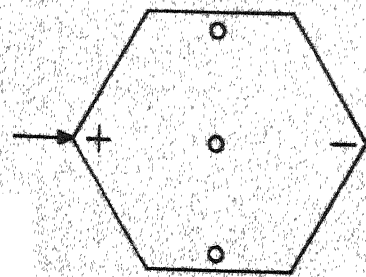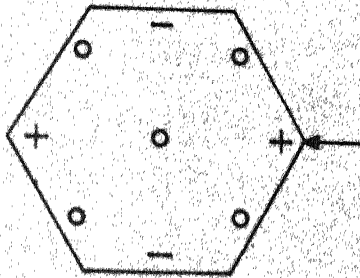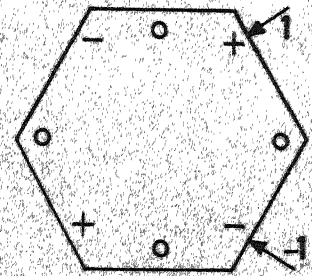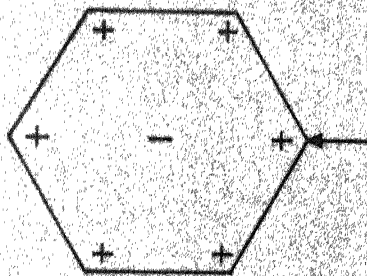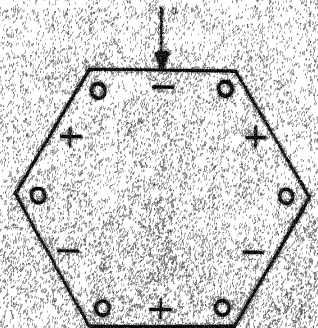
(1,1) even mode
λ = 3.11a

(2,1) even mode
λ =1.90a

(2,1) odd mode
λ =1.90a

(0,1) even mode
λ = 1.5 a

(3,1) odd mode
λ = 1.25a
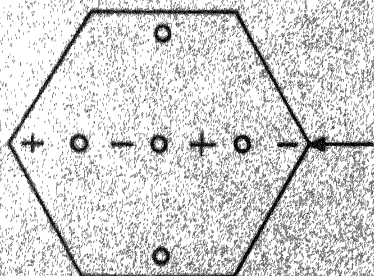
(1,2) even mode
λ = 1.09a
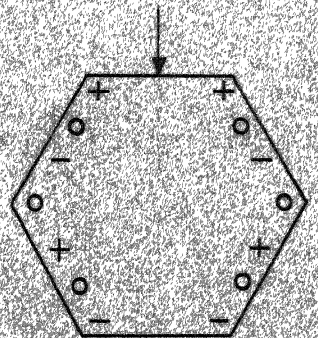
(3,1)* odd mode
λ = 1.09a
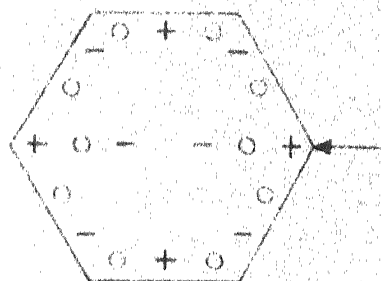
(4,1) even mode
λ = 1.08a
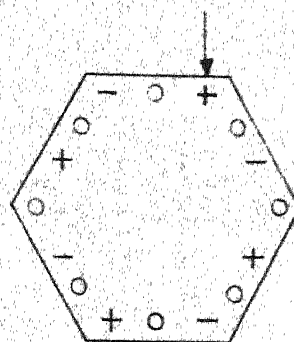
(4,1) odd mode
λ = 1.08a
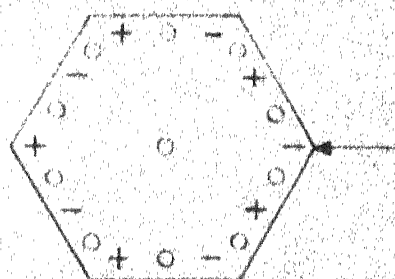
(5,1) even mode
λ = 0.887a
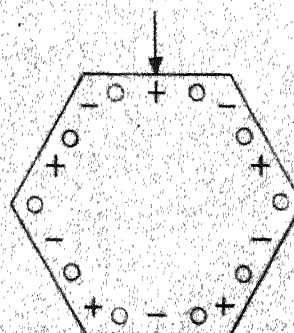
(5,1) odd mode
λ = 0.887a
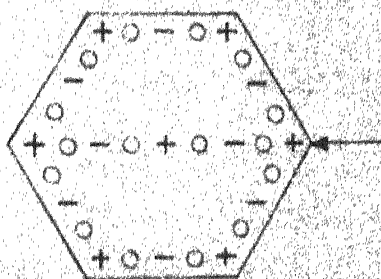
(6,2) even mode
λ = 0.866a
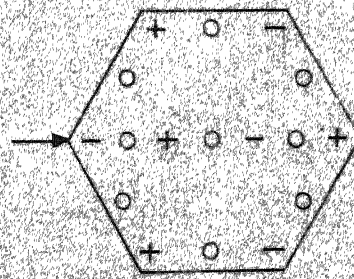
(3,2) even mode
λ = 0.75a

Fig. 6.15   Various modes of a hexagon

For circular disk resonators, the even and the odd modes resonate at the same frequency. In the case of hexagonal resonator, there are certain frequencies where either only the even mode or only the odd mode is resonant. The nomenclature of modes of the hexagonal resonator is based on the modes of a circular resonator. For a circular disk resonator of radius 'a', the modes of resonance are given by

$$\lambda = 2\pi/k_{nm} \qquad (6.8)$$

where k_{nm} satisfy

$$J_n'(k_{nm}\, a) = 0 . \qquad (6.9)$$

In these modes, m denotes the mth root of (6.9) and determines the radial variation of fields. There is n-cycle variation around the periphery.

The lowest order modes of hexagonal resonator have one cycle variation around the periphery. For the even mode, there is a zero in the center of the hexagon, hence the lowest order modes have been called (1,1) modes. The higher order modes have also been named in the same manner. As in the case of rhombic resonator, some higher frequency modes have similar variations as a low frequency mode. In such cases, the high frequency mode is termed with a superscript *.

It is significant here to compare the modes of resonance of a hexagon with those of a circular disk resonator of

radius 'a'. The lowest order (1,1) mode of a circular resonator corresponds to $\lambda = 3.413a$ whereas (1,1) mode of a hexagon resonates at $\lambda = 3.11a$. For the (0,1) mode of a circle, the odd mode does not exist. In the present case also, only the (0,1) even mode has been observed. The (4,1) mode of a hexagon differs from the corresponding mode of a circle so that the voltage in the center of the hexagon is nonzero. Resonance frequencies of hexagonal resonator are compared with those of a circular disk resonator in Table 6.3.

A regular hexagonal resonator has been fabricated in stripline configuration on polystyrene substrate ($\varepsilon_r = 2.47$, height d = 1/16", side of hexagon, A = 2.017 cm.). The photograph shown in Fig. 6.4 includes the lower plate of substrate for the hexagonal resonator also. The frequencies of resonance have been measured experimentally. The effective side of the hexagon is obtained by considering, as in earlier cases, the magnetic wall to be shifted outward by an amount δ. Effective side 'a' is given by

$$a = A + \frac{2}{\sqrt{3}} \delta \qquad\qquad (6.10)$$

where A is the actual side of the hexagon. Theoretical and experimental values of the resonance frequencies for the hexagonal resonator have been compared in Table 6.4.

Table 6.3   Comparison of some of the resonances of hexagonal and circular resonators

Mode	λ for hexagonal resonator	λ for circular resonator
(1,1) even		
(1,1) odd	3.11a	3.413a
(2,1) even		
(2,1) odd	1.90a	2.057a
(0,1) even	1.5a	1.640a
(3,1) odd	1.25a	1.496a
(1,2) even	1.09a	1.179a
(3,1)* odd	1.09a	-
(4,1) even		
(4,1) odd	1.08a	1.182a
(5,1) even		
(5,1) odd	0.887a	0.979a

Table 6.4   Comparison of theoretically calculated and
            experimentally measured resonance frequencies
            for a regular hexagonal resonator

Effective side, a = 2.098 cm, ε_r = 2.47, d=1/16"

Mode	λ	Resonance Frequency	
		Theoretical	Experimental
(1,1) odd (1,1) even	3.11a	2.925 GHz	2.903 GHz
(2,1) even (2,1) odd	1.90a	4.787 GHz	4.790 GHz
(0,1) even	1.5a	6.066 GHz	5.981 GHz
(3,1) odd	1.25a	7.272 GHz	7.203 GHz
(1,2) even (3,1)* odd	1.09a	8.339 GHz	8.200 GHz
(4,1) even (4,1) odd	1.08a	8.408 GHz	8.413 GHz
(5,1) even (5,1) odd	0.887a	10.259 GHz	10.311 GHz
(6,2) even	0.866a	10.506 GHz	10.400 GHz
(3,2) even	0.75a	12.131 GHz	12.045 GHz

6.5 DISCUSSION

Lowest order and some higher order modes of resonances of triangular, rhombic and hexagonal resonators have been studied. In all the three cases, the measured resonance frequencies for various modes are in agreement with the theoretically computed values. The difference in the two sets of values is mainly due to the tolerance in the dielectric constant of the substrate. For rhombic and hexagonal resonators, some numerical errors may also be present because of finite number of ports considered along the interfaces. However, since the number of interconnecting ports is twelve along each side of triangular segments, this error is expected to be very small. Another source of error is that the expression (2.2) used for extension of the magnetic wall from the physical periphery is not strictly valid at the corners. Considering these sources of errors, the agreement between theoretical and experimental values of resonance frequencies is seen to be good.

The even mode resonances, of the hexagonal resonator considered, correspond to the case of a trapezoidal resonator. Thus, the results presented could be used for design of trapezoidal resonators also.

For the case of an equilateral triangle, a 60° - rhombus and a regular hexagon (the sides being equal in the three cases), the value of lowest order resonance frequency is

minimum for hexagon and maximum for triangle. For lowest order resonance, $\lambda = 1.5a$ for triangle, $\lambda = 2.34a$ for rhombus and $\lambda = 3.11a$ for hexagon.

The voltage variation around the periphery would pass through zero an even number of times. For the lowest order resonance frequency the voltage would have one cycle variation or would pass through the zero twice. The variation of $(\frac{1}{2},\frac{1}{2})$ even-odd mode for a 60°-rhombus passes through the zero twice around the periphery even though it is not the lowest order mode. However, this mode cannot be excited by a single feed line and two feed points are required to excite this mode. The voltage variation for the (0,1) even mode of a regular hexagon does not pass through zero around the periphery.

A hexagon has all the resonances of a triangle but only the even mode resonances of a rhombus (i.e. same as an equilateral triangle). This is because an even number of equilateral triangles (i.e. six) form a hexagon whereas an odd number of rhombii (i.e. three) make up the hexagonal shape. An odd mode of a rhombus cannot be excited in a hexagon since it leads to inconsistent boundary conditions along AB as shown in Fig. 6.16. For this very reason, all the resonances of a triangle are possible in a hexagon also.

At the lowest resonance frequency of hexagon, both even and odd modes are resonant. This behaviour is similar to
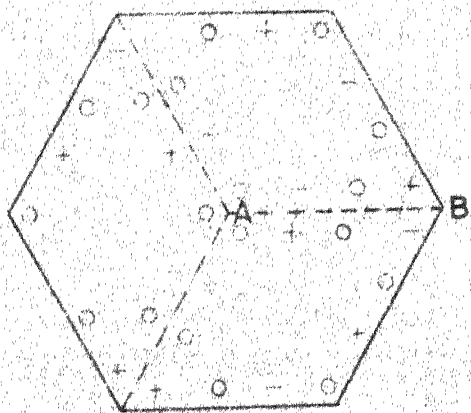
Fig. 6.16 Odd modes of rhombii in a hexagon.

that of a circular resonator where both even and odd modes are resonant (except for $(0,m)$ modes). For some higher resonance frequencies, either only the even mode or only the odd mode is resonant. This may be because a regular hexagon has axial symmetry of 60° only unlike a circle which is fully symmetrical.

The method of analysis used in this chapter may be applied to analyze planar resonators of many other shapes also. Resonators using annular ring structures, circular sectors and annular sectors can also be analyzed by the same technique. The Green's functions obtained in Chapter Four may be used for this purpose.

The resonator configurations studied in this chapter could also be used as microstrip antennas. This application is, however, not discussed in this thesis.

Chapter Seven
T-JUNCTIONS WITH TRIANGULAR GEOMETRY

T-junctions (or Y-junctions) are used in stripline and microstrip circuits to realize shunt connections of three transmission line sections. The T-junctions can be broadly considered to be of three different types depending upon the impedances of the three transmission lines. The three types of T-junctions, as shown in Fig. 7.1, are - i) junction where all three impedances are equal, ii) junction with only two impedances equal, and iii) junction with all three impedances unequal. A rectangular geometry is often used for these junctions. Like many other discontinuities, the T-junction discontinuity also generates parasitic reactances which affect the performance of the circuit containing the junction.

Two-dimensional analysis can be used to determine accurately the effect of junction reactances and of the presence of higher order modes produced thereby. Green's function for rectangular geometry given by (2.30) and the segmentation method discussed in Sec. 5.2.2 can be used to characterize a T-junction.

It is of interest to know if the use of a triangular geometry at the T-junction causes any reduction in the parasitic reactances. In this chapter, two kinds of T-junctions with
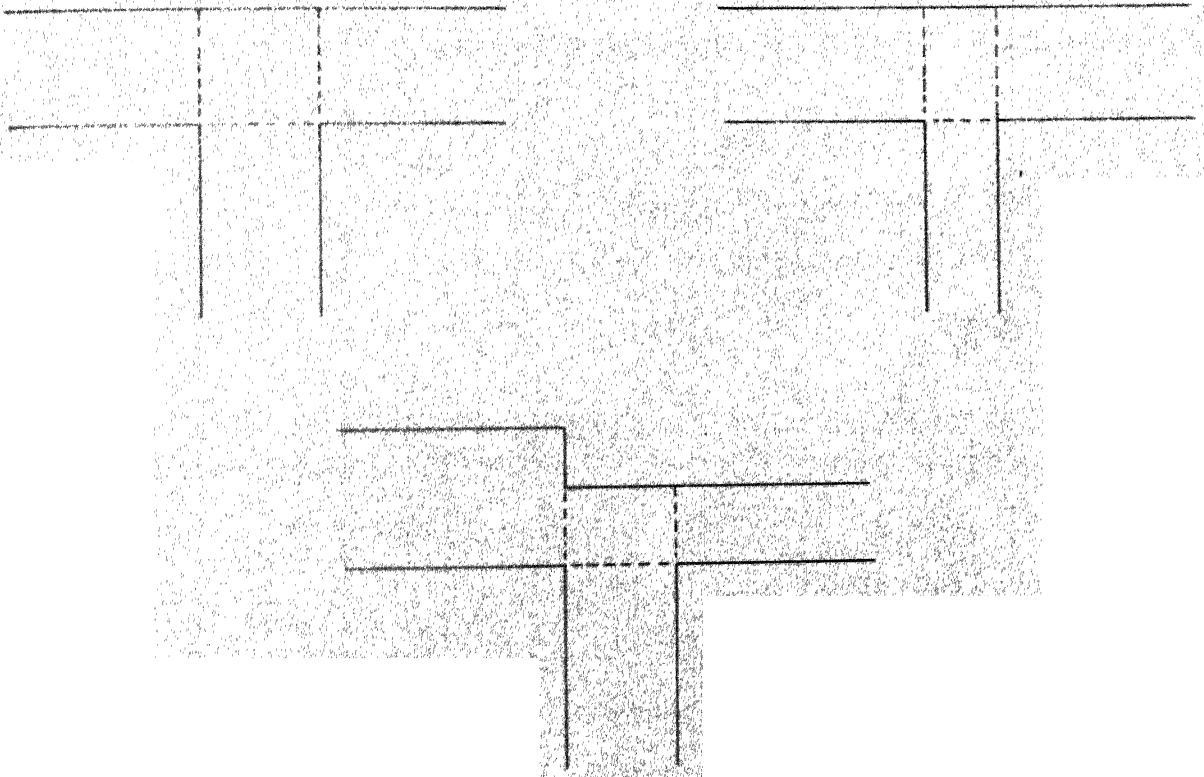
Fig. 7.1   Three types of T-junctions.

impedance ratios 1:1:1 and $(1/\sqrt{2})$:1:1 have been investigated
for this purpose. For T-junctions with impedance ratio 1:1:1,
it has been found that an equilateral triangular geometry at
the junction yields the best performance. A right-angled
isosceles triangular geometry yields the best performance
for T-junctions with impedance ratio $(1/\sqrt{2})$:1:1.

Method of Analysis

Z-matrices for the geometrical shapes are obtained
using the Green's functions given in Chapters Two and Three.
Integrals of eigenfunctions (appearing in Green's function
expansions) over widths of various ports are used in the
evaluation of Z-matrices. These integrals are listed in
Appendix A. Portions of outgoing transmission lines from
the junction are also modelled as planar rectangular compo-
nents. As discussed in Chapter Five, this process accounts for any
higher order modes excited by the discontinuities. The
Z-matrices of various components are combined using the
segmentation method. For higher accuracy, the ports corres-
ponding to the outgoing line sections are divided into multi-
ple subports. These subports are combined using the technique
described in Sec. 5.2.4. The S-matrix is obtained from the
overall Y-matrix at external ports using (5.24).

7.1 T-JUNCTIONS WITH EQUAL LINE IMPEDANCES

In this section, the case of T-junctions with equal line

impedances are considered. One of the applications of this type of junctions is the circuit for SPDT switches [33]. ·In these junctions, the widths of the three outgoing lines are equal and a square geometry is used at the junction. Under ideal conditions, the input reflection coefficient at the junction should be -1/3 and the transmission coefficient from one branch to another should be 2/3. However, due to dis-continuity reactances, the performance would differ from that of the ideal junction.

2-d analysis has been carried out for the rectangular T-junction. The circuit is divided into segments as shown in Fig. 7.2(a). The width of 50 Ω line is divided into six subports as shown in Fig. 7.2(b). It is found that the refle-ction coefficients differ from the ideal value of -1/3 and these deviations increase with frequency. The reflection coefficient at port 1 is shown as a function of frequency in Fig. 7.3 (curve 'a').

Since, the widths of the three outgoing lines are same, use of equilateral triangular geometry at the junction is explored. An equilateral triangle is used at the junction and the resulting T- or Y-junction (shown in Fig. 7.2(c)) is also analyzed using the 2-d approach. The reflection coefficient (equal at all three ports) is very close to the desired value of -1/3 and deviates only slightly at high fre-quencies. This reflection coefficient is shown as a function
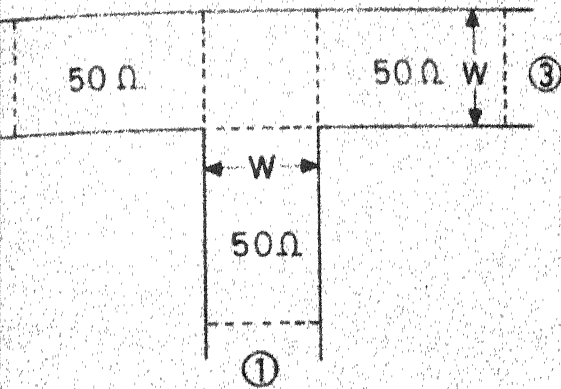
(a)
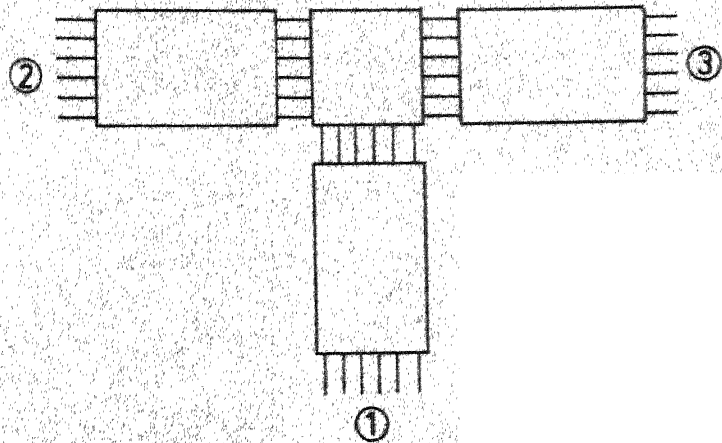
(b)
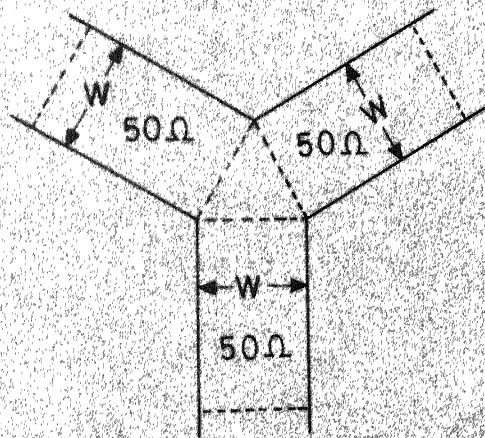
(c)

Fig. 7.2 (a) 1:1:1 rectangular T-junction.
         (b) Connection of segments of (a) using multiple subports.
         (c) 1:1:1 triangular T-junction.
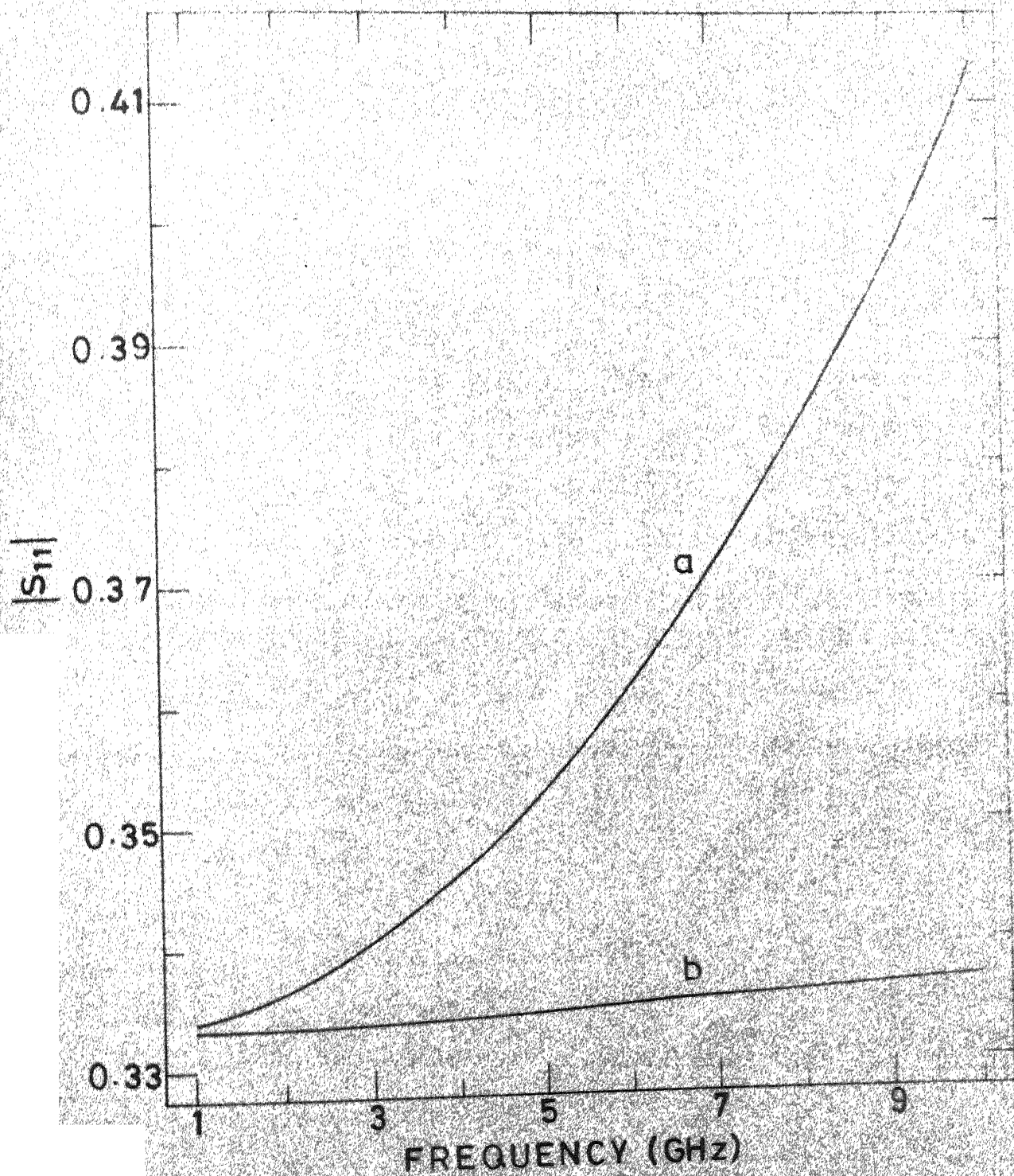
Fig 7.3 Variations of $|S_{11}|$ with frequency for 1:1:1 junctions

of frequency in Fig. 7.3 (curve 'b'). It is seen that the performance of equilateral triangular T-junction is much better than that of a rectangular T-junction.

To verify the improvement obtained by the use of equilateral triangle in T-junctions with impedance ratio 1:1:1, two T-junctions have been fabricated: one using a rectangular T-junction and the other using an equilateral triangular T-junction. These circuits have been fabricated in stripline configuration on polystyrene substrate (ε_r = 2.47, height d = 1/16"). As in the previous chapter, magnetic wall is considered to be shifted out from the physical periphery by an amount δ given by (2.2). For 50 Ω lines, the effective side of the equilateral triangle is 0.381 cm. and the corresponding physical dimension is 0.241 cm. In the case of rectangular T-junction, these dimensions correspond to the square region at the junction. A photograph of the lower plates of substrate for the two circuits is shown in Fig.7.4. For measurement of input VSWR, ports 2 and 3 of T-junction are terminated in matched loads and input reflection coefficient is measured at port 1. The variations of VSWR with frequency for the two circuits are shown in Fig. 7.5. The theoretically predicted variations are also shown in the figure.

7.2 T-JUNCTIONS WITH IMPEDANCE RATIO $(1/\sqrt{2})$:1:1

In this section, T-junctions with one line impedance
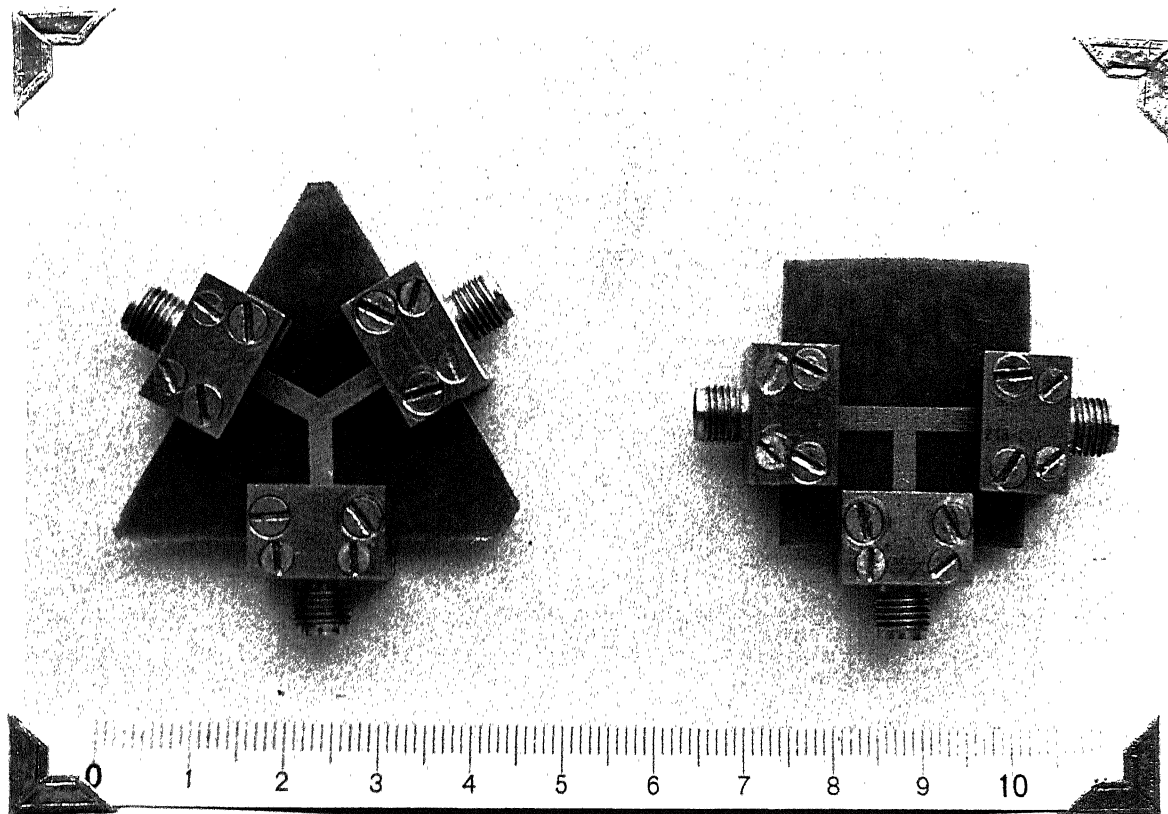
Fig. 7.4 Experimental T-junctions (impedance ratio 1:1:1)
using rectangular and triangular geometries with
the top dielectrics and ground planes removed.
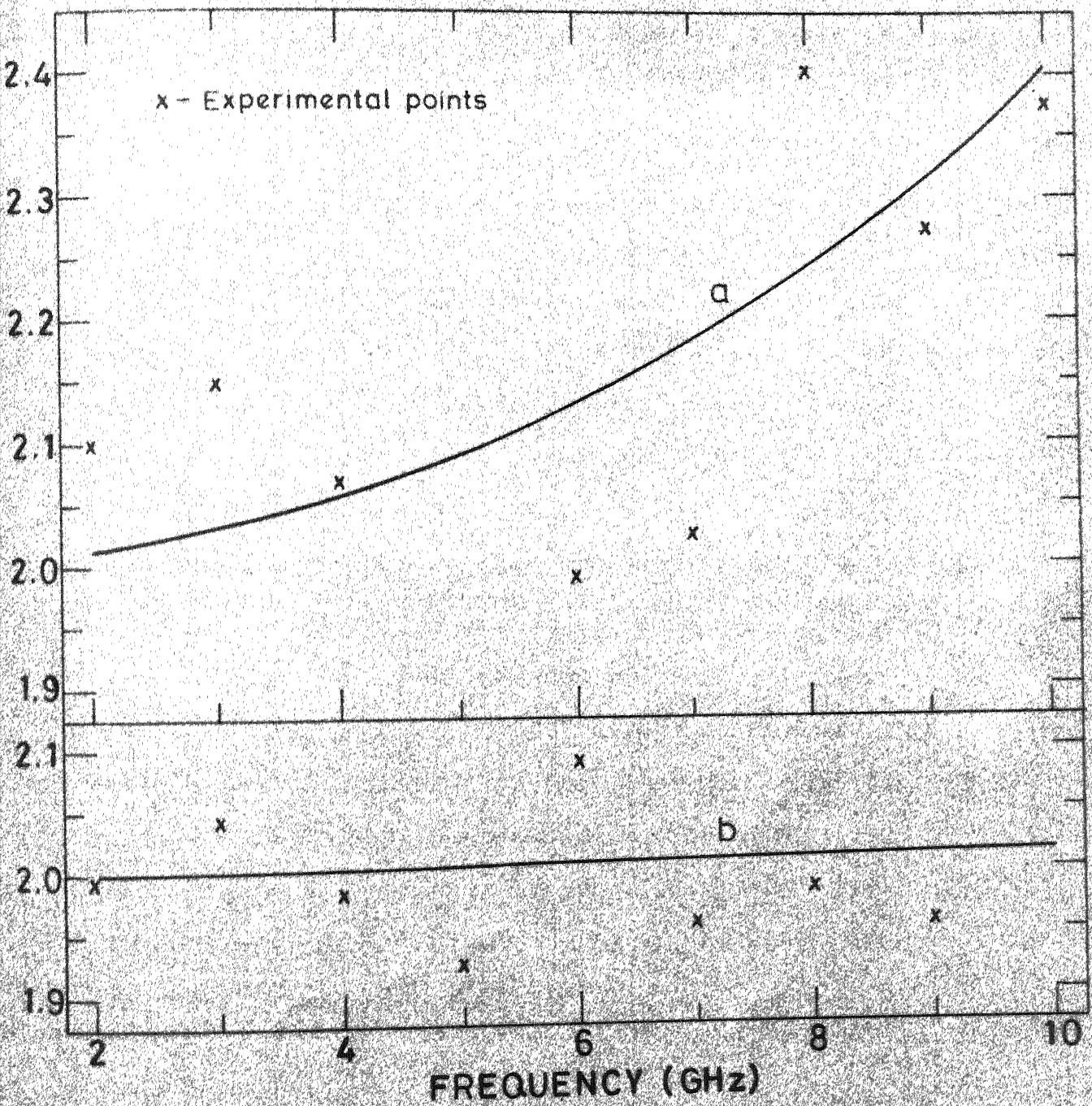
Fig. 7.5 Variations of VSWR with frequency (theoretical and experimental) for two cases.

equal to $1/\sqrt{2}$ times the other two (equal) line impedances are considered. These junctions occur frequently in circuits such as power dividers, hybrids, etc. [28]. In these junctions the effective widths (in the planar waveguide model) of the three lines are in the ratio $\sqrt{2}:1:1$. Usually, a rectangular geometry is used at the junction. In ideal case, the input reflection coefficient at the line with lower impedance should be $(1 - \sqrt{2})/(1 + \sqrt{2})$ or -0.172. The characteristics of a practical T-junction would however be different from the desired ideal values because of the discontinuity effects.

The rectangular junction has been analyzed using 2-d approach. The circuit is divided into segments as shown in Fig. 7.6(a). As before, for higher accuracy, the ports on the 50 Ω main line are divided into six subports and the port on 35.35Ω line is divided into eight subports. It is found that the performance of the junction differs from the ideal case and it deteorates with increase in frequency. The reflection coefficient at port 1 is shown as a function of frequency in Fig. 7.7 (curve 'a').

Since the effective widths of the three outgoing lines are in the ratio $\sqrt{2}:1:1$, use of a right-angled isosceles triangle (ratio of sides being $\sqrt{2}:1:1$) is explored. A right-angled isosceles triangle (in the effective magnetic wall model) is used at the junction. The T-junction (shown in
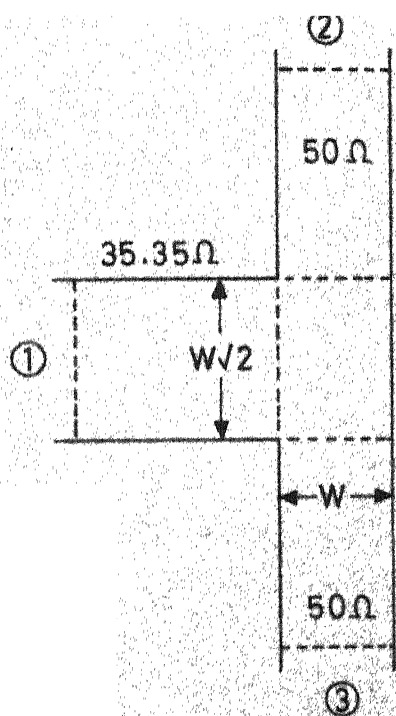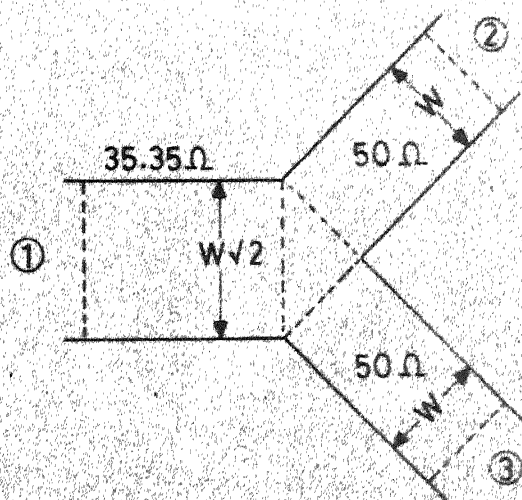
Fig . 7.6 $\frac{1}{\sqrt{2}}$:1:1 rectangular and triangular T-junctions .
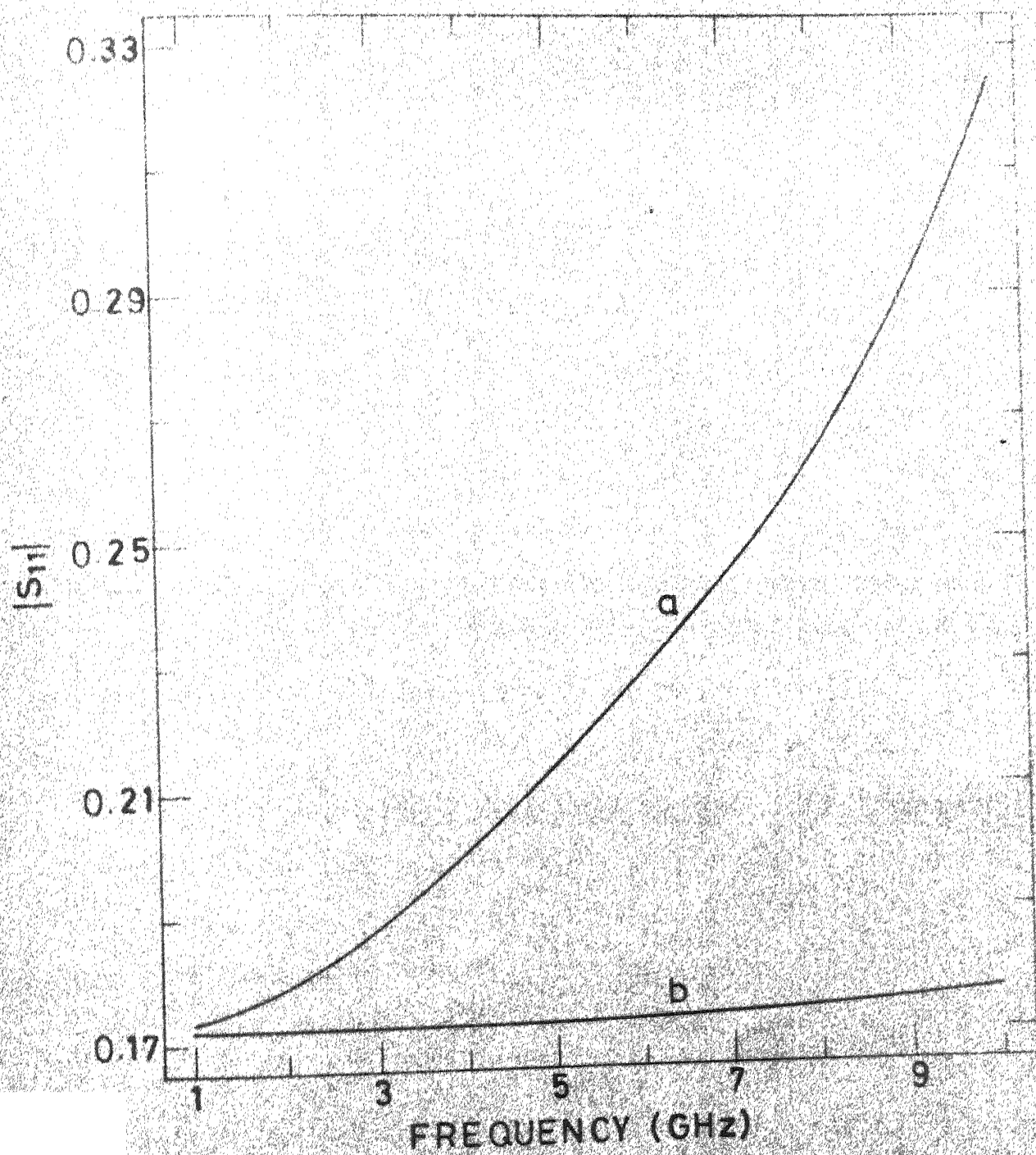
Fig. 7.7   Variation of $|S_{11}|$ with frequency for $\frac{1}{\sqrt{2}}$ 1:1   T-junction

Fig. 7.6(b)) is analyzed using the 2-d approach. The performance is very close to the ideal behaviour upto very high frequencies and the deviation from the ideal case is negligible. The reflection coefficient at port 1 is shown as a function of frequency in Fig. 7.7 (curve 'b'). It is seen that the performance of right-angled isosceles triangular T-junction is much better than that of a rectangular T-junction.

It should be noted that, for a T-junction with impedance ratio $(1/\sqrt{2}):1:1$, a right-angled isosceles triangle is proposed in the effective dimensions and not in the physical dimensions. Only the effective widths of the three outgoing lines are in the ratio $(1/\sqrt{2}):1:1$ and the actual geometry at the junction is not a right-angled triangle. In a typical case, the physical periphery and the magnetic wall location are shown in Fig. 7.8.

To verify (experimentally) the improvement caused by using a triangular junction, a quarter wave matching section is incorporated at the input end as shown in Fig. 7.9. Two circuits, one using a rectangular junction and the other using a right-angled isosceles triangular junction, have been fabricated in stripline configuration on polystyrene substrate $(\varepsilon_r = 2.47$, height d = 1/16"). As before, the magnetic wall is considered to be shifted out from the physical periphery by an amount δ given by (2.2). Various effective and actual dimensions of the two circuits are as follows :
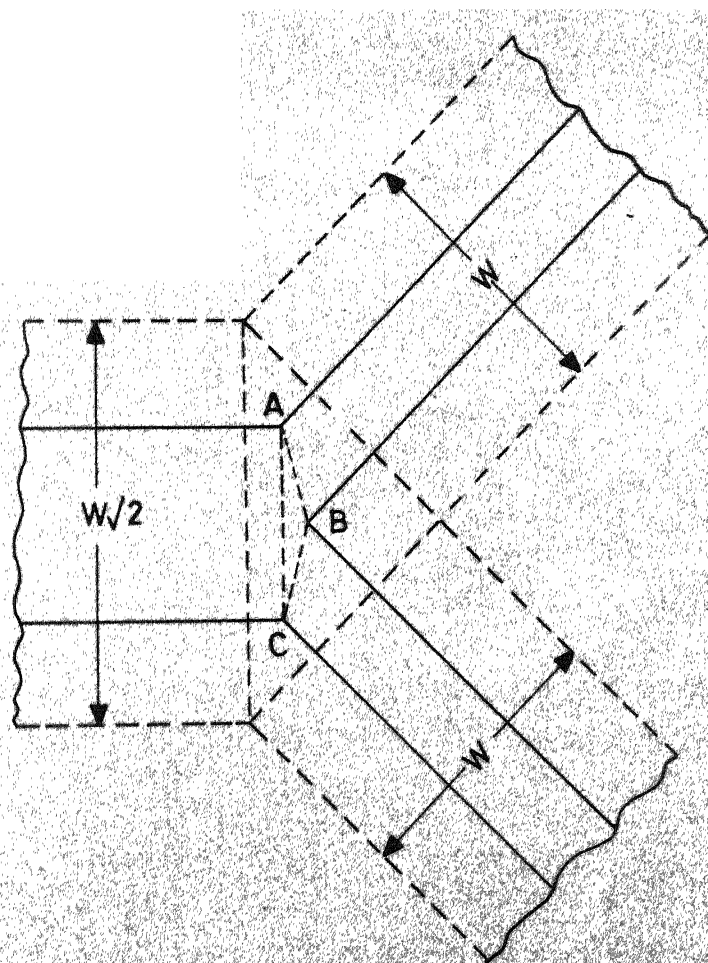
Physical boundary
— — — — — — Magnetic wall

Fig. 7.8 A right-angled isosceles triangular
T-junction.
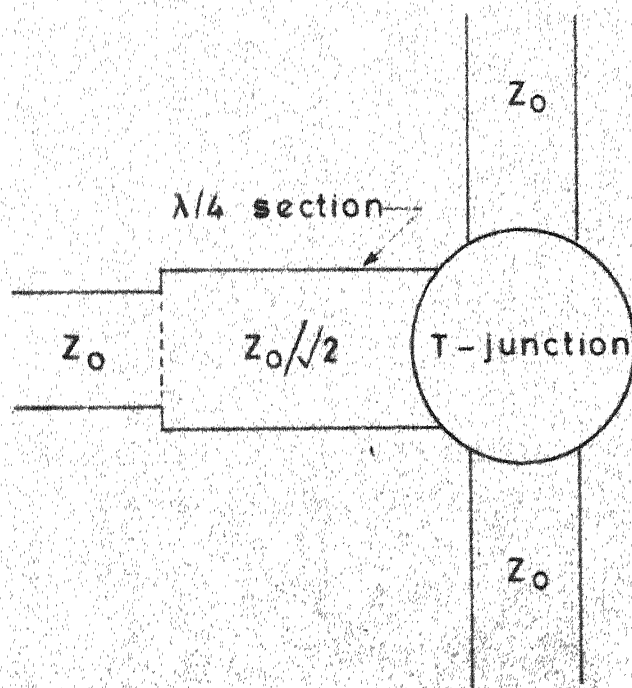
Fig. 7.9   Matching section with $\frac{1}{\sqrt{2}}$:1:1 T-junction

	Effective	Actual

a) Rectangular T-junction

i) 50 Ω side of rectangle — 0.381 cm. — 0.241 cm.

ii) 35.35 Ω side of rectangle — 0.539 cm. — 0.398 cm.

iii) Length of rectangular segment on the input side — 1.945 cm. — 1.945 cm.

b) Triangular T-junction

i) 50 Ω side of triangle — 0.381 cm. — 0.244 cm. (side AB in Fig. 7.8)

ii) 35.35 Ω side of triangle — 0.539 cm. — 0.398 cm.

iii) Length of the rectangular segment on the input side — 1.910 cm. — 1.950 cm.

A photograph of the lower plates of substrate for the two circuits is shown in Fig. 7.10. 2-d analysis is used to obtain the theoretical results. Matching section, geometry used at the junction, and portions of outgoing transmission lines are modelled as planar segments. The theoretical and experimental variations of input VSWR with frequency for the circuit using rectangular junction are shown in Fig. 7.11. Experimentally observed variation of input VSWR for the circuit using triangular junction is compared with the theoretical variation in Fig. 7.12.

7.3 APPLICATIONS OF TRIANGULAR JUNCTIONS

The T-junctions discussed in the earlier sections are widely used in various microwave circuits. The performance
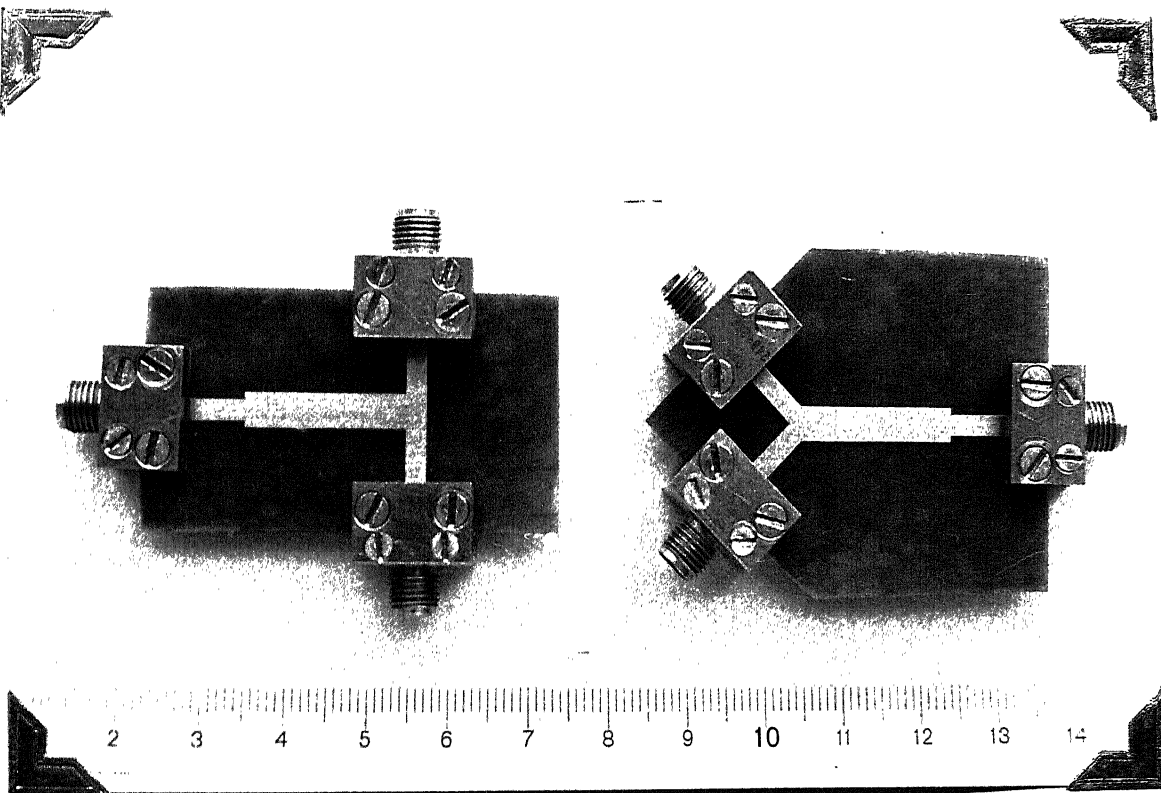
Fig. 7.10   Experimental circuits of $(1/\sqrt{2}):1:1$
T-junction with matching section on input
side using rectangular and right-angled
isosceles triangular junctions with the top
dielectrics and ground planes removed.
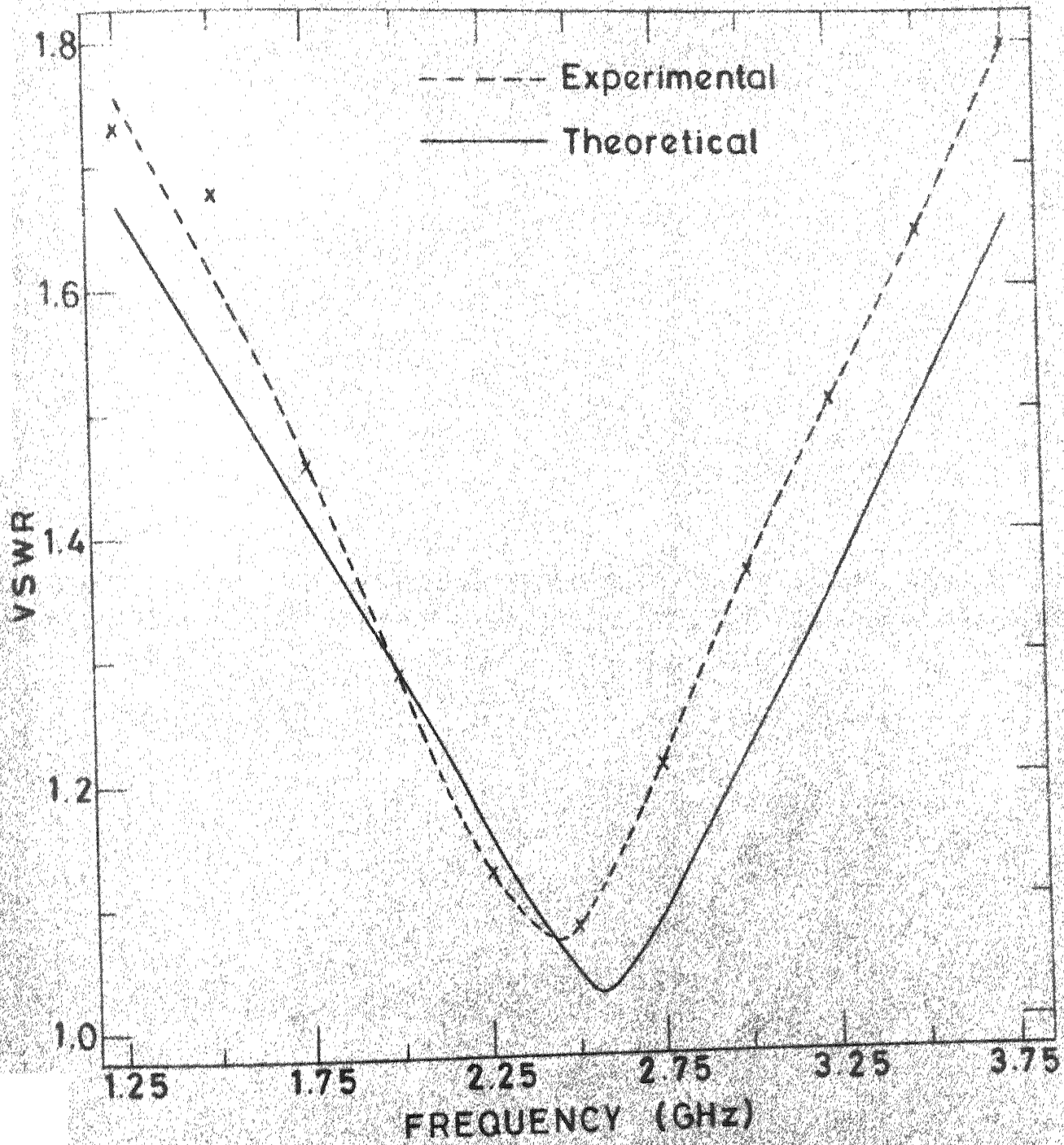
Fig. 7.11 Variations of VSWR with frequency for circuit using rectangular junction
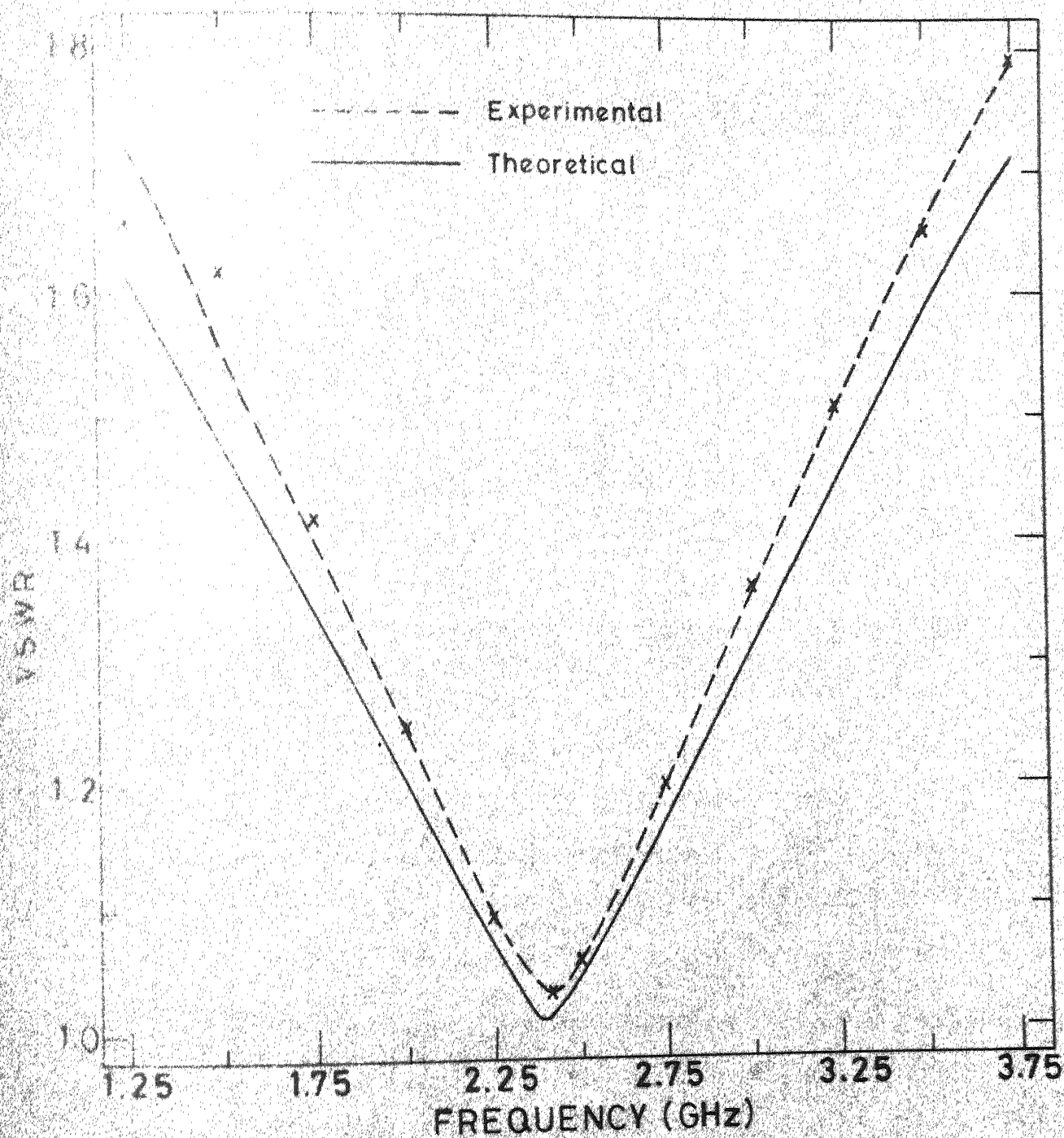
Fig. 7.12 Variations of VSWR with frequency for circuit using triangular junction.

of such circuits can be improved by using suitable triangular shaped junctions. In this section, two examples of these circuits are being given to bring out the improvement caused by the use of triangular junctions.

Consider an in-phase power divider circuit using single matching sections $(Z = Z_0\sqrt{2})$ on the output sides as shown in Fig. 7.13(a). The circuit uses a T-junction with impedance ratio $(1/\sqrt{2}):1:1$ and hence a right-angled isosceles triangle can be used at the junction as shown in Fig. 7.13(b). The 2-d approach is used to analyze both these circuits designed at 6 GHz center frequency. The variations of input VSWR with frequency are shown in Fig. 7.14 (curve 'a' for the circuit using rectangular junction and curve 'b' for circuit using triangular junction). It is seen that the center frequency is shifted from the design objective in both the cases. Further, the circuit using triangular junction has a lower value of VSWR (= 1.007) at its center frequency than for the circuit using rectangular junction (where VSWR = 1.052).

Another example of a circuit using T-junctions with impedance ratio $(1/\sqrt{2}):1:1$ is a branch-line hybrid shown in Fig. 7.15(a). Triangular junctions can be used in this case also by making the quarter wave sections curved as shown in Fig. 7.15(b). For carrying out its 2-d analysis, the circuit should be divided into rectangular, triangular, and annular sector shaped segments. However, the characterization of an

Z_0

$Z_0\sqrt{2}$

$\lambda/4$

$2Z_0$

$\lambda/4$

Z_0

(a)

$Z_0\sqrt{2}$

Z_0

Z_0

$\lambda/4$

$Z_0\sqrt{2}$

$2Z_0$

(b)

Z_0

$Z_0\sqrt{2}$

$\lambda/4$

Z_0
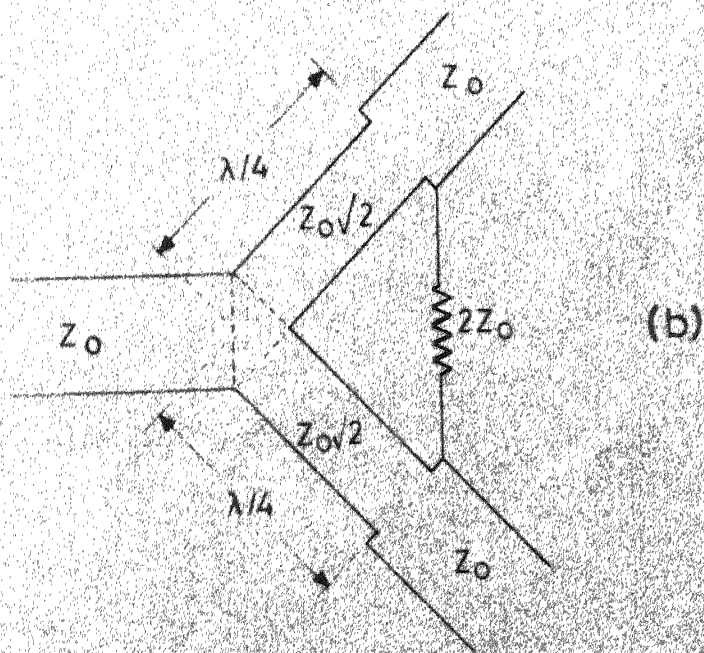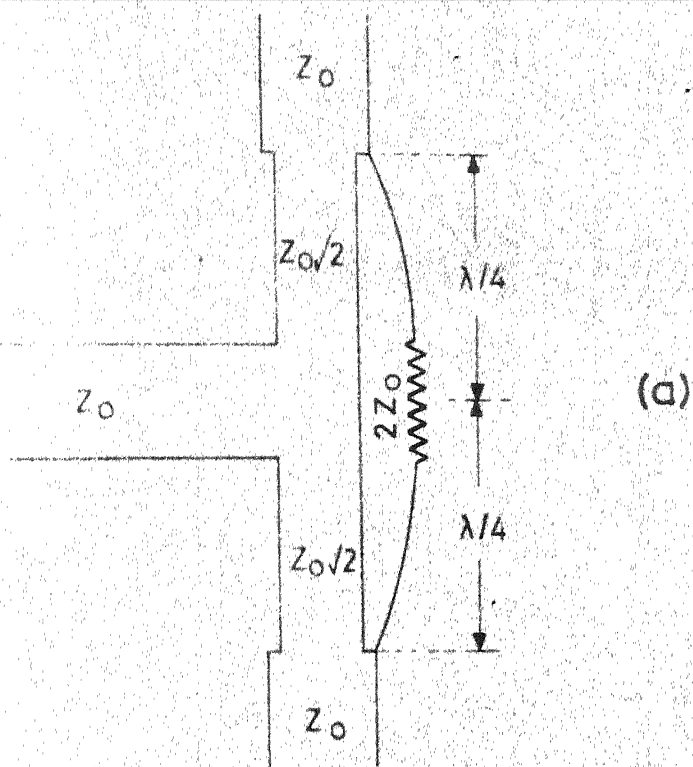
Fig. 7.13   Power divider using
(a) rectangular junction
(b) triangular junction

a – Rectangular junction
b – Triangular junction
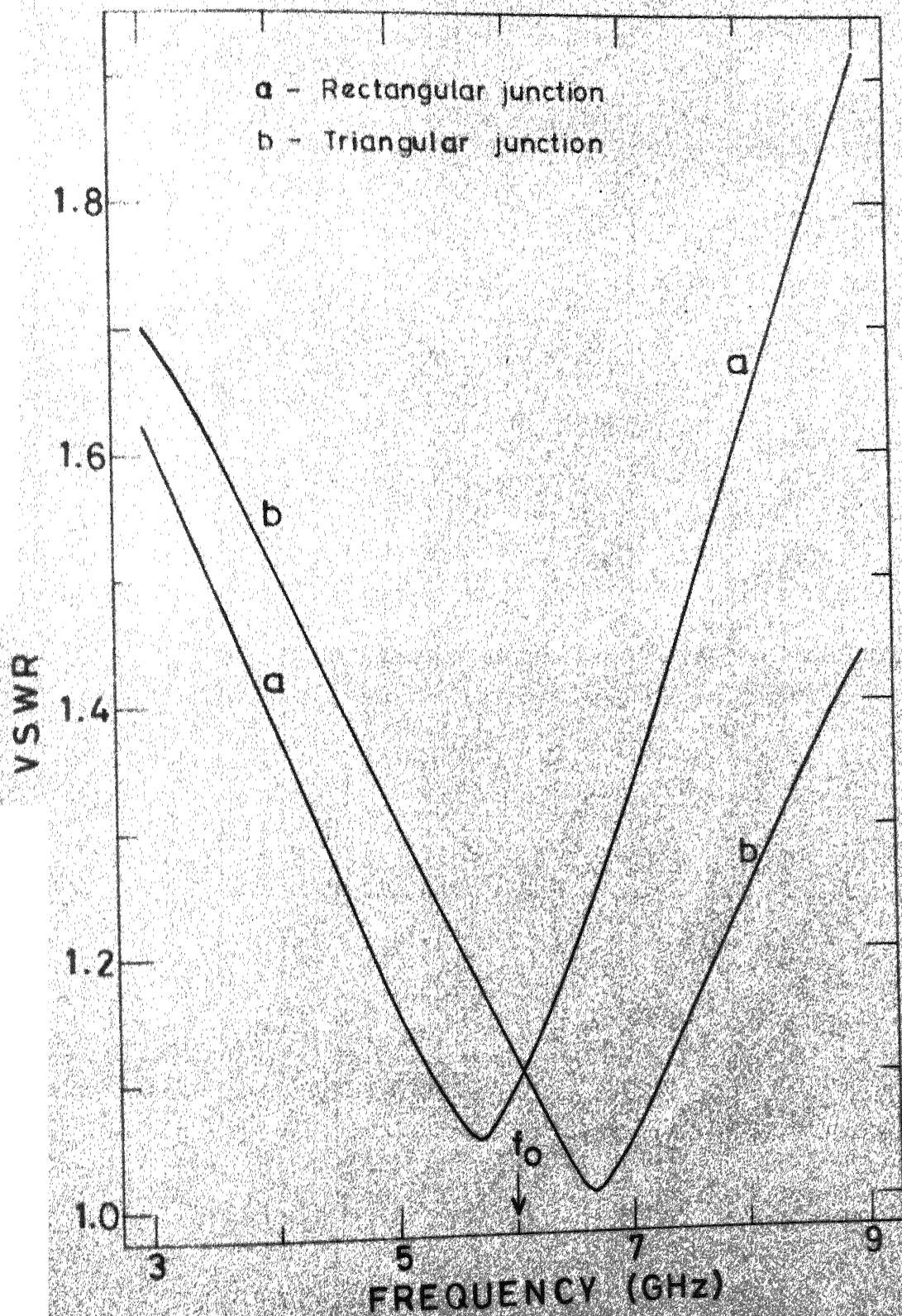
Fig. 7.14 Variations of VSWR with frequency for power divider
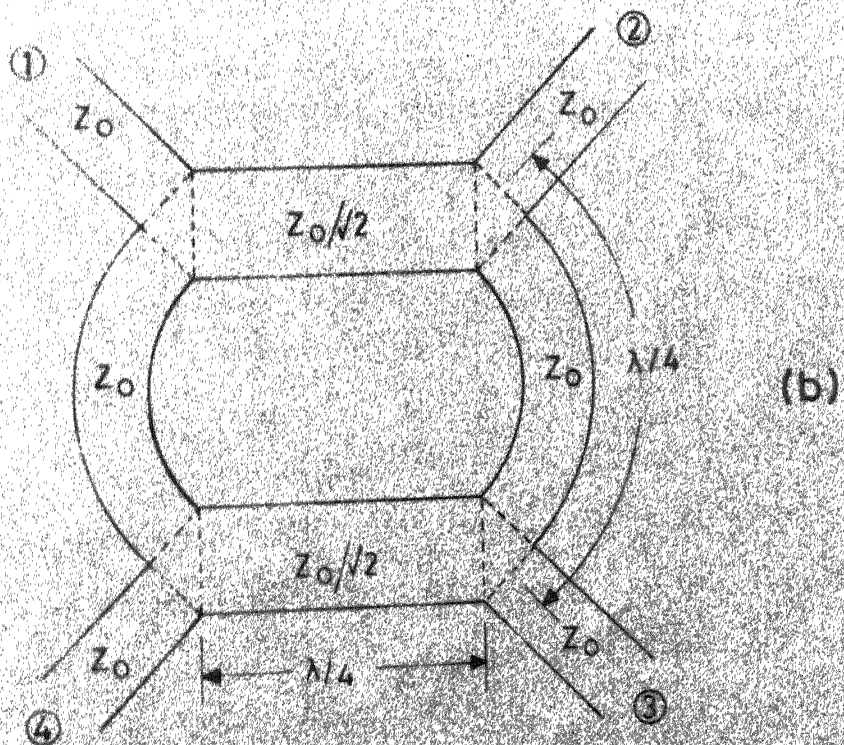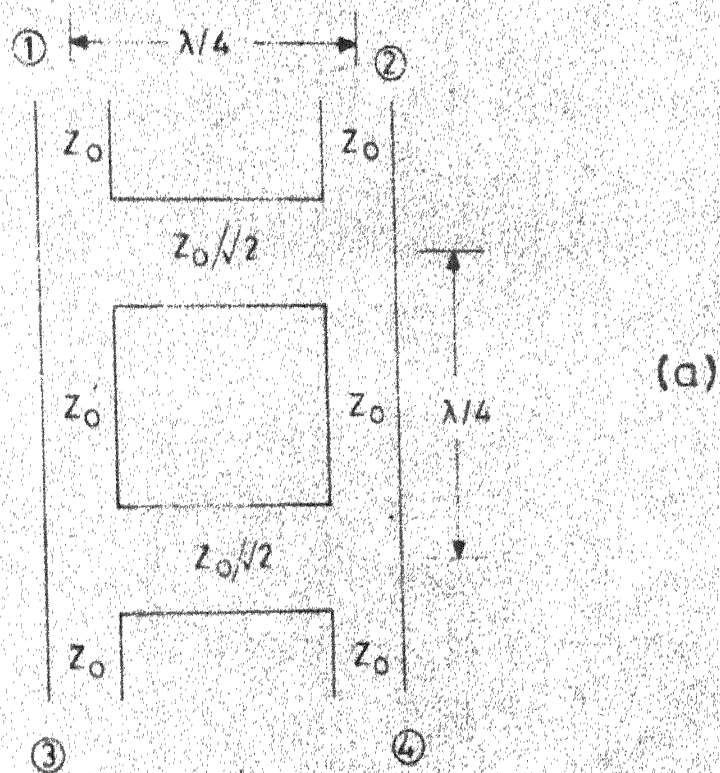
Fig. 7.15 Branch line hybrid using
(a) rectangular junctions
(b) triangular junctions

annular sector shaped segment can be approximated by modelling it as a rectangular segment . 2-d analysis for the circuit shown in Fig. 7.15(b) has been carried out at 4 GHz. center frequency and by modelling the annular sector shaped segments also as rectangular segments. The input VSWR's (equal at all ports) for the two circuits shown in Fig. 7.15 are plotted as a function of frequency in Fig. 7.16 (curve 'a' for the circuit using rectangular junctions and curve 'b' for the circuit using triangular junctions). As in the case of power divider circuits, the center frequency of hybrid is shifted in both the cases. However, the shift in case of the circuit using triangular junctions is much lower (= 220 MHz) than that (= 870 MHz) for the circuit using rectangular junctions. The circuit using triangular junctions has a lower value of VSWR (= 1.013) at its center frequency than for the circuit using rectangular junctions (where VSWR=1.093).

7.4   DISCUSSION

It has been shown in this chapter that, the affect of parasitic reactances can be reduced for two kinds of T-junctions by using triangular geometries at the junction. For a T-junction with equal line impedances, an equilateral triangle is proposed and for a T-junction with impedance ratio $(1/\sqrt{2}):1:1$, a right-angled isosceles triangle (in magnetic wall model) is proposed. Improvement using trian-gular shaped junctions has been verified experimentally for both the cases.
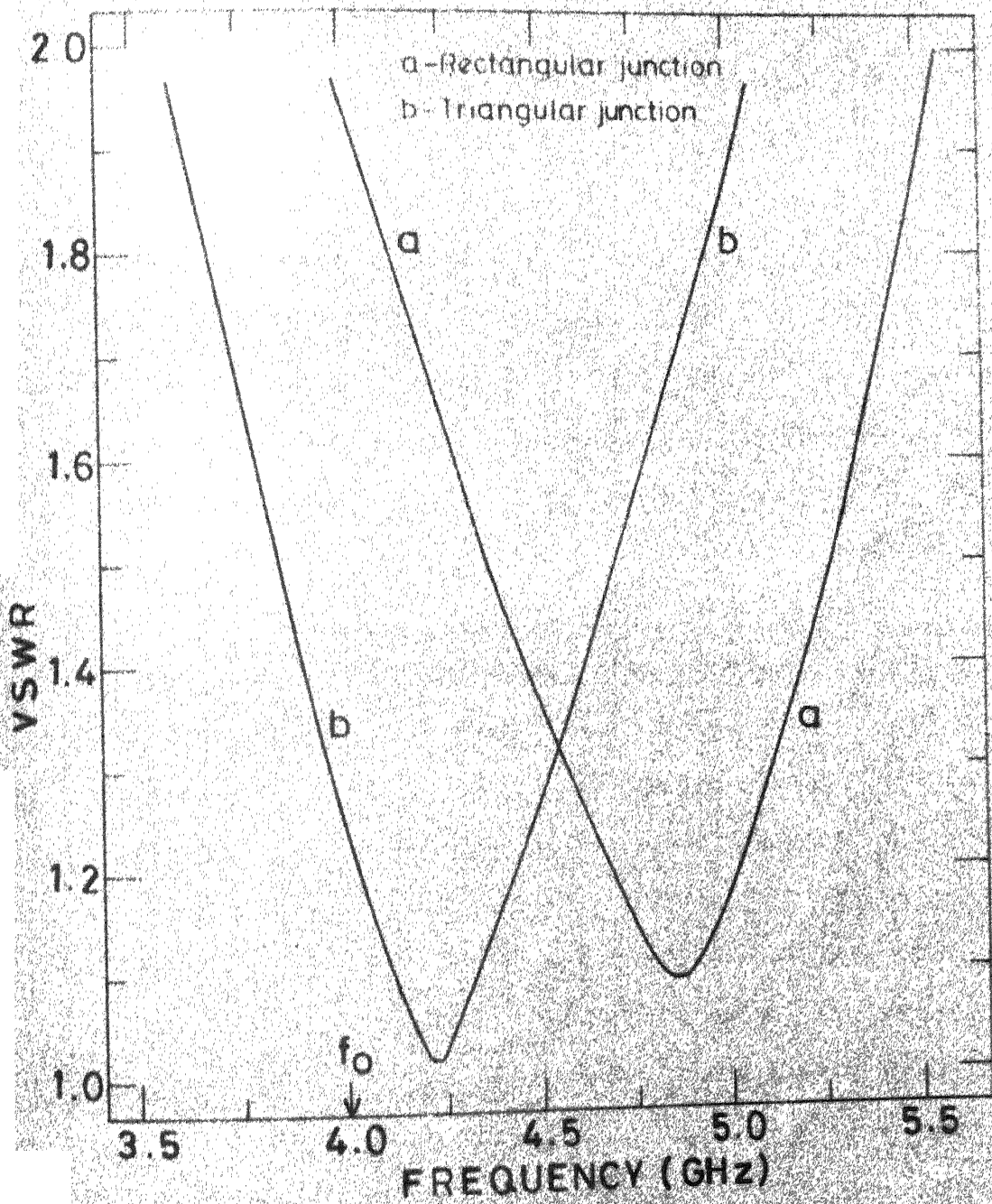
Fig . 7 .16   Variations of VSWR with frequency for branch-line hybrid .

It is perhaps significant to compare the areas of junctions with different geometries. For T-junctions with equal impedances, effective area at the junction is W^2 for the rectangular junction and $W^2\sqrt{3}/4$ for the equilateral triangular junction where W is the effective width of the outgoing transmission lines. For T-junctions with impedance ratio $(1/\sqrt{2}):1:1$, effective area at the junction is $W^2\sqrt{2}$ for the rectangular junction and $W^2/2$ for the right-angled isosceles triangular junction where W is the effective width of the two symmetric outgoing transmission lines. Thus, it is observed that the reduction in parasitic reactances obtained by the use of triangular junctions is associated with the reduced junction area. Also, for the two types of junctions studied, the corresponding triangles have the least area at the junction. To support the argument given above for improvement in parasitics, optimization was carried out for T-junctions with impedance ratio $(1/\sqrt{2}):1:1$. Three geometries — i) rectangular, ii) equilateral triangular, and iii) right-angled isosceles triangular were tried at the junction (as shown in Fig. 7.17), and their dimensions were treated as variable parameters. These three junctions were optimized to minimize the deviation of reflection coefficient from its ideal value of -0.172. Least square optimization procedure described in Appendix B is used. In each of the three cases, the minimum value of deviation occurs when the dimensions at the junction
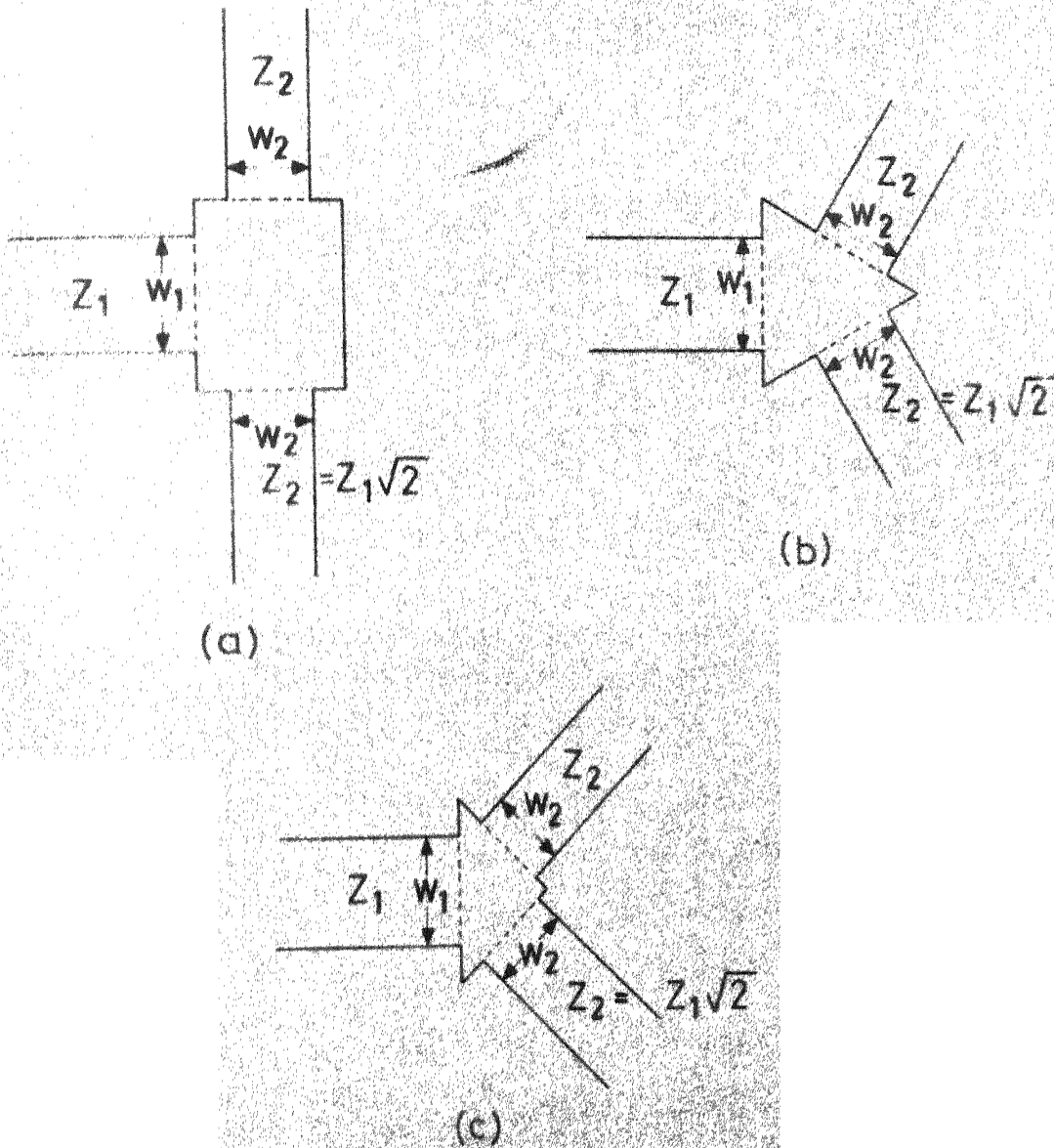
Fig . 7.17 $\frac{1}{\sqrt{2}}$:1:1 T-junctions using various geometrical shapes .

are minimum for that geometry (i.e. sides of rectangle are W_1 and W_2, side of equilateral triangle is W_1 and the longer side of the right-angled isosceles triangle is W_1). Amongst the three optimum values of reflection coefficient, the value of input reflection coefficient for the case of equilateral triangle lies between the other two optimum values. For a typical case ($\varepsilon_r = 2.55$, $d = 1/16"$, $Z_2 = 50\,\Omega$, $f = 10$ GHz) the input reflection coefficients for rectangular, equilateral triangular and right-angled isosceles triangular T-junctions have the magnitudes 0.386, 0.214 and 0.189 respectively. Area of the equilateral triangular junction is $W_2^2\sqrt{3}/2$ as compared to $W_2^2\sqrt{2}$ and $W_2^2/2$ for the rectangular and right-angled isosceles triangular junctions respectively. In view of the observations summarized above, it may be stated that the equilateral triangle and the right-angled isosceles triangle have the optimal geometry for the T-junctions with equal line impedances and line impedances in ratio $(1/\sqrt{2}):1:1$ respectively. These observations can be extended to T-junctions with arbitrary impedances also. For a T-junction with arbitrary impedances, a triangle with sides equal to the effective widths of the three outgoing lines has the least area. It is expected that use of this type of triangles would minimize parasitic react-ances for T-junctions with arbitrary impedances also. Analysis of these junctions can be carried out using contour integral method [1] of 2-d approach.

In both the circuit examples considered in Sec. 7.3, a shift in the center frequency is observed. To obtain minimum VSWR at the center frequency, changes in lengths of matching sections are needed. Such changes are required since in 2-d analysis the matching sections are modelled more accurately and the actual dimensions may no longer remain $\lambda/4$. These changes can be obtained by optimizing the lengths of various matching sections so that the magnitude of S_{11} is minimized. For the power divider circuit, there would be only one variable parameter in optimization. Thus, the circuit analyzed would correspond to an optimum design at some other center frequency and the VSWR obtained at that frequency is the minimum obtainable for that center frequency. However, for the branch-line hybrid circuit, there would be two variable parameters in optimization. Thus, the VSWR obtained at the center frequency need not correspond to the minimum obtainable for that center frequency.

Besides power dividers and branch-line hybrids, the T-junctions discussed in this chapter are used in stubs, SPDT switches, ratrace hybrids and branch-line hybrids. Triangular T-junctions can be used in these circuits to reduce the effect of parasitics. Improved designs for power divider circuits and branch-line hybrid using triangular T-junctions have been obtained in Chapter Eight.

Chapter Eight

OPTIMIZATION OF STRIPLINE AND MICROSTRIP CIRCUITS
USING 2-D APPROACH

Stripline circuits contain many discontinuities whose reactances lead to degradation of circuit performance. The equivalent circuits for discontinuities are not very accurate at high frequencies or when the field perturbations caused by the neighbouring discontinuities interact with each other. In the previous chapter, 2-d approach has been used to characterize T-junctions and for analysis of some circuits which contain T-junctions. It has been pointed out there that in the design of power dividers and branch-line hybrids the quarter wave matching sections do not yield the lowest VSWR at the center frequency and optimization needs to be carried out.

In this chapter, 2-d analysis has been used in the optimization of in-phase 3 db power dividers and branch-line hybrid circuits [28].

8.1   IN-PHASE POWER DIVIDERS

Three types of power divider circuits have been considered as shown in Fig. 8.1. These are : i) a circuit with single matching section $(Z = Z_0/\sqrt{2})$ on the input side, ii) a circuit with single matching sections $(Z = Z_0\sqrt{2})$ on the output sides, and iii) a circuit with a matching section $(Z = Z_0/2^{1/4})$ on the input side and matching sections $(Z = Z_0 \, 2^{1/4})$ on the

Z_0

Z_0 $Z_0/\sqrt{2}$

Z_0

Z_0

$Z_0/2$

Z_0

$Z_0/\sqrt{2}$

Z_0

Z_0

$2^{1/4} Z_0$

Z_0 $2^{-1/4} Z_0$

$2^{1/4} Z_0$

Z_0
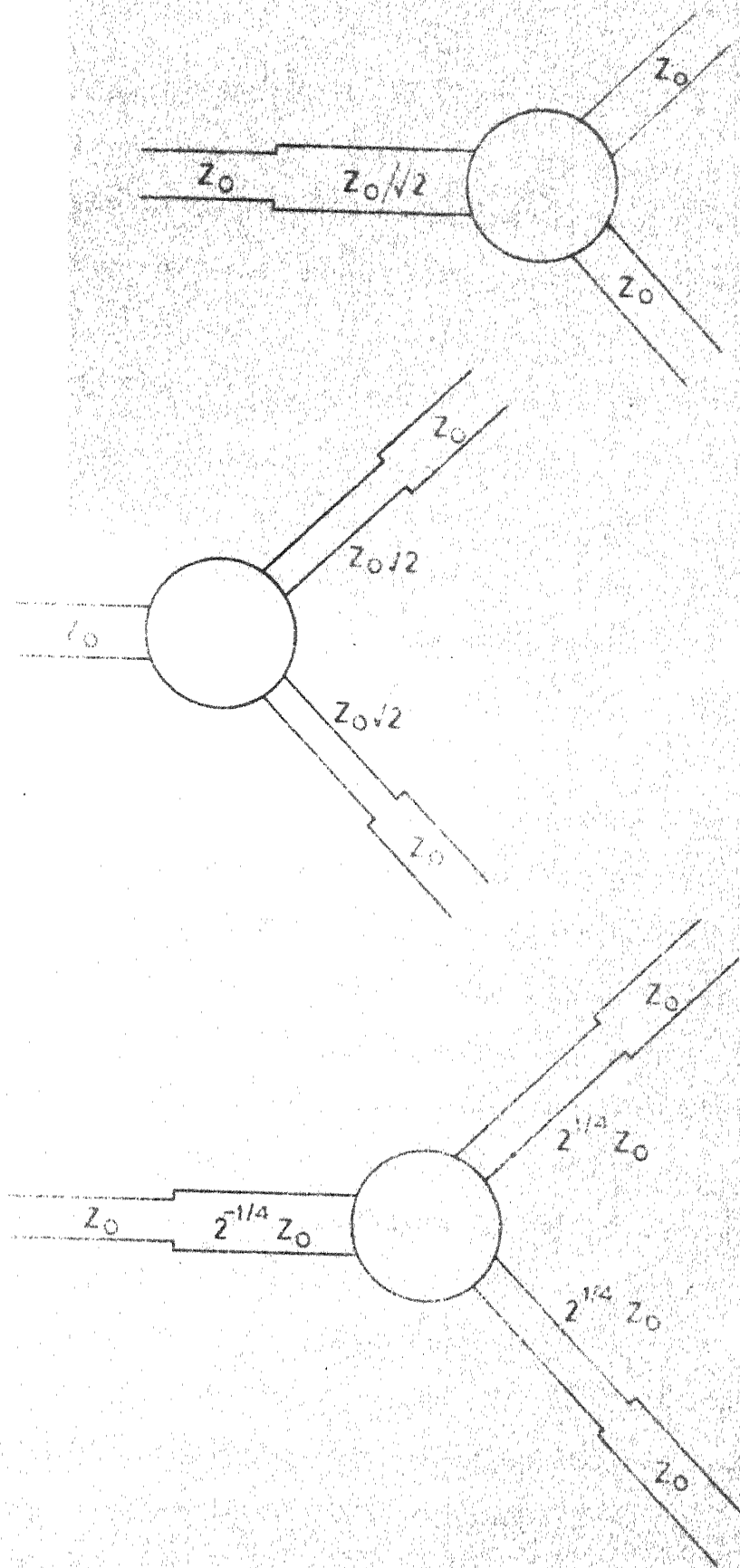
Fig 8.1   Three types of power dividers

output sides. Theoretically (i.e. in absence of discontinuity reactances and any higher order modes) each of the matching sections should be quarter wavelength long. Output VSWR and the isolation between two output ports are improved by connecting a resistance of value $2Z_o$ between the two outgoing lines at quarter wavelength away from the junction [28].

Each of the three types of power divider circuits (Fig. 8.1) uses a T-junction with impedance ratio $(1/\sqrt{2}):1:1$. Thus, their designs can be improved by using right-angled isosceles triangular junctions as discussed in the previous chapter. Optimization procedure is used to obtain lengths of various matching sections so that the input reflection coefficient is minimized at the center frequency. For this purpose, matching line sections and portions of line lengths on the three outgoing transmission lines are modelled as rectangular planar segments. For obtaining the input reflection coefficien the symmetry in the circuit is exploited and only the even mode half-section is analyzed. The case of power divider with matching section on the input as well as the output sides, and its even mode half-section are shown in Fig. 8.2. Overall input reflection coefficient is same as the S_{11} for the even mode half-section. A least square optimization method is used to minimize $|S_{11}|$ for the even mode with 10 GHz center frequency. The optimization procedure used is described in Appendix B. The design and performance data (input VSWR's) for the three types of circuits is given in Table 8.1.
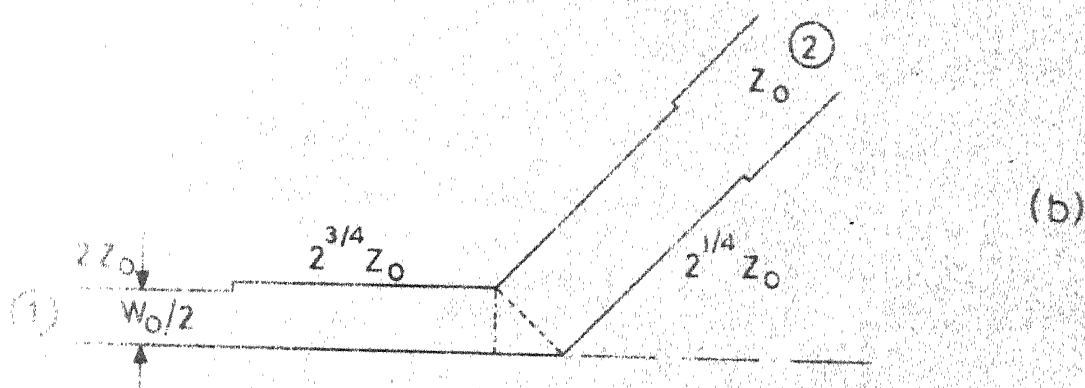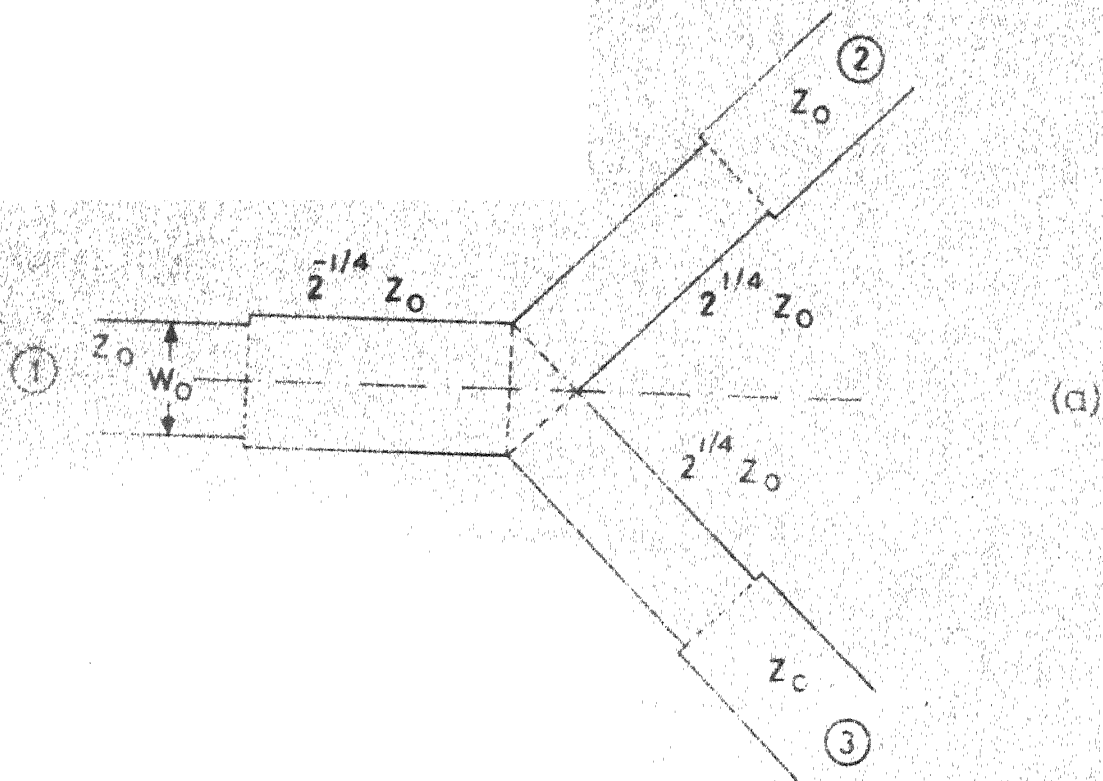
Fig. 8.2 (a) Power divider with matching sections
at both sides and its
(b) even mode half-section

Table 8.1   Design and performance data of power dividers
using triangular T-junctions

$(\varepsilon_r = 2.55, \quad h = 1/16")$

Configuration	$|S_{11}|$ at 10 GHz	Bandwidth (VSWR < 1.05)	Optimized lengths of matching sections
Single section at input	0.0043	9.5 to 10.5 GHz	0.425 cm.
Single sections at outputs	0.0017	9.55 to 10.55 GHz	0.415 cm.
Matching sections at input and at outputs	0.0034	8.15 to 11.3 GHz	0.436 cm. 0.429 cm.

To reduce output VSWR, an isolation resistance is connected between the two outgoing lines from the T-junction. This is shown in Fig. 8.3 for the circuit with single matching sections at the outputs and its odd mode half-section. The lengths of various matching sections (having been determined to minimize $|S_{11}|$) are now fixed and objective is to minimize $|S_{22}|$ by allowing the isolation resistance and its position to be varied.

It should be noted here that the isolation resistance does not affect the performance of the even mode half-section since in the even mode case the isolation resistance is open circuited in the middle. Also, to minimize the output VSWR it would be sufficient to minimize the $|S_{22}|$ for the odd mode case since S_{22} for the even mode half-section is almost zero at the center frequency.

The analysis of odd mode half-section requires characterization of a segment with a resistance connected to ground from a specified location. This can be obtained by having a port of small width (equivalent to the width of the chip resistor to be used) at the position of the isolation resistance and terminating this port to ground through a resistance $R/2$. Width of the chip resistor has been assumed to be 0.5 mm in the computations. The impedance matrix at the remaining ports (with one port connected to ground through a resistance $R/2$) is computed as follows.
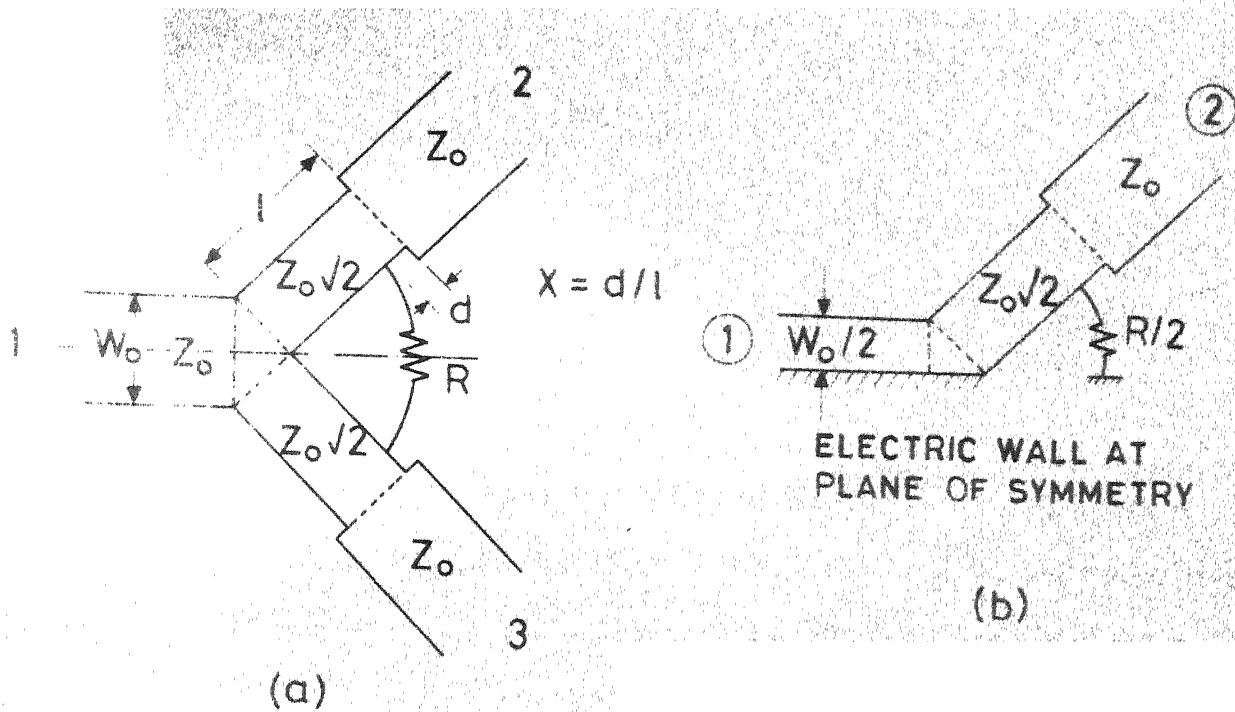
Fig 8.3 (a) Power divider with matching sections
at outputs and its (b) odd mode
half-section

Let the impedance matrix of the segment be partitioned as

$$\begin{bmatrix} \underline{v}_1 \\ v_r \end{bmatrix} = \begin{bmatrix} \underline{z}_{11} & \underline{z}_{1r} \\ \underline{z}_{r1} & z_{rr} \end{bmatrix} \begin{bmatrix} \underline{i}_1 \\ i_r \end{bmatrix} . \qquad (8.1)$$

The subscript r denotes the port to be terminated and subscript 1 denotes all other ports of the segment. Using

$$v_r = - \frac{R}{2} i_r \qquad (8.2)$$

the impedance matrix at other ports can be obtained as

$$\underline{v}_1 = \left[\underline{z}_{11} - \frac{1}{z_{rr} + \frac{R}{2}} \underline{z}_{1r} \underline{z}_{r1} \right] \underline{i}_1 . \qquad (8.3)$$

Various segments are combined using segmentation method and optimization procedure is used to minimize $|S_{22}|$ for the odd mode. The data for the design of isolation resistance for the three types of power divider circuits studied is given in Table 8.2.

The frequency variations for the input and output VSWR's for the three circuits are shown in Fig. 8.4.

The experimental verification of the procedure is carried out by conducting measurements for a power divider with single matching section on input side. Optimization of a circuit (for stripline configuration) is carried out at $f_0 = 2 GHz$. (d = 1/4", $\varepsilon_r = 10$). The concept of scaling

Table 8.2 Design and performance with isolation resistance

Configuration	Isolation resistance	Position (distance from junction)	$\lvert S_{22}\rvert$ at 10 GHz	Minimum value of $\lvert S_{22}\rvert$ (frequency)
Single section at input	80.93Ω	0.512 cm.	0.167	0.166 (10.1 GHz)
Single section at outputs	134.97Ω	0.390 cm.	0.1923	0.1763(7.2 GHz)
Matching sections at input and outputs	131.36Ω	0.402 cm.	0.1852	0.167 (13 GHz)
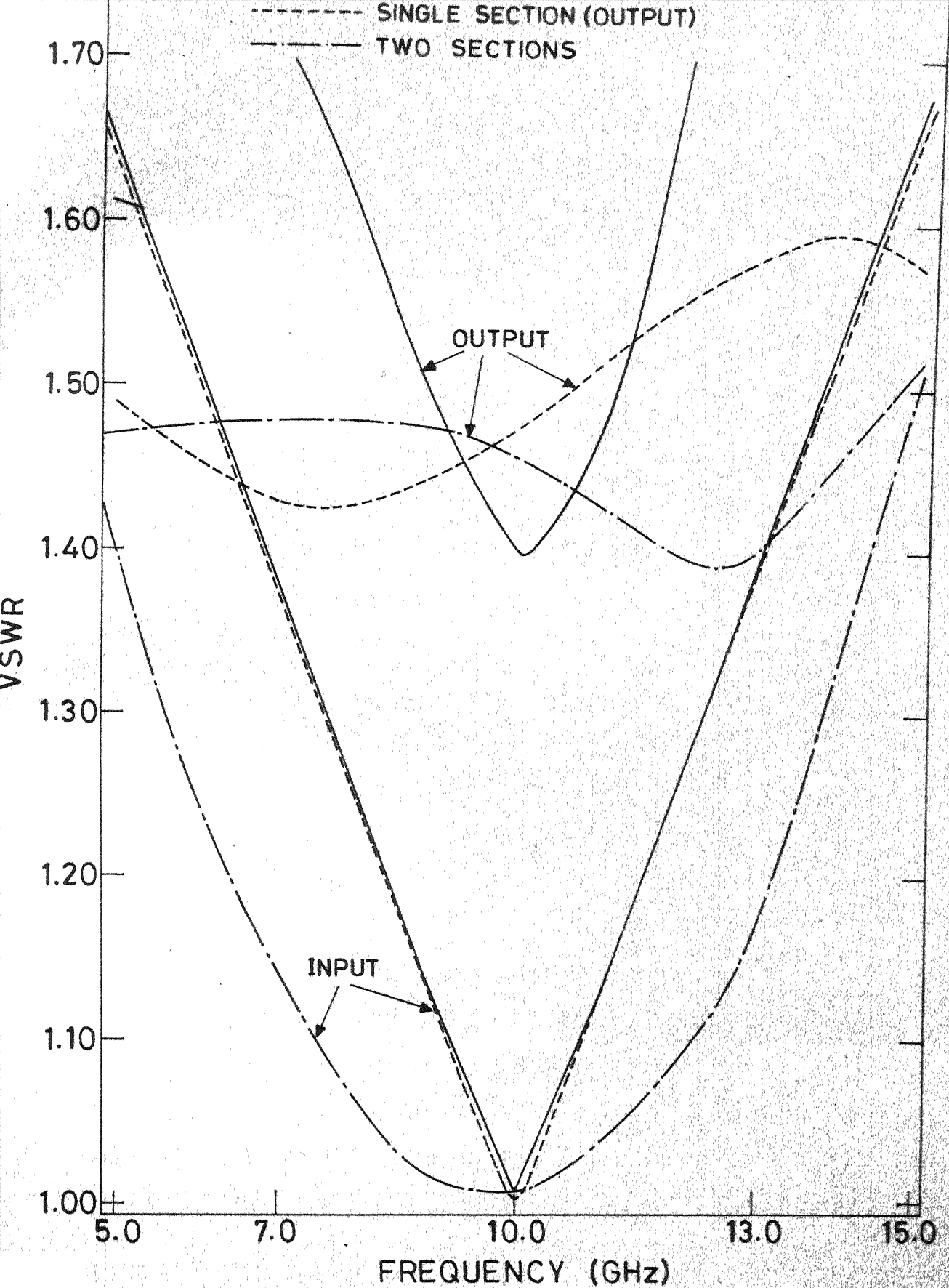
Fig. 8.4 Input and output VSWR's for the three power dividers.

described in Appendix C is used to obtain from this the
design for microstrip configuration with $f_o = 1$ GHz.
($d = 1/4$", $\varepsilon_r = 10$). This circuit design, used for fabrica-
tion, is a scaled model (Appendix C) of a circuit on
0.025" thick alumina ($\varepsilon_r = 10$) substrate with $f_o = 10$ GHz.
The dimensions obtained from scaling are for magnetic wall
model (length of $35.35\,\Omega$ segment = 2.194 cm.). The physical
dimensions of the circuit are obtained using the procedure
described in Appendix C. The dimensions of the power divider
circuit (in microstrip configuration are shown in Fig. 8.5
and an outline of the circuit layout is shown in Fig. 8.6.
The measurements have been carried out using an automatic
network analyzer*. In these measurements, no compensation
has been made for connector imperfections. The theoretical
and measured values of input VSWR are shown as a function of
frequency in Fig. 8.7. Theoretical and measured values of
coupling (i.e. $|S_{21}|$) are plotted in Fig. 8.8 as a function
of frequency. Dotted lines in these figures show maximum and
minimum values considering the uncertainity in reflection
coefficient to be 0.06 and in transmission coefficient to be
0.045. With this uncertainity taken into account, the
agreement between the theoretically predicted values and
experimental results is reasonable.

*Courtesy Mikrowellen-Laboratorium, Eidgenössische Technische
Hochschule Zürich.

Physical boundary

Magnetic wall

W = 0.607 cm

W_1 = 1.145 cm

l_1 = 1.835 cm

l_2 = 2.122 cm
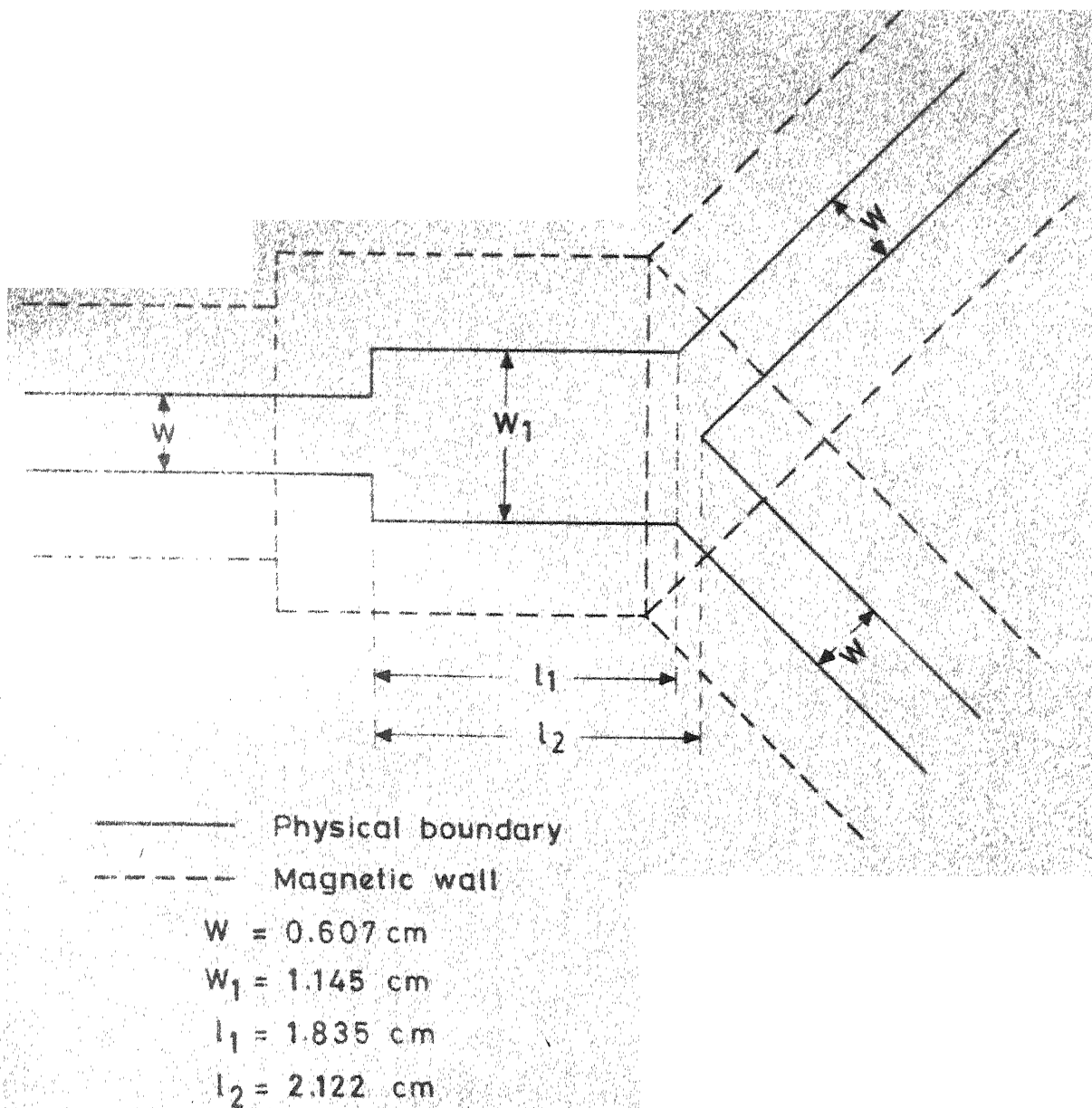
Fig 8.5 Configuration of optimized power divider
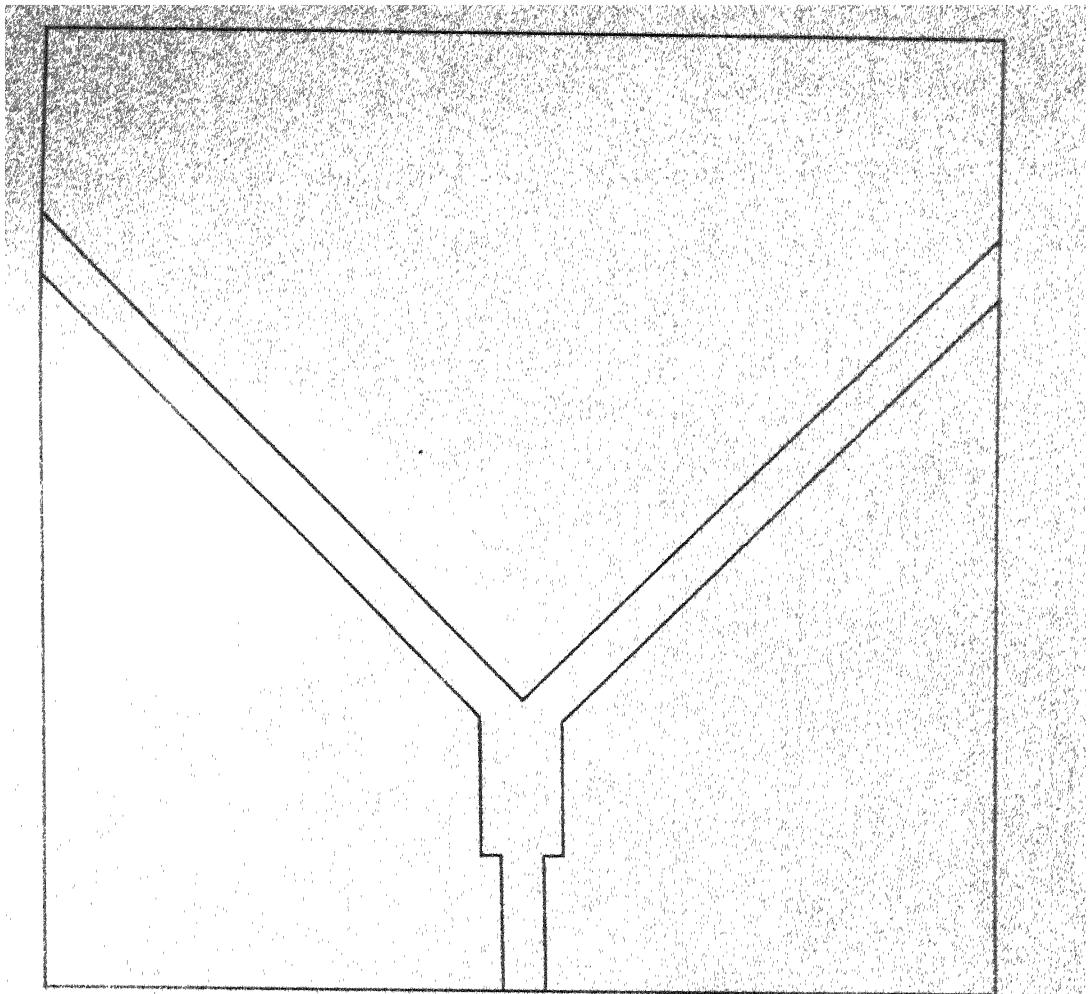
Fig.8.6   Outline of the circuit fabricated.
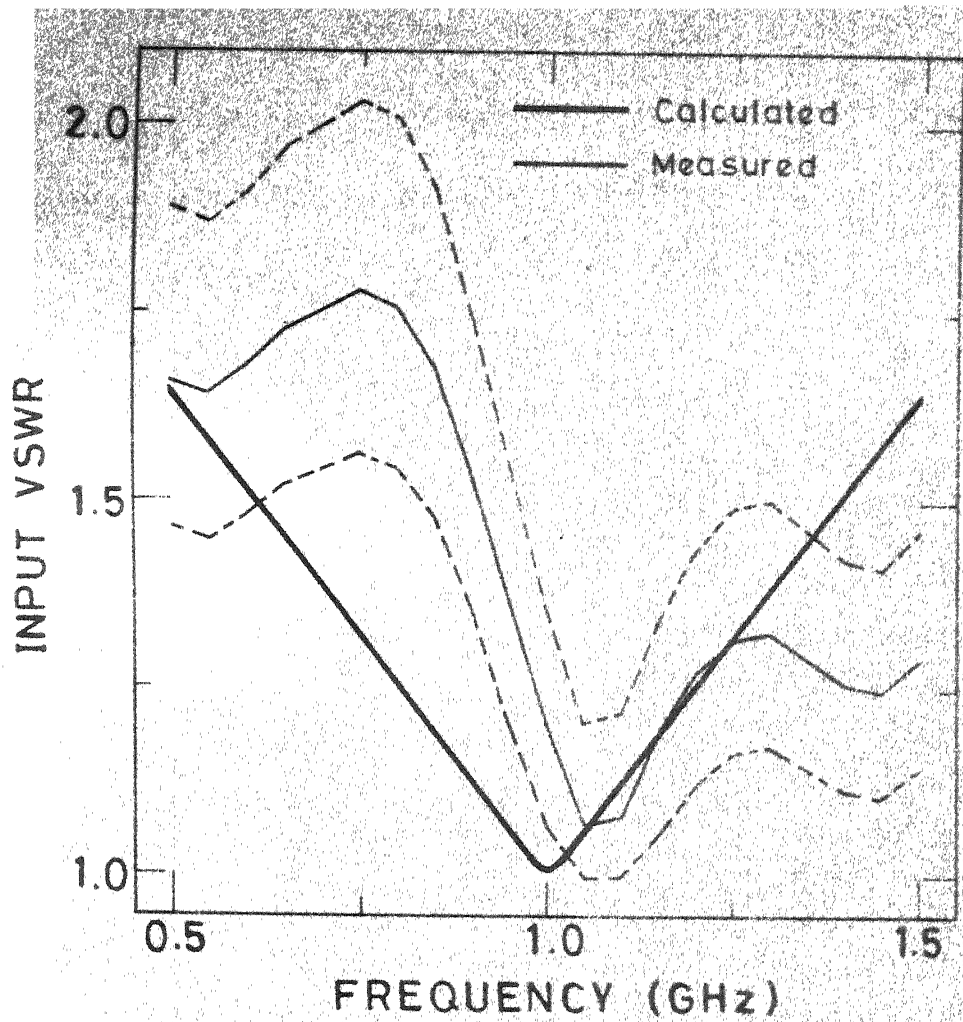
Fig . 8.7 Calculated and measured
values of VSWR
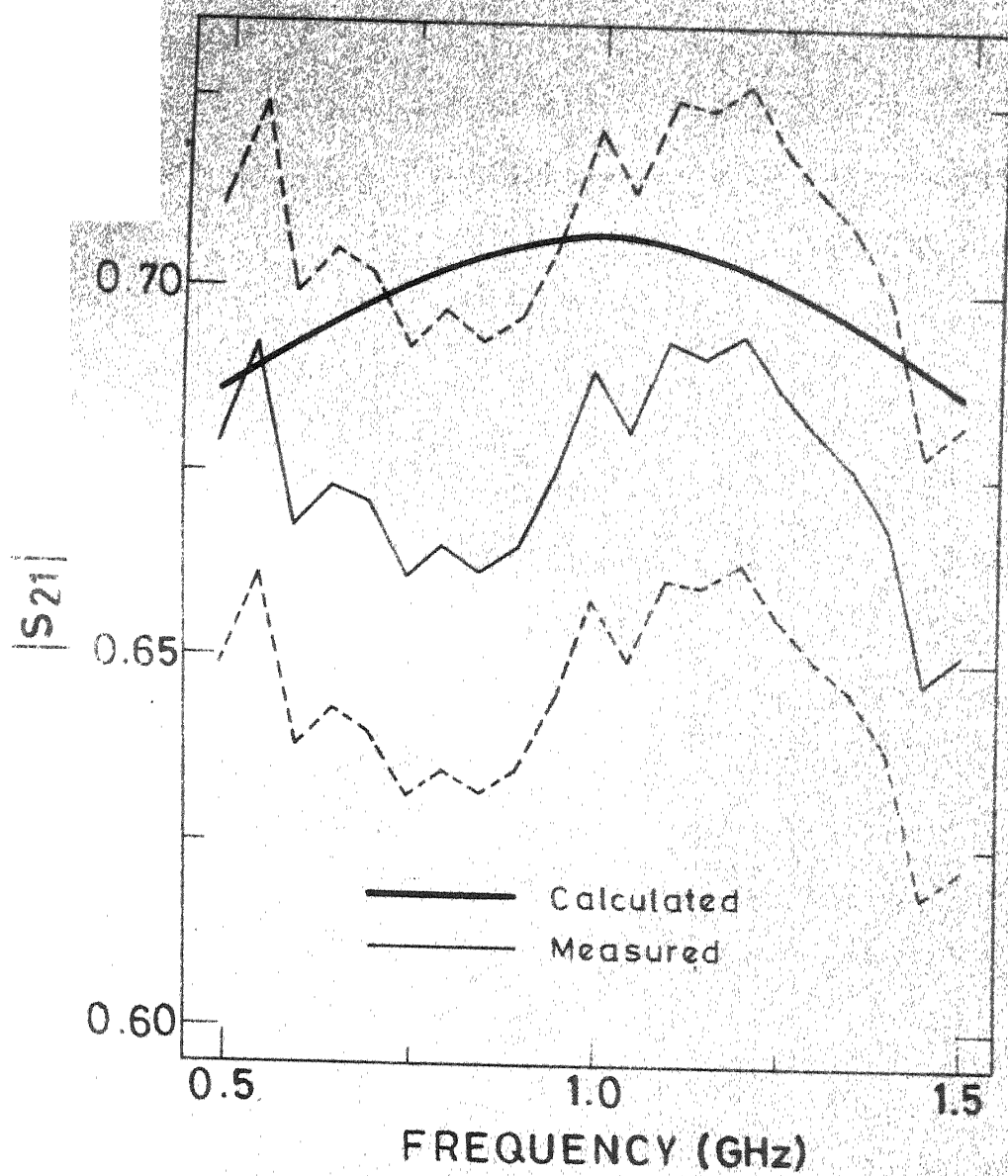
Fig. 8.8 Calculated and measured values of coupling coefficient

8.2 BRANCH-LINE HYBRID

Branch-line hybrids are commonly used in microwave circuits. At high frequencies the performance of the circuit is limited by discontinuities. This circuit uses T-junctions with impedance ratio $(1/\sqrt{2}):1:1$. As shown in the previous chapter, use of right-angled isosceles triangular geometry at these junctions reduces the parasitics. For using triangular junctions in a hybrid, two of the quarter wave sections have to be curved as shown in Fig. 7.15(b). The performance of branch-line hybrids using sections of exactly $\lambda/4$ length was evaluated in Sec. 7.3. It was observed that the center frequency is shifted and the minimum VSWR obtained is about 1.05.

The lengths of the two quarter wave sections can be modified to obtain optimum performance. All the four quarter wave sections are modelled as rectangular planar segments. Higher accuracy can be obtained by modelling the two curved segments as annular sectors with a 90° sectoral angle. The Green's function for annular sectors given in Chapter Four may be used for this purpose. However, modelling of annular segments requires equation (4.22) to be solved for each eigenvalue and thus the procedure is computationally expensive. For this reason, it has not been employed in the work reported here.

For optimizing the design of the hybrid, there are two designable parameters - i) length of the $Z_o/\sqrt{2}$ section, and

ii) length of the quarter wave section with impedance Z_0.
The objectives for optimization are to minimize VSWR and to
equalize power division at the center frequency. There are
two complex objectives S_{11} and $(S_{21} - j\, S_{41})$ whose magnitudes
are to be minimized. The least square optimization procedure
discussed in Appendix B is used. The layout for the optimum
case is shown in Fig. 8.9. Various dimensions of the opti-
mized circuit in microstrip configuration ($f_0 = 1$ GHz,
$\varepsilon_r = 10$, d = 1/4") are also indicated in the figure.
Effective lengths of 50Ω and 35.35Ω segments are 1.633 cm.
and 2.243 cm. respectively. In this design also, the micro-
strip version is obtained by using the technique of scaling
discussed in Appendix C.

The variation of input VSWR with frequency is shown in
Fig. 8.10. Figure 8.11 shows the variations of isolation
(i.e. $|S_{31}|$) and of the transfer coefficients to coupled
ports (i.e. $|S_{21}|$ and $|S_{41}|$) with frequency. The input
VSWR at the center frequency is 1.019 and the difference in
the magnitudes of coupling coefficients to the two coupled
ports at the center frequency is about 0.004.

8.3 DISCUSSION

In the optimization of input VSWR of power dividers, the
objective function contains only S_{11}. This is because the
symmetry of the circuit ensures that $S_{21} = S_{31}$ and when S_{11}
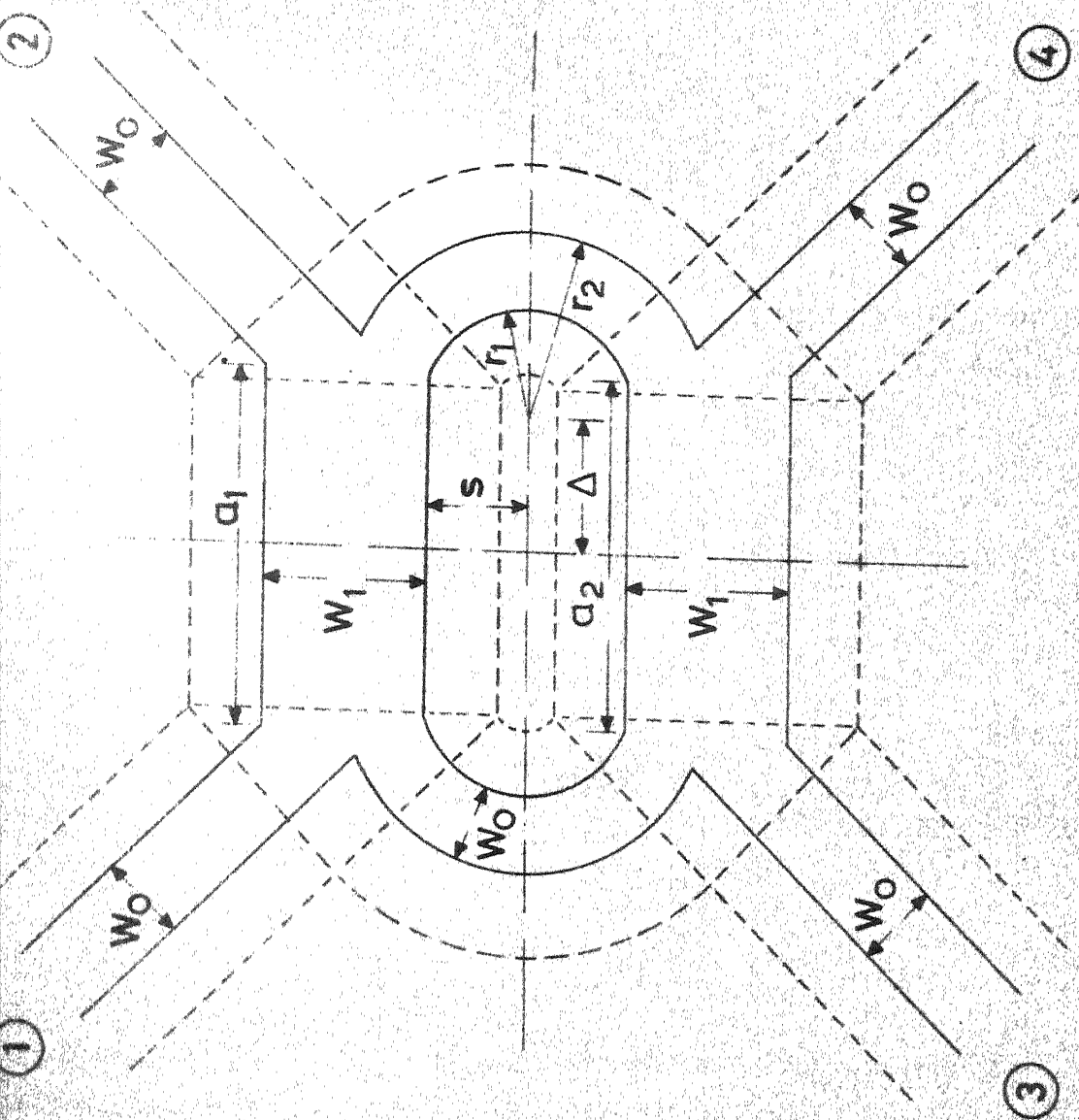
$$w_0 = 0.607\ cm$$
$$w_1 = 1.145\ cm$$
$$a_1 = 2.529\ cm$$
$$a_2 = 2.310\ cm$$
$$r_1 = 0.736\ cm$$
$$r_2 = 1.343\ cm$$
$$s = 0.698\ cm$$
$$\Delta = 0.922\ cm$$

Fig. 8.9 Configuration of optimized hybrid.
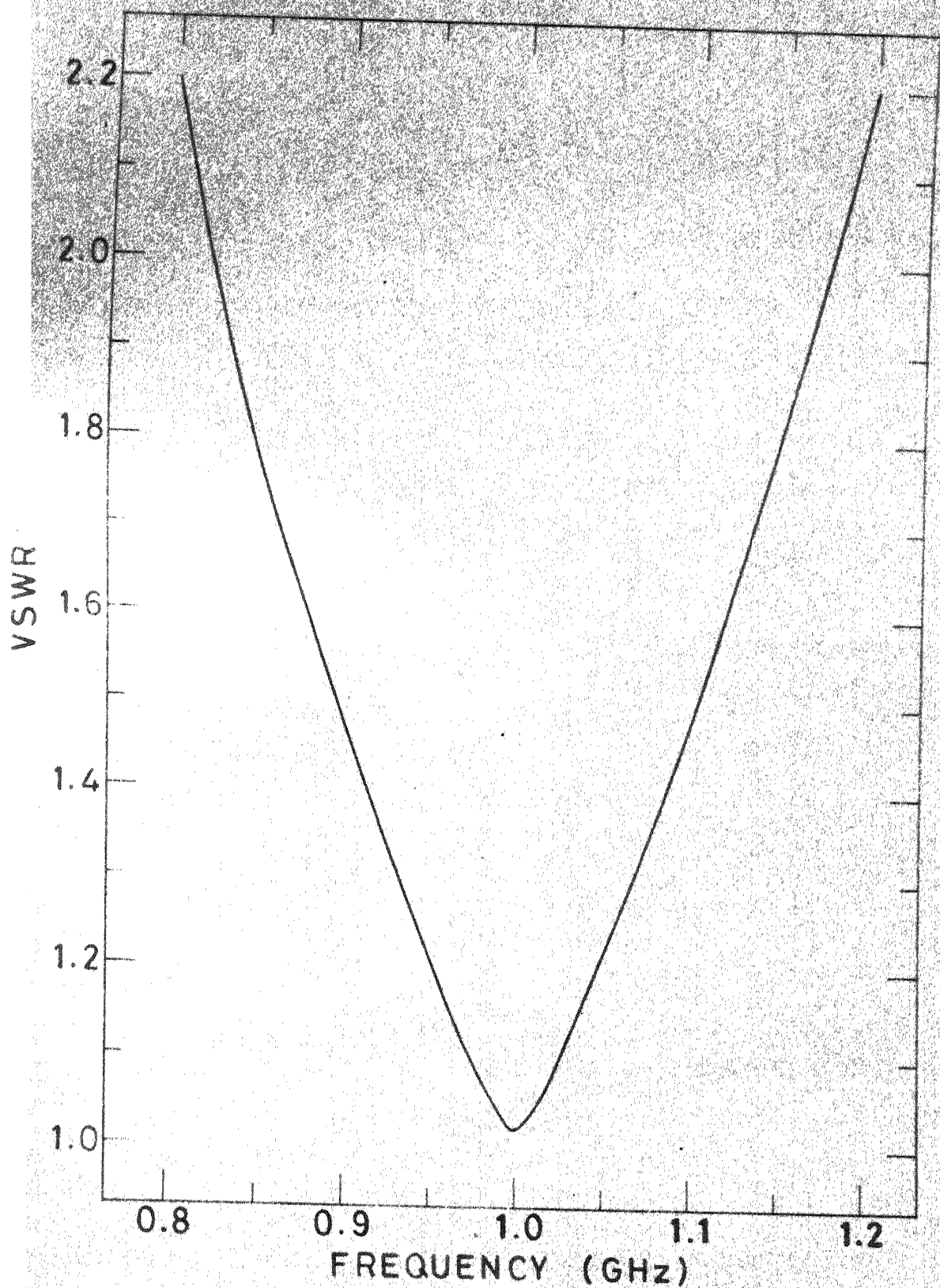
Fig. 8.10   Input VSWR of optimized hybrid.
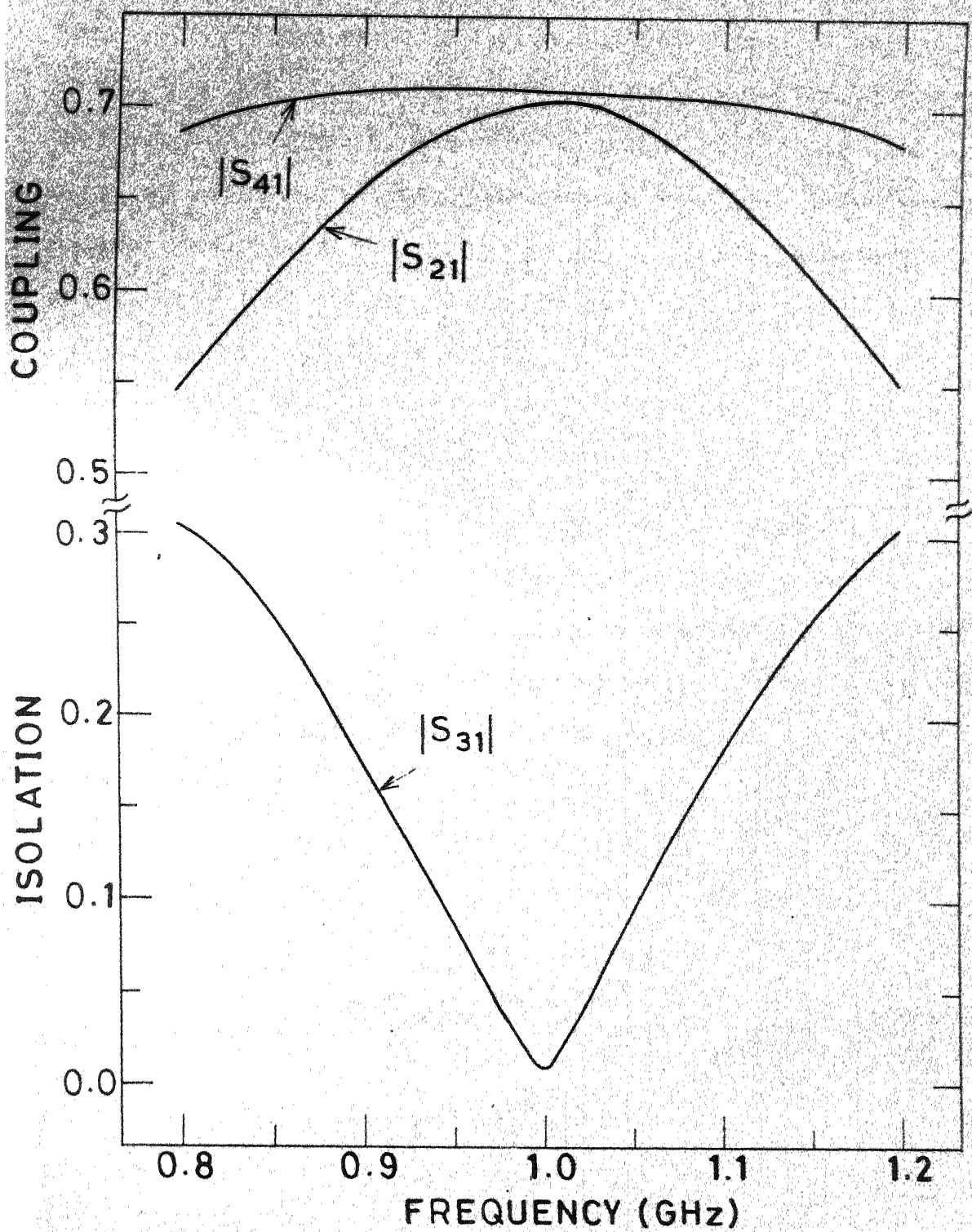
Fig. 8.11   Transfer coefficients for optimized
hybrid.

tends to zero the power division objective (i.e. equal power in the two output ports) is automatically met. In the case of branch-line hybrid, the only symmetry is that the two line sections of same impedance have equal lengths. This does not ensure equal power division when input VSWR is minimized to unity. For this reason it is necessary to have the objective as minimization of S_{11} and $(S_{21} - j\ S_{41})$. This would give the optimum which tries to minimize input VSWR as well as equalise the power division.

It has been shown in this chapter that the two-dimensional approach can be used in the optimization of strip-line and microstrip circuits. Improved designs can be obtained for circuits whose performance is limited by the presence of the discontinuity effects and the higher order modes present thereby.

Chapter Nine

CONCLUDING REMARKS

This chapter contains summary of the results reported
in this thesis and some suggestions for further investigations.

9.1 SUMMARY OF SALIENT RESULTS

The investigations reported in this thesis can be broadly
divided into two categories - i) the analytical techniques
developed for two-dimensional circuits and ii) their appli-
cations to microwave integrated circuits.

9.1.1 Analytical Techniques

Green's functions for some triangular and sectoral shapes
have been reported.

For triangular shapes, the method of images [25] has been
employed to obtain the eigenfunctions of the Helmholtz equation
which are then used to derive the Green's functions. The tri-
angular shapes considered are - i) 30° - 60° right-angled,
ii) equilateral, and iii) right-angled isosceles. Green's
functions for odd mode half-sections of some of the triangular
shapes and of a rectangle are also reported. These segments
have mixed boundary conditions and the method of images is
applied in these cases also.

The Green's functions for circular sectors, annular rings and annular sectors have been obtained by expanding these in series of eigenfunctions [25]. As mutually orthogonal eigenfunctions are obtainable for only those sectoral angles which are submultiples of π, the Green's functions are obtainable for only these sectoral shapes. For circular sectors, the eigenvalues $k^2_{n_i m}$ are given by the zeros of the first derivatives of Bessel's functions. For annular rings and annular sectors, the transcedental equation (4.22) has to be solved for evaluating various eigenvalues.

The segmentation method for the analysis of 2-d circuits has been modified so that the operations are carried out in terms of Z-matrices of individual segments. S-matrix for the overall circuit is obtained from its Z-matrix. The proposed method using Z-matrices is shown to be computationally more efficient than the earlier method.

9.1.2 Applications

Various modes of resonances for equilateral triangular, 60°-rhombic and regular hexagonal resonators have been studied. These shapes have been analyzed using Green's function for an equilateral triangle. Various modes of resonances are found for these three shapes and the voltage distributions around the periphery for these modes have been obtained. It is seen that the triangular resonators have odd modes of resonances

in addition to the even modes reported earlier. The resonance frequencies predicted have been verified experimentally for each of the three shapes.

Stripline and microstrip T-junctions have been shown to exhibit lower parasitic reactances when triangular geometries are used as compared to the junctions with rectangular geometry normally used. Two types of T-junctions with impedance ratios 1:1:1 and $(1/\sqrt{2}):1:1$ have been studied for this purpose. For T-junctions with equal impedances, an equilateral triangle and for T-junctions with impedance ratio $(1/\sqrt{2}):1:1$, a right-angled isosceles triangle is proposed for use at the junction. Improvements using triangular junctions have been verified experimentally for both the cases.

The 2-d analysis technique has been used for compensation of discontinuity reactances and optimization of power dividers and branch-line hybrids. Triangular geometries have been used at T-junctions. A least square optimization procedure is used for obtaining the designs of these circuits. Experimental results for one type of power divider circuit in microstrip configuration are also reported.

9.2 SUGGESTIONS FOR FURTHER INVESTIGATIONS

Green's functions for some other shapes can also be obtained by expansion in series of eigenfunctions. Using the eigenfunctions for elliptical shapes, Green's functions for

ellipses, elliptical sectors and elliptical rings can be derived.

Triangular, rhombic and hexagonal resonators studied can also be used as microstrip antennas by determining the radiation field around the periphery. Many other resonator shapes (like annular rings, sectors, etc.) can also be analyzed by the Green's function approach and used to design antenna configurations of similar shapes.

Triangular T-junctions considered in this thesis could also be used for improving the performance of other circuits which contain any of the two types of T-junctions discussed in Chapter Seven. Some examples of these circuits are SPDT switches, stub filters, ratrace hybrids, etc.

The technique used for minimizing the effect of parasitic reactances in T-junctions can be extended to junctions with arbitrary impedances also. In these junctions an improvement in performance is expected by using triangles with the sides equal to the effective widths of the three outgoing lines. Contour integral method [1] can be used for the analysis of these junctions. The T-junctions with arbitrary impedances are used in several microwave circuits like multi-branch directional couplers, filters, impedance matching stubs, etc. Improvements in the performance resulting from the use of triangular T-junctions in these circuits should be investigated.

Planar circuit approach has been used in discontinuity analysis [13]. With the Green's functions for triangular and sectoral shapes reported in this thesis, more generalized discontinuity configurations can now be analyzed. Some of these configurations are shown in Figures 4.1, 4.2 and 7.1. Methods for compensation of discontinuity reactances can be studied using 2-d approach.

The 2-d analysis technique can, in general, be used in optimization of the design of microstrip and stripline circuits. Considerable improvement is expected for the circuits whose performances are limited by the junction reactances and the presence of higher order modes. A general CAD program can be developed for this purpose.

Appendix A

INTEGRALS OF EIGENFUNCTIONS IN GREEN'S
FUNCTION EXPANSIONS

In this Appendix, normalized integrals of eigenfunctions (appearing in Green's function expansion) over the widths of coupling ports are given. Normalized integral is obtained by dividing the integral of eigenfunction over the width of port by the port width. These integrals have been used for the characterizations for rectangular, equilateral triangular and right-angled isosceles triangular components in Chapters Six, Seven and Eight. In the expressions which follow, function sinc (x) is given by

$$\text{sinc } (x) = \begin{cases} \dfrac{\sin x}{x} & , \quad \text{if } x \neq 0 \\[2mm] 1 & , \quad \text{if } x = 0 . \end{cases} \tag{A.1}$$

A.1 RECTANGULAR SEGMENT

Normalized integrals of the eigenfunction $\cos \dfrac{m\pi x}{a} \cos \dfrac{n\pi y}{b}$ (given in equation (2.30)) are being given for the ports along each of the four sides as shown in Fig. A.1(a). These integrals are as given in Table A.1.

Rectangular Segment with one side as Electric Wall

Green's function for odd mode half-section of a rectangle is given in Sec. 3.5. This function is used to carry out odd
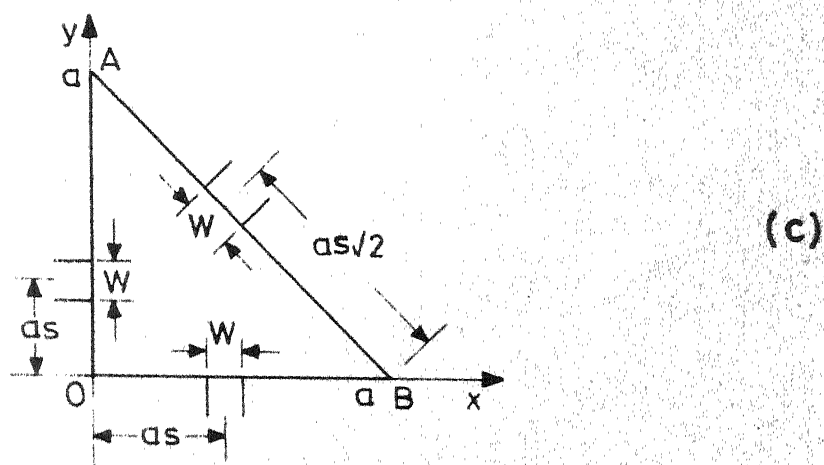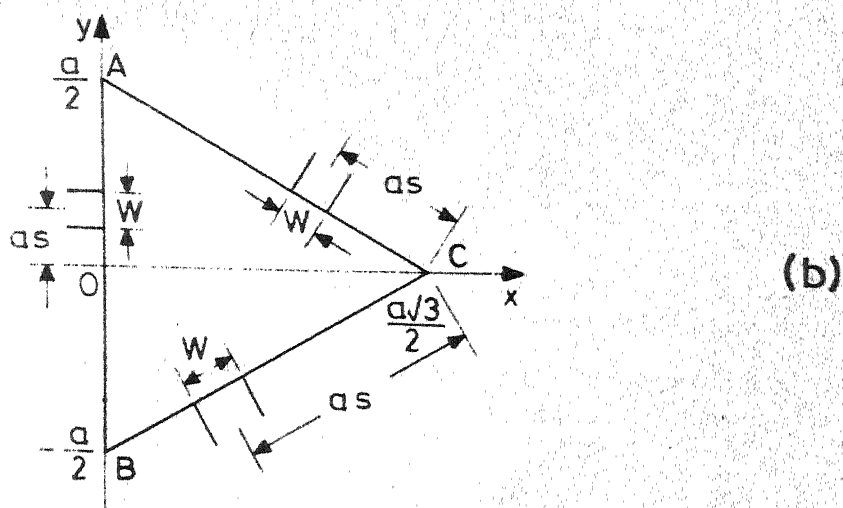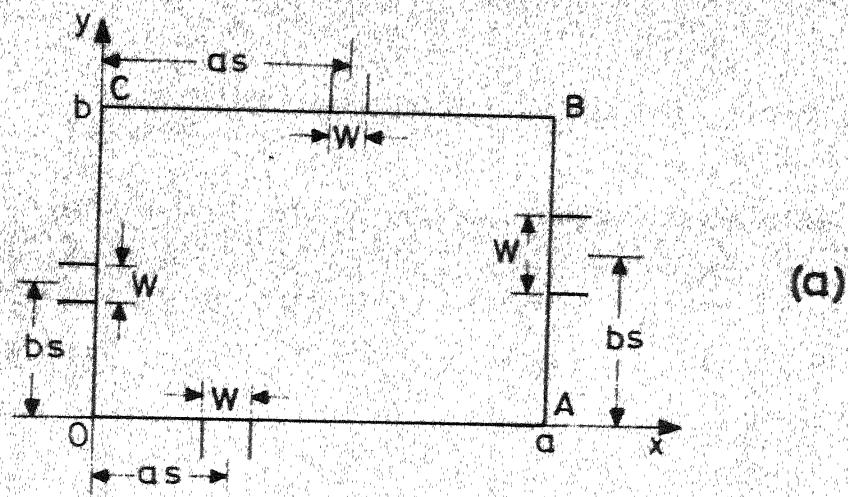
Fig. A.1   Locations of ports on various segments.

Table A.1   Normalized integrals for ports on a rectangular
segment

Locations of ports	Normalized Integrals
Along the side OC	$\cos(n\pi s)\ \mathrm{sinc}(\frac{n\pi W}{2b})$
Along the side OA	$\cos(m\pi s)\ \mathrm{sinc}(\frac{m\pi W}{2a})$
Along the side AB	$(-1)^m \cos(n\pi s)\ \mathrm{sinc}(\frac{n\pi W}{2b})$
Along the side CB	$(-1)^n \cos(m\pi s)\ \mathrm{sinc}(\frac{m\pi W}{2a})$

Table A.2   Normalized integrals for ports on a rectangular
segment with one side as an electric wall

Locations of ports	Normalized Integrals
Along the side OC	$\sin(\frac{n\pi s}{2})\ \mathrm{sinc}(\frac{n\pi W}{4b})$
Along the side AB	$(-1)^m \sin(\frac{n\pi s}{2})\ \mathrm{sinc}(\frac{n\pi W}{4b})$
Along the side CB	$(-1)^{\frac{n-1}{2}} \cos(m\pi s)\ \mathrm{sinc}(\frac{m\pi W}{2a})$

mode analysis of power dividers in Sec. 8.1. The eigen-
functions are given by $\cos \frac{m\pi x}{a} \sin \frac{n\pi y}{2b}$ where n takes only
odd values. The normalized integrals for ports along the
three sides as shown in Fig. A.1(a) are given in Table A.2.

A.2 EQUILATERAL TRIANGULAR SEGMENT

The eigenfunctions of equilateral triangular segment
(Fig. A.1(b)) are $T_1(x,y)$ and $T_2(x,y)$ given by (3.5) and
(3.15) respectively. Normalized integrals (denoted by F)
of $T_1(x,y)$ and $T_2(x,y)$ are being given for ports along each
of the three sides as shown in Fig. A.1(b). In the expres-
sions which follow, α and β are given by $\frac{\pi W}{3a}$ and $\frac{2\pi s}{3}$ res-
pectively. The normalized integrals for $T_1(x,y)$ are as given
below.

For ports along the side AB :

$$F = (-1)^{\ell} \cos[\beta(m-n)] \, \text{sinc}[\alpha(m-n)]$$
$$+(-1)^{m} \cos[\beta(n-\ell)] \, \text{sinc}[\alpha(n-\ell)]$$
$$+(-1)^{n} \cos[\beta(\ell-m)] \, \text{sinc}[\alpha(\ell-m)] \quad . \qquad (A.2)$$

For ports along the side AC :

$$F = \cos[\beta(m-n)] \, \text{sinc}[\alpha(m-n)] + \cos[\beta(n-\ell)] \, \text{sinc}[\alpha(n-\ell)]$$
$$+\cos[\beta(\ell-m)] \, \text{sinc}[\alpha(\ell-m)] \quad . \qquad (A.3)$$

For ports along the side BC, the expression for F is same as
that for ports along the side AC. The normalized integrals for

$T_2(x,y)$ are as given below.

For ports along the side AB :

$$F = (-1)^\ell \sin[\beta(m-n)] \ \text{sinc}[\alpha(m-n)]$$

$$+(-1)^m \sin[\beta(n-\ell)] \ \text{sinc}[\alpha(n-\ell)]$$

$$+(-1)^n \sin[\beta(\ell-m)] \ \text{sinc}[\alpha(\ell-m)] . \tag{A.4}$$

For ports along the side AC :

$$F = -\sin[\beta(m-n)] \ \text{sinc}[\alpha(m-n)] - \sin[\beta(n-\ell)] \ \text{sinc}[\alpha(n-\ell)]$$

$$-\sin[\beta(\ell-m)] \ \text{sinc}[\alpha(\ell-m)] . \tag{A.5}$$

For ports along the side BC, the expression for F is negative of that for the ports along AC.

A.3 RIGHT-ANGLED ISOSCELES TRIANGULAR SEGMENT

The eigenfunctions of right-angled isosceles triangle (Fig. A.1(c)) are given by $T(x,y)$ in (3.24). Normalized integrals of $T(x,y)$ are being given for ports along each of the three sides as shown in Fig. A.1(c). The normalized integrals for $T(x,y)$ are as given below.

For ports along the side OA,

$$F = \cos(n\pi s) \ \text{sinc}(\frac{n\pi W}{2a}) + (-1)^{m+n} \cos(m\pi s) \ \text{sinc}(\frac{m\pi W}{2a}). \tag{A.6}$$

For ports along the side OB,

$$F = \cos(m\pi s) \ \text{sinc}(\frac{m\pi W}{2a}) + (-1)^{m+n} \cos(n\pi s) \ \text{sinc}(\frac{n\pi W}{2a}). \tag{A.7}$$

For ports along the side AB,

$$F = (-1)^m \{ \cos[(m+n)\pi s] \, \text{sinc}[(m+n)\alpha] +$$

$$\cos[(m-n)\pi s] \, \text{sinc}[(m-n)\alpha] \} \qquad (A.8)$$

where

$$\alpha = \frac{\pi W}{2\sqrt{2}a} \quad .$$

Odd mode half-section

Green's function when side OB in Fig. A.1(c) is an electric wall is given by (3.29). This function is used to carry out odd mode analysis of power dividers in Sec. 8.1. The eigenfunction U(x,y) is given by (3.30). Normalized integrals, F, of U(x,y) for ports along two sides of the triangle are given below.

For ports along the side OA,

$$F = \sin(\frac{n\pi s}{2}) \, \text{sinc}(\frac{n\pi W}{4a}) - (-1)^{\frac{m+n}{2}} \sin(\frac{m\pi s}{2}) \, \sin(\frac{m\pi W}{4a}) \quad . \quad (A.9)$$

For ports along side AB,

$$F = (-1)^{\frac{m+1}{2}} \{ \cos[(m+n)\beta] \, \text{sinc}[(m+n)\alpha] -$$

$$\cos[(m-n)\beta] \, \text{sinc}[(m-n)\alpha] \} \qquad (A.10)$$

where

$$\alpha = \frac{\pi W}{4\sqrt{2}a} \qquad \text{and} \quad \beta = \pi s/2 \quad .$$

Appendix B

OPTIMIZATION PROCEDURE USED

This appendix describes the procedure used for optimization of circuits in Chapter Eight. The method uses the gradient of the performance objectives which are expressed in terms of S-parameters. Differential Z-matrices of components with respect to the designable parameters are obtained by series summation in the same manner as used for Z-matrices of components. For segmentation, these differential Z-matrices are put together in the same form as in equation (5.11). The differential Z-matrix of the overall network is obtained using (5.14) as

$$Z'_p = Z'_{pp} + (Z'_{pq} - Z'_{pr})(Z_{qq} - Z_{qr} - Z_{rq} + Z_{rr})^{-1} (Z_{qp} - Z_{qp})$$

$$- (Z_{pq} - Z_{pr})(Z_{qq} - Z_{qr} - Z_{rq} + Z_{rr})^{-1} [(Z'_{qq} - Z'_{qr} - Z'_{rq} + Z'_{rr})$$

$$\cdot (Z_{qq} - Z_{qr} - Z_{rq} + Z_{rr})^{-1} (Z'_{qp} - Z_{rp}) + (Z'_{qp} - Z'_{rp})]. \quad (B.1)$$

The differential Y-matrix is obtained using

$$Y'_p = -Z_p^{-1} Z'_p Z_p^{-1} \qquad (B.2)$$

and the external subports are combined in the same manner as in (5.23). The differential S-matrix of the overall network is obtained using (5.24) as

$$S' = -[\sqrt{Z_0}][I + (Y_0 - Y)(Y_0 + Y)^{-1}] Y'(Y_0 + Y)^{-1} [\sqrt{Y_0}]. \quad (B.3)$$

Having obtained the differential S-matrices, the gradient of performance can be determined and any of the gradient optimization methods can be used. A least square optimization procedure is utilized in Chapters Seven and Eight.

Optimization of Least Square Objective Functions

The procedure described here minimizes the sum of squares of deviations. It is based on Gaussian least square solution. The method uses the gradients of each of the terms and avoids one-dimensional search in the design space.

Let the objective function U to be minimized be written as

$$U = f_1^2 + f_2^2 + \ldots + f_m^2 \qquad (B.4)$$

where f_1, f_2, ..., f_m are the functions of the designable parameters $\underline{x}$ given by

$$\underline{x} = \{x_1, x_2, \ldots, x_n\}^t \qquad (B.5)$$

with $m \geq n$. The minimization of U in (B.4) is equivalent to minimizing the norm of an m-dimensional objective function vector

$$\underline{f}(\underline{x}) = \{f_1(\underline{x}), f_2(\underline{x}), \ldots, f_m(\underline{x})\}^t \qquad (B.6)$$

with $f_1(\underline{x})$, $f_2(\underline{x})$, ..., $f_m(\underline{x})$ being its components. The norm of $\underline{f}(\underline{x})$ is taken to be $[\underline{f}(\underline{x})]^t [\underline{f}(\underline{x})]$ and is equal to U given by (B.4). The Jacobian, formed using derivatives of the

components of the vector objective function, is given as

$$
\underline{J}(\underline{x}) = \begin{bmatrix}
\dfrac{\partial f_1}{\partial x_1} & \dfrac{\partial f_1}{\partial x_2} & \cdots & \dfrac{\partial f_1}{\partial x_n} \\[2ex]
\dfrac{\partial f_2}{\partial x_1} & \dfrac{\partial f_2}{\partial x_2} & \cdots & \dfrac{\partial f_2}{\partial x_n} \\[2ex]
\vdots & \vdots & & \vdots \\[2ex]
\dfrac{\partial f_m}{\partial x_1} & \dfrac{\partial f_m}{\partial x_2} & \cdots & \dfrac{\partial f_m}{\partial x_n}
\end{bmatrix} . \tag{B.7}
$$

The value of the vector objective function $\underline{f}$ can be estimated at $\underline{x} + \Delta\underline{x}$ using the Taylor series expansion as

$$
\underline{f}(\underline{x} + \Delta\underline{x}) = \underline{f}(\underline{x}) + \underline{J}(\underline{x}) \, \Delta\underline{x} \tag{B.8}
$$

where the increment $\Delta\underline{x}$ is assumed to be small so that the higher order terms can be neglected.

In this method, $\Delta\underline{x}$ is chosen such that the norm of $\underline{f}(\underline{x} + \Delta\underline{x})$, given by the right-hand side of (B.8), is minimum. The value of $\Delta\underline{x}$ giving minimum norm of $\underline{f}(\underline{x}) + \underline{J}(\underline{x}) \, \Delta\underline{x}$ is given by [34]

$$
\Delta\underline{x} = -\,\{[\underline{J}(\underline{x})]^{t}\,[\underline{J}(\underline{x})]\}^{-1}\,[\underline{J}(\underline{x})]^{t}\,\underline{f}(\underline{x}) . \tag{B.9}
$$

The process converges in a single iteration if U given by (B.4) is quadratic. For higher order objective functions, this process has to be repeated i.e. $\underline{f}(\underline{x})$ and $\underline{J}(\underline{x})$ are computed at $\underline{x} + \Delta\underline{x}$ and a new $\Delta\underline{x}$ is obtained. This process is repeated till convergence.

A common drawback using this method is that $\Delta \underline{x}$, as computed from (B.9) may become too large. In such cases it is desirable to restrict each component of $\Delta \underline{x}$ to a pre-specified value.

This technique has been used for optimization in this thesis. The scattering parameters, being complex, are treated as two components of the vector objective function. For example, in the case of minimizing input reflection coefficient, $\underline{f}$ is expressed as

$$\underline{f} = \{\mathrm{Re}(S_{11}), \quad \mathrm{Im}(S_{11})\}^{t}. \tag{B.10}$$

In the design of branch-line hybrid the objectives for optimization are to minimize the input VSWR and to equalize power division. Objective function vector $\underline{f}$ is expressed as

$$\underline{f} = \{\mathrm{Re}(S_{11}), \ \mathrm{Im}(S_{11}), \quad \mathrm{Re}(S_{21} - j\, S_{41}), \ \mathrm{Im}(S_{21} - j\, S_{41})\}^{t}. \tag{B.11}$$

The results reported in Chapters Seven and Eight are based on the optimization procedure described above.

Appendix C

SCALING FOR PLANAR CIRCUITS

Once a 2-d circuit has been designed for a given set of specifications, the principle of scaling may be used to design a circuit with similar specifications at a different frequency or with different (scaled) impedances at all the ports. Design of a stripline type circuit from a microstrip type circuit (and vice versa) is also possible through scaling.

C.1 EFFECTIVE DIMENSIONS

For the purpose of scaling, the dimensions considered include the extension of periphery for taking into account the fringing field in open boundary planar circuits. In stripline type 2-d circuits, the effective width of a transmission line of impedance Z_o is given by

$$W_{eff} = \frac{\eta\, d}{2 Z_o} \tag{C.1}$$

and equals $(W + 2\delta)$ with

$$\delta = \frac{2d\, \ln 2}{\pi} . \tag{C.2}$$

In microstrip type 2-d circuits, the effective width of transmission line of impedance Z_o is

$$W_{eff} = \frac{\eta\, d}{Z_o} . \tag{C.3}$$

The width W is related to the impedance Z_o by [35]

$$W = 8d \frac{\left\{[\exp(Z_o\sqrt{\varepsilon_r+1}/42.4)-1](7+4/\varepsilon_r)/11 + (1+1/\varepsilon_r)/0.81\right\}^{\frac{1}{2}}}{\exp(Z_o\sqrt{\varepsilon_r+1}/42.4) - 1}$$

$$(C.4)$$

and δ is computed as

$$\delta = (W_{eff} - W)/2 .$$ (C.5)

Consider a rectangular segment with effective length and width ℓ_e and W_e respectively. In stripline configuration δ is almost independent of width and the extensions along the length and width are same. For microstrip configuration, first Z_ℓ is computed as $\eta d/\ell_e$. The actual length ℓ is computed from Z_ℓ using (C.4). The extension along the length is obtained as $(\ell_e - \ell)/2$. The extension along the width is computed as described above using (C.3) to (C.5).

C.2 FREQUENCY SCALING

The concept of frequency scaling applicable to stripline, microstrip and waveguide circuits [36], [37] can be applied to general 2-d planar circuits also. If all the linear dimensions in the planar patch are reduced by a scaling factor K and it is deposited on a substrate of height d/K, the response of the modified circuit at frequency f will be same as that of the original circuit on a substrate of height d at frequency f/K. For example, if a circuit has been designed at 1 GHz on a 5 mm thick substrate, by scaling down all the linear dimensions of the patch by a factor of 10 and fabricating it on a 0.5 mm thick substrate the design can be used at 10 GHz.

It may be noted that for stripline type circuits, extension of boundary because of the fringing field is proportional to the height of the substrate. Thus, actual physical dimensions may be used for the purposes of frequency. scaling.

C.3 IMPEDANCE SCALING

The concept of impedance scaling gives another planar circuit which has impedance values at all the coupling ports scaled by some factor and has the same frequency response for the scattering parameters. The new circuit has to be deposited on a substrate of different height and all dimensions of the 2-d patch remain the same. If the planar patch is deposited on a substrate of height Kd, the S-matrix of the new circuit would be the same as that of the original circuit on substrate height d. For the new circuit, the impedances at all the coupling ports are scaled up by the factor K.

The two types of scaling concepts discussed above may be combined together. For example, if the height of the substrate is kept unchanged and linear dimensions scaled up by a factor K, the S-matrix of the modified circuit at the frequency f/K is the same as that of the original circuit at frequency f but all impedances levels (in the modified circuit) are scaled down by the factor K.

C.4 DESIGN OF A STRIPLINE TYPE CIRCUIT FROM A MICROSTRIP TYPE PLANAR CIRCUIT (AND VICE VERSA)

The concept of scaling can also be applied to obtain an

equivalent design in the microstrip type configuration from the design in the stripline type configuration and vice versa. The scattering matrix response of a stripline type planar circuit with spacing 2d between the ground planes will be the same as that of a microstrip type planar circuit with substrate height d, provided the linear dimensions (between the magnetic walls) in the 2-d patches are the same in both the cases. It may be be noted that the characteristic impedance values at the coupling ports for the microstrip type circuit will be twice the corresponding values for the stripline type circuit. Impedance scaling technique can be used in conjunction with the above conversion to get the desired impedance values at the coupling ports.

These scaling techniques provide an additional flexibility in design and are used to obtain the designs of circuits in microstrip configuration in Chapter Eight.

REFERENCES

[1]   T. Okoshi and T. Miyoshi, "The planar circuit – An approach to microwave integrated circuitry," IEEE Trans. Microwave Theory Tech., vol. MTT-20, pp.245-252, Apr. 1972.

[2]   P. Silvester, "Finite element analysis of planar microwave networks," IEEE Trans. Microwave Theory Tech., vol. MTT-21, pp. 104-108, Feb. 1973.

[3]   T. Okoshi and T. Takeuchi, "Analysis of planar circuits by segmentation method," Electron. Commun. Japan, vol. 58-B, no.8, pp. 71-79, Aug. 1975.

[4]   T. Okoshi, Y. Uehara, and T. Takeuchi, "The segmentation method – An approach to the analysis of microwave planar circuits," IEEE Trans. Microwave Theory Tech., vol.MTT-24, pp. 662-668, Oct. 1976.

[5]   T. Okoshi, T. Takeuchi, and J.P. Hsu, "Planar 3-db hybrid circuit," Electron. Commun. Japan, vol. 58-B, no. 8, pp. 80-90, Aug. 1975.

[6]   O.C. Zienkiewicz, The Finite Elements Method. London : McGraw-Hill, 1977.

[7]   Y. Rahmat-Samii, T. Itoh, and R. Mittra, "A spectral domain analysis for solving microstrip discontinuity problems," IEEE Trans. Microwave Theory Tech., vol. MTT-22, pp. 372-378, Apr. 1974.

[8]   A.K. Sharma, "Spectral domain analysis of microstrip resonant structures," Ph.D. dissertation, Department of Electrical Engineering, Indian Institute of Technology, New Delhi, India, 1979.

[9]   J. Helszajn and D.S. James, "Planar triangular resonators with magnetic walls," IEEE Trans. Microwave Theory Tech., vol. MTT-26, pp. 95-100, Feb. 1978.

[10]   J. Helszajn, D.S. James, and W.T. Nisbet, "Circulators using planar triangular resonators," IEEE Trans. Microwave Theory Tech., vol. MTT-27, pp. 188-193, Feb. 1979.

[11]   H.M. Altschuler and A.A. Oliner, "Discontinuities in
        the center conductor of symmetric strip transmission
        line," IRE Trans. Microwave Theory Tech., vol.MTT-8,
        pp. 328-339, May 1960.

[12]   K.C. Gupta, R. Garg, and I.J. Bahl, Microstrip Lines
        and Slotlines. Dedham, MA : Artech House, 1979.

[13]   T. Miyoshi, "Expansion of electromagnetic field in
        planar circuits," Electron. Commun. Japan, vol. 58-B,
        no.2, pp. 100-108, Feb. 1975.

[14]   T. Miyoshi and T. Okoshi, "Analysis of microwave
        planar circuits," Electron. Commun. Japan, vol. 55-B,
        no.8, pp. 24-31, Aug. 1972.

[15]   T. Miyoshi, S. Yamaguchi, and S. Goto, "Ferrite planar
        circuits in microwave integrated circuits," IEEE Trans.
        Microwave Theory Tech., vol. MTT-25, pp. 593-600,
        July 1977.

[16]   T. Miyoshi and S. Miyauchi, "The design of planar
        circulators for wide-band operation," IEEE Trans.
        Microwave Theory Tech., vol. MTT-28, pp. 210-214,
        Mar. 1980.

[17]   Y.T. Lo, D. Solomon, and W.F. Richards, "Theory and
        experiment on microstrip antennas," IEEE Trans.
        Antennas Propagat., vol. AP-27, pp. 137-145, Mar.1979.

[18]   K.C. Gupta and P.C. Sharma, "Segmentation and desegmen-
        tation techniques for analysis of planar microstrip
        antennas," accepted for presentation at 1981 Int.
        IEEE/AP-S Symposium, Los Angeles, CA, USA, June 16-19,
        1981.

[19]   J. Watkins, "Circular resonant structures in microstrip,"
        Electron. Lett., vol. 5, pp. 524-525, 1969.

[20]   I. Wolff, "Microstrip bandpass filter using degenerate
        modes of a microstrip ring resonator," Electron. Lett.
        vol. 8, pp. 302-303, 1972.

[21]   G.D'Inzeo, F. Giannini, C.M. Sodi, and R. Sorrentino,
        "Method of analysis and filtering properties of
        microwave planar networks," IEEE Trans. Microwave
        Theory Tech., vol.MTT-26, pp.462-471, July 1978.

[22]   A.K. Sharma and W.J.R. Hoefer, "Spectral domain
        analysis of an hexagonal microstrip resonator," to be
        published.

[23] E.S. Kuh and R.A. Rohrer, Theory of Linear Active Networks. San Francisco, CA: Holdern-Day, 1967, p. 271.

[24] V.A. Monaco and P. Tiberio, "Computer-aided analysis of microwave circuits," IEEE Trans. Microwave Theory Tech., vol. MTT-22, pp. 249-263, Mar. 1974.

[25] P.M. Morse and H. Feshbach, Methods of Theoretical Physics. New York : McGraw-Hill, 1953, ch. 7.

[26] S.A. Schelkunoff, Electromagnetic Waves. New York : Van Nostrand, 1943, p. 393.

[27] T. Okoshi and S. Kitazawa, "Computer analysis of short-boundary planar circuits," IEEE Trans. Microwave Theory Tech., vol. MTT-23, pp. 299-306, Mar. 1975.

[28] H. Howe, Jr., Stripline Circuit Design. Dedham, MA: Artech House, 1974, ch. 3.

[29] V.A. Monaco and P. Tiberio, "Automatic scattering matrix computation of microwave circuits," Alta Freq., vol. 39, pp. 59-64, Feb. 1970.

[30] R.T. Irish, "Elliptic resonator and its use in micro-circuit systems," Electron. Lett., vol. 7, pp. 149-150, Apr. 1971.

[31] W.T. Nisbet and J. Helszajn, "Mode chart for microstrip resonators on dielectric and magnetic substrates using a transverse resonance method," Microwaves Opt. Acous., vol. 3, pp. 69-77, Mar. 1979.

[32] J.P. Hsu, O. Kondo, T. Anada, and H. Makino, "Measurement and calculation of eigenvalues of various triplate type microwave planar circuits," Rec. of Professional Groups, IECEJ, Paper MW 73-117, Feb. 1974.

[33] R.V. Garver, Microwave Diode Control Devices. Dedham, MA: Artech House, 1975, ch. 7, p. 193.

[34] S. Barnett, Matrices in Control Theory with Applications to Linear Programming. New York: Van Nostrand, 1971, ch. 6, p. 130.

[35] H.A. Wheeler, "Transmission-line properties of a strip on a dielectric sheet on a plane," IEEE Trans. Microwave Theory Tech., vol. MTT-25, pp. 631-647, Aug. 1977.

[36]   M.V. Schneider, "Millimeter-wave integrated circuits,"
         in IEEE, G-MTT Int. Microwave Symp. Digest, 1973,
         pp. 16-18.

[37]   M.V. Schneider and W.W. Snell, Jr., "A scaled hybrid
         multiplier from 10 to 30 GHz.," B.S.T.J., vol. 50,
         pp. 1933-1942, July/Aug. 1971.